SPECTROSCOPY OF NEUTRON UNBOUND STATES IN NEUTRON RICH CARBON

By

Shea Mosby

A DISSERTATION

Submitted to
Michigan State University
in partial fulfillment of the requirements
for the degree of

DOCTOR OF PHILOSOPHY

Physics

2011

ProQuest LLC.
789 East Eisenhower Parkway
P.O. Box 1346
Ann Arbor, MI 48106 - 1346

ABSTRACT

SPECTROSCOPY OF NEUTRON UNBOUND STATES IN NEUTRON RICH CARBON

By

Shea Mosby

Neutron unbound states in ^{19,21}C have been populated by nucleon removal from a beam of ^{22}N at 68 MeV/u, and the invariant mass method was used to reconstruct decay energies of the reaction products. Charged fragments were bent from the beam axis by a dipole magnet and their properties measured by a suite of charged particle detectors sufficient to identify individual reaction products and reconstruct momentum vectors at the reaction target. Neutrons were detected at forward angles by the Modular Neutron Array (MoNA), which measured their trajectory and time of flight.

A resonance at 76 ± 14 keV was observed in the decay spectrum of ^{19}C, corresponding to an excited state at 383 ± 15 keV. Comparison to shell model calculations results in the assignment of this state to the $5/2^+_1$ state in ^{19}C, and the resulting level scheme indicates a breakdown in existing shell model descriptions of this nucleus. In the case of ^{21}C, an s-wave line shape was used to describe the experimental decay energy spectrum, resulting in a scattering length limit of $|a_s| < 1.5$ fm. This result suggests that ^{22}C is bound by less than 100 keV.

DEDICATION

To Michelle

ACKNOWLEDGMENT

I would like to thank Michael Thoennessen for serving as my advisor during my time as a graduate student. Thank you for making the effort to direct my work while allowing me the freedom to follow my own trains of thought and make many of my own mistakes. I would also like to thank my committee members (Artemis Spyrou, Hironori Iwasaki, Scott Bogner, James Linnemann, and Phillip Duxbury) for their time spent reviewing my work. In particular, Artemis was a valuable source of advice and motivation during my time at the NSCL.

The NSCL operations staff was invaluable during the execution of my experiment, providing a high quality beam well above the predicted rates which ultimately made my results tractable. I am indebted to the MoNA Collaboration for the construction and maintenance of MoNA, without which my thesis work would never have existed. My fellow MoNA graduate students (Greg Christian, Jenna Smith, Jesse Snyder, and Michael Strongman) provided invaluable support during the execution of my experiment, as well as uncounted hours of input and discussions. Thanks is also due to the other members of the NSCL graduate student body - too many students to mention by name - who assisted in the work presented here, whether it be a clever programming trick or an encouraging word on an otherwise discouraging day.

Warren Rogers deserves particular thanks for his role in starting me on the path that led to this point. As an academic advisor, role model, and friend he awoke my interest in Physics as more than a hobby and has served as an immense source of information, advice, and inspiration.

Words fail to express the debt I owe my wife, Michelle, for her contributions to this work. Thank you for the countless hours you've spent supporting me on this endeavor while working toward your own doctorate - I never could have done this without you. Your influence permeates all aspects of this work, whether it was logic checking a thought I had, encouraging me to try "just one more" idea out on a

particularly difficult analysis challenge, or suffering through and providing emotional support during the difficult times. Finally, I'd like to acknowledge the rest of my family for their support during this whole process. Without you all I wouldn't be the person I am today.

TABLE OF CONTENTS

LIST OF FIGURES

Chapter 1

Introduction

The study of nuclear structure asks a simple question with a complex answer: how do combinations of protons and neutrons behave when they are assembled into an atomic nucleus? The nature of this problem precludes a simple answer - a full description of the atomic nucleus requires solving an n-body problem (where n is an arbitrary number of nucleons), which alone is a significant computational challenge. Furthermore, the binding of protons and neutrons together is largely mediated by the strong force, a force which is not well-understood at present and therefore a complete and robust form is not available for such calculations. Work on both of these challenges is ongoing, and progress is being made for the lightest nuclei where the calculation space is still tractable given current computational constraints [1]. Moving beyond the lightest of systems requires appealing to some other, more approximate model. One very well tested model is the nuclear shell model, which treats nuclei as collections of protons and neutrons filling discretized energy levels within some sort of mean field in a description which is qualitatively similar to the description of electrons orbiting the nucleus in atomic physics.

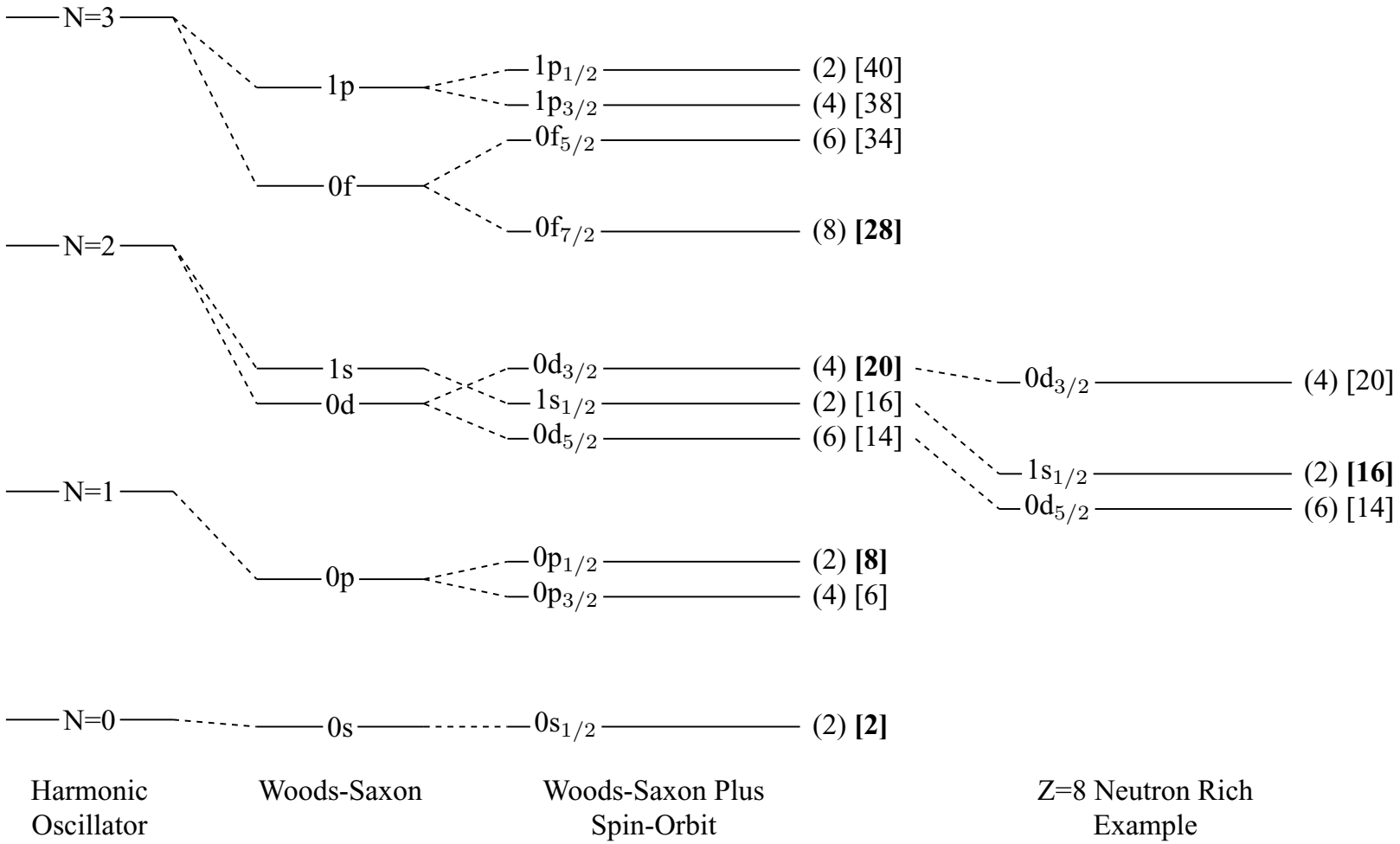

Figure 1.1: Schematic rendering of the development of a shell model, with example energy level shifts for ^{24}O.

This model is shown schematically in Figure 1.1. The motivation to construct such a model began in the 1930's, when measurements began demonstrating that certain "magic" numbers of protons and neutrons resulted in increased stability. Initial skepticism that the nucleus could be described with a mean-field approach fell away under the weight of experimental evidence over the next decade, with M. Goeppert-Mayer noting the existence of increased stability at nucleon numbers 8, 20, 50, 82 and 126 in 1948 [2]. Simple potentials only reproduced the lightest magic numbers of 8 and 20, but in 1949 two different groups independently demonstrated that adding a spin-orbit term to a harmonic oscillator potential could reproduce all of the magic numbers [3, 4]. The swapping of a harmonic oscillator for a Woods-Saxon potential first developed 5 years later [5] further improved the model, which is capable of describing nuclei near stability very well across the entire nuclear chart. Figure 1.1 demonstrates that the shell model describes these magic numbers (indicated by bold face lettering) as corresponding to shell closures, followed by a large energy gap to the next level.

Near the limits of existence, this theoretical description begins to break down. In particular, the level structure changes as one moves to more asymmetric nuclear matter (extreme A/Z ratios). One such example is neutron-rich oxygen, as demonstrated in Figure 1.1. In particular, the neutron *sd* shell splits apart, resulting in a new large shell gap at N=16 for ^{24}O. In recent years, significant effort has been put forth from both theoretical and experimental camps to understand and constrain this changing structure for very asymmetric nuclei. Support from the experimental side is necessary for continued progress in this area, and the present work explores the structure of ^{19,21}C as indicated in Figure **??**.

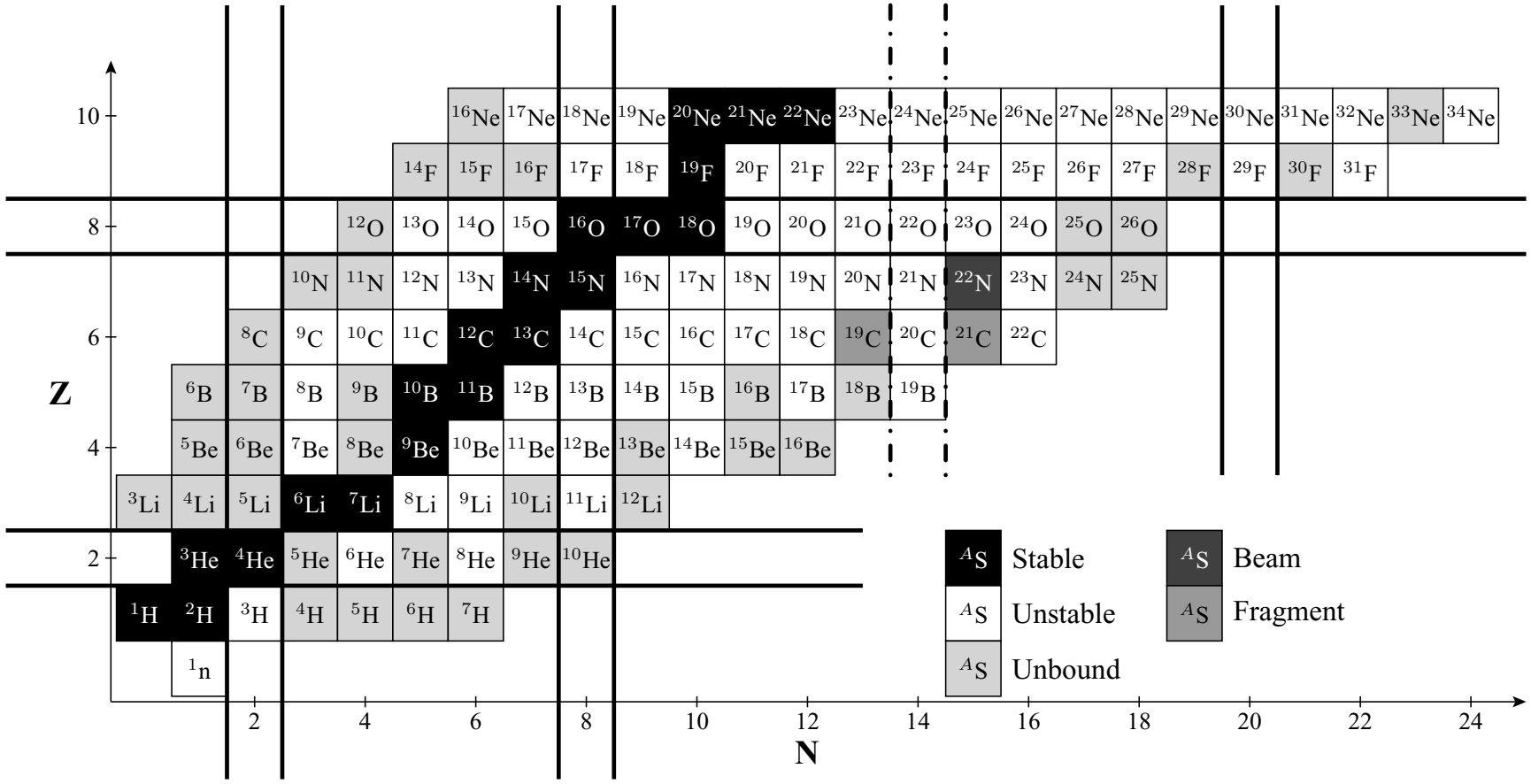

Figure 1.2: Chart of nuclides with "magic numbers" illustrated and this work's beam and reaction products of interest indicated.

Chapter 2

Theory and Motivation

2.1 Shell Model Calculations

As mentioned in Chapter 1, a successful method of describing the atomic nucleus is the nuclear shell model, in which the nucleons comprising the nucleus are treated as independent particles in a mean field. The choice of mean field for the present work's calculations is that of a Woods Saxons potential:

$$V(r) = \frac{V_0}{1 + e^{(r-R)/a}} \tag{2.1}$$

where V_0 is the potential depth of order -50 MeV, R is the nuclear radius of order $r_0 A^{1/3}$ where $r_0 \approx 1.2 - 1.4$ fm, and a is the diffuseness and generally is between 0.6 and 0.8 fm. A spin-orbit potential is also included to better reproduce data:

$$V_{SO} = -\frac{1}{r} V'(r) \vec{\ell} \cdot \vec{s} \tag{2.2}$$

as shown in Figure 1.1, this potential breaks the degeneracy of given ℓ-value states and performs well in describing the major shell structures near stability. More correlations must be included to reproduce observables away from closed shells as their structure

is not so simple. These typically take the form of two-body interactions and enter calculations by re-expressing the Hamiltonian as

$$H = H_0 + H_{res} \tag{2.3}$$

Where H_0 is the original mean-field Hamiltonian and H_{res} includes the modifications to the interaction

$$H_{res} = \frac{1}{2} \sum_{i,j=1}^{A} V_{ij} + \sum_{i=1}^{A} U(r_i) \tag{2.4}$$

where V_{ij} is the two-body interaction term and $U(r_i)$ is a central potential term. In principle the many-body system of equations can be solved with the above equations, but this is not a tractable problem for all but the lightest systems with current computational facilities. Therefore, some truncation of the model space is generally imposed, and an active area for the calculation defined where the two-body interactions are calculated. In this space, the total wavefunction Ψ_k for a system with quantum numbers $k = (n, \ell, j)$ is given by a linear combination of its basis states

$$\Psi_k = \sum_{\alpha} a_{k\alpha} |\Psi_\alpha\rangle \tag{2.5}$$

where α represents the basis state index and $|\Psi_\alpha\rangle$ represent the basis states themselves. Then, the Schrödinger equation may be written as

$$H|\Psi_k\rangle = E_k|\Psi_k\rangle \tag{2.6}$$

$$(H_0 + H_{res}) \sum_{\alpha} a_{\alpha k} |\Psi_\alpha\rangle = E_k \sum_{\alpha} a_{\alpha k} |\Psi_\alpha\rangle \tag{2.7}$$

and the inner product with $\langle\Psi_\beta| = \sum_\beta a_{\beta k}\langle\Psi_\beta|$ taken:

$$\sum_{\alpha,\beta} a_{\alpha k} a_{\beta k} \langle\Psi_\beta|H|\Psi_\alpha\rangle = E_k \sum_{\alpha,\beta} a_{\alpha k} a_{\beta k} \delta_{\alpha\beta} \tag{2.8}$$

This represents a system of equations which can be solved to find the eigenvalues E_k as well as matrix elements

$$H_{\alpha\beta} = \langle\Psi_\beta|H|\Psi_\alpha\rangle = \langle\Psi_\beta|H_0|\Psi_\alpha\rangle + \langle\Psi_\beta|H_{res}|\Psi_\alpha\rangle \tag{2.9}$$

Here, the two elements on the right side of 2.9 are known as the *bare (spherical) single particle energies* (SPE)

$$\langle\Psi_\beta|H_0|\Psi_\alpha\rangle = E^{(0)}_{\alpha\beta}\delta_{\alpha\beta} = E^{(0)}_\alpha \tag{2.10}$$

and *two-body matrix elements* (TBME) $\langle\Psi_\beta|H_{res}|\Psi_\alpha\rangle$. With this information in hand, the wavefunctions and other spectroscopic information can be calculated. The interaction used to generate the TBME can in principle be obtained from fundamental nucleon-nucleon interactions, and some progress is being made in this area (e.g. [6]). The interactions used for shell model calculations in this work are data-driven, which is to say that they are the result of fitting the interaction parameters over a large set of measured binding energies and low-lying states for nuclei in the vicinity of the calculation space. In particular, the WBP and WBT interactions used in this work have both been developed in this way, with special care taken because the interactions must describe *psd* cross-shell nuclei [7]. The interaction must cross over the proton p and neutron *sd* shells to properly describe the nuclei in this region. The WBP and WBT interactions differ only in the specific routine used to fit the interaction parameters.

In the following discussions, the contribution of the *tensor force* to H_{res} will be

particularly relevant. This force arises from spin-isospin coupling between nucleons, and takes the form

$$V_T = (\vec{\tau_1} \cdot \vec{\tau_2})([s_1 s_2]^{(2)} \cdot Y^{(2)}) f(r) \tag{2.11}$$

where τ is isospin, s is spin, and $[\,]^{(2)}$ represents the coupling of two operators to rank 2. This force is a significant driver in changes of nuclear structure away from stability [8, 9, 10]. The tensor force can be either attractive or repulsive between protons and neutrons depending on their orbital and total angular momenta, and modifies the binding energy of different orbitals accordingly. If the proton and neutron orbitals are denoted by $j_\pm$ and $j'_\pm$ respectively ($j_\pm = \ell \pm 1/2$), then the force is attractive for spin-flip partners $j_\pm$ and $j'_\mp$ and repulsive for $j_\pm$ and $j'_\pm$.

2.2 Shell Evolution Near N = 14

The formation and disappearance of nuclear shell gaps in exotic nuclei is currently a topic of great interest, as it affects numerous phenomena in nuclear physics and provides a tool to constrain theoretical descriptions of the nucleus. In light neutron-rich nuclei, it is now known that those nuclei with holes in the $\pi 0p_{1/2}$ and $\pi 0p_{3/2}$ subshells experience a smaller neutron-neutron interaction than theory predicts. This effect has been observed in Z=5-7 and N=10-15 [11, 12, 13]. In particular, the USD portion of the WBT interaction [7] has been shown to need empirical reductions of 12.5 - 25% of its TBME to describe the bound excited states of these nuclei. Similar reductions in TBME have been needed to reproduce magnetic moments measured in ^{17}B and ^{17}N [14].

2.2.1 N = 14 shell gap

N=14 has been shown to be a closed subshell for the oxygen isotopes [15]. The resulting large energy gap in ^{22}O is thought to occur because of attractive monopole matrix elements $V^{nn}_{d_{5/2}d_{5/2}}$ increasing the binding of the $\nu 0d_{5/2}$ relative to the $\nu 1s_{1/2}$. Figure 2.1 demonstrates the evolution of the shell gap as proton number is reduced by comparing the even-even Z=8 isotopic chain with the Z=6 one in two ways (taken from [12]). Panels (a) and (b) show the evolution of the 2^+ excited state energies in Z=8 and Z=6 taken from experimental data. Both follow a similar trend for N=8,10,12 but significantly differ for N=14, where Z=8 shows a significant increase in 2^+ energy while Z=6 does not. The energy of the 2^+ can be related to the energy needed to excite a neutron across the $\nu 0d_{5/2} - \nu 1s_{1/2}$ gap, which is why it grows for the closed subshell existing in Z=8. The lack of a significant rise in this energy for Z=6 suggests the gap is greatly diminished.

Figure 2.1(c) and (d) show this reduction from a slightly different perspective, and compare the effective single particle energies (ESPE) for the two isotopic chains calculated by shell model. It is readily observed that at N=14, there is a large energy gap between the $\nu 0d_{5/2}$ and $\nu 1s_{1/2}$ orbitals for Z=8 which is greatly reduced in Z=6. The driver for this vanishing gap is thought to be the tensor force, which serves to attractively couple the $\pi 0p_{1/2}$ and $\nu 0d_{5/2}$ orbitals while leaving the $\nu 1s_{1/2}$ unchanged. In Z=6 the attractive couplings are gone, which causes the $\nu 0d_{5/2}$ to be less bound relative to the $\nu 1s_{1/2}$.

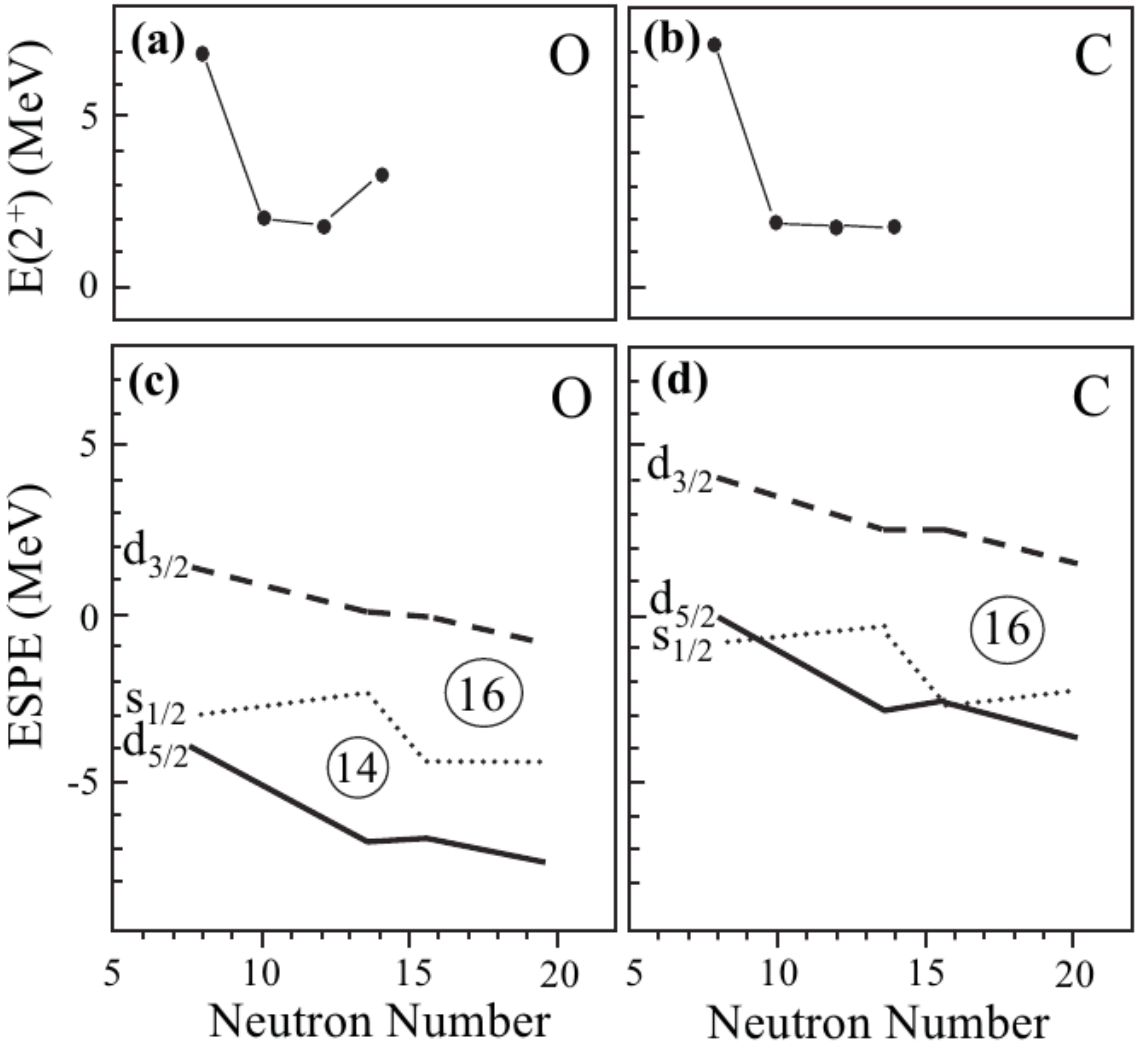

Figure 2.1: Collapse of the N=14 shell gap demonstrated in two ways by [12]. Top, a comparison of the measured 2^+ energies as a function of neutron number shows that at N=14 in oxygen (a) an increase occurs which is not matched in the carbon isotopic chain (b). Bottom, ESPEs calculated in the WBP interaction demonstrate the large gap between the $\nu 0d_{5/2}$ and $\nu 1s_{1/2}$ shells for N=14 gap in oxygen (c). In carbon, this gap is significantly diminished (d).

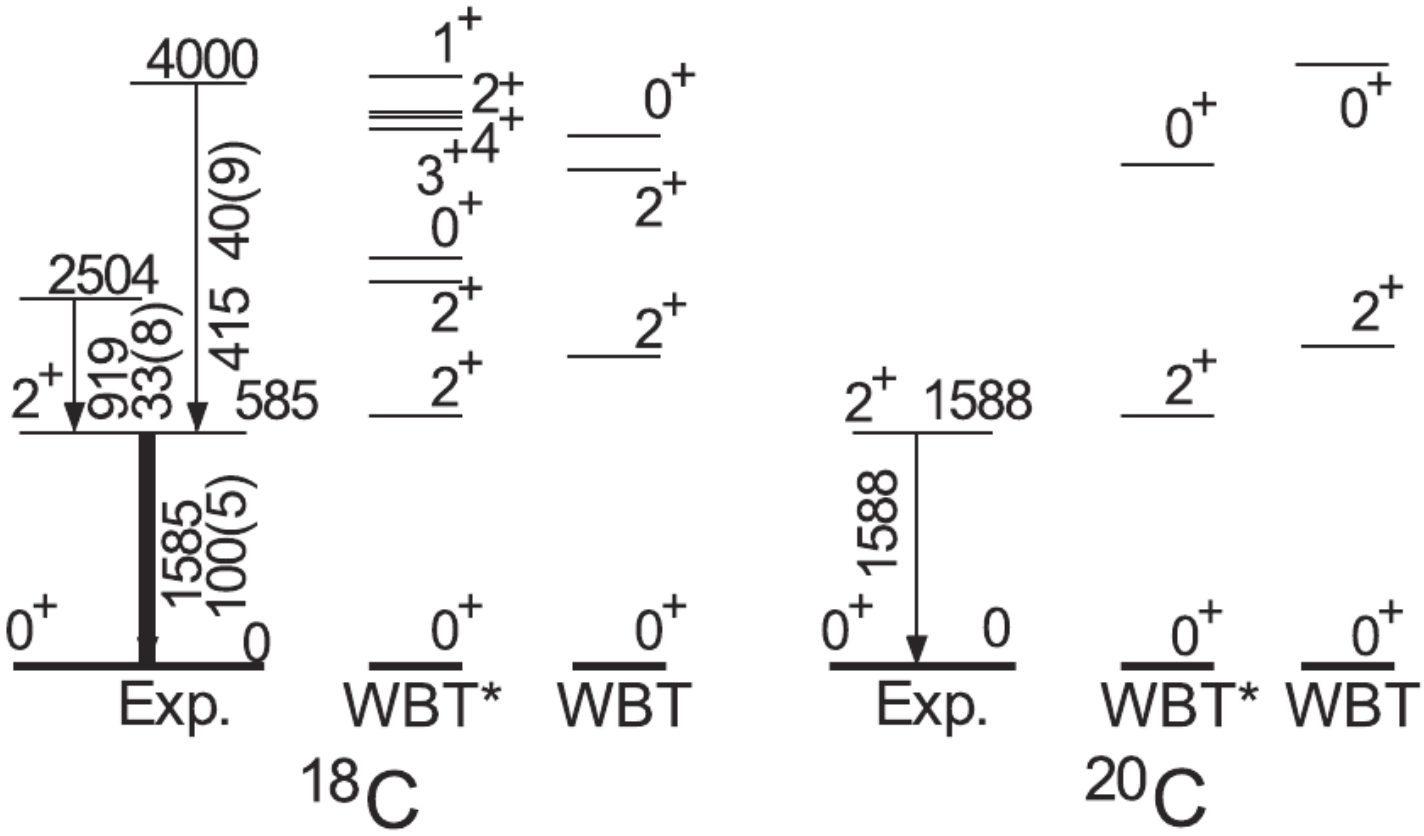

Figure 2.2: Comparison of ^{18,20}C experimental level schemes to WBT, WBT* interactions from [12].

While this serves to describe the overall structure of Z=6 relative to Z=8, it does not capture all changes. This can be seen in Figure 2.2, which compares experimental level schemes for ^{18,20}C with theoretical predictions [12]. The first comparison to be made is between experiment and the shell model interaction labelled WBT, which is a standard interaction to use when describing nuclei in this *psd* space. It is readily observed that the experimental level scheme is compressed relative to the theoretical one. This effect is observed systematically for Z=5-7 and N=10-15, and suggests a breakdown in the description of *psd* cross-shell nuclei within this theoretical framework. Empirical reductions of the neutron *sd* TBME associated with this interaction are capable of reproducing the level density in this region, with reductions varying between 12.5% for the Z=7 isotopic chain to 25% for Z=5,6. It has been suggested that the root cause of this systematic breakdown is related to the phenomenological nature of the WBT [11]. In particular, the very neutron rich *psd* cross shell nuclei are more loosely bound and have larger matter radii than those nuclei which were fit over to develop the interaction. The reduction in TBME for this interaction suggests that the interaction binds these nuclei too much. Therefore it is interesting to continue characterizing the nuclei in this region in order to more fully understand how the theoretical description of these nuclei breaks down.

^{19}C is a bound nucleus and lies adjacent to the N=14 nucleus ^{20}C on the nuclear chart, making it an interesting case to search for excited states with its proximity to the N=14 subshell closure and location within the *psd* cross-shell space described above. This nucleus has been the subject of prior study, of which three experiments have obtained excited state spectroscopic information by utilizing two different reaction mechanisms and experimental techniques. The first two experiments searched for bound excited states through γ-ray spectroscopy, with one [12] utilizing fragmentation and another [16] using proton inelastic scattering (p,p') on a liquid hydrogen target. The resulting γ-ray spectra are shown in Figure 2.3, with the former reaction

producing a γ line at 201 ± 15 keV and the latter reaction populating two lines at 72 ± 4 keV and 197 ± 6 keV.

Fast neutron spectroscopy has also been used in conjunction with (p,p') reactions on a liquid hydrogen target to look for neutron unbound excited states in ^{19}C [17]. The resulting decay spectrum is shown in Figure 2.4 and shows a clear resonance near 1 MeV. All together, the three experiments claim to have observed three different excited states in ^{19}C, and the resulting level scheme compared to theoretical calculations in Figure 2.5. The 200 keV γ-ray line has been assigned to a $3/2^+$, the 72 keV to a $5/2^+$ lying above the $3/2^+$, and the unbound resonance to the second $5/2^+_2$. There is, however, a question of why the fragmentation γ-ray spectroscopy experiment did not observe the 72 keV line that the (p,p') experiment did (shown in the figure as the red line corresponding to the $5/2^+_1$ state). No explanation is given in either publication to justify this difference, and as shall be seen in Section 5.1 cross section estimations for the two different reaction mechanisms cast further doubt on the 72 keV result.

As shown in Figure 2.5, a low lying triplet is predicted by shell model, followed by a large energy gap to the next state. Further, within the uncertainty of the theoretical calculations, it is possible that at least one state in the low-lying triplet be neutron unbound. Therefore, a new neutron spectroscopy experiment could remove the ambiguity in the observation of the $5/2^+_1$ state, and attempt to reproduce the location of the $5/2^+_2$ unbound state with a different reaction mechanism. Observation of a near-threshold resonance would demonstrate that the $5/2^+_1$ state is in fact neutron unbound, leaving ^{19}C with two bound states.

2.2.2 The N=15 Probe

The evolution of a shell gap for neutron number N can be extracted from the single particle or single hole levels in the N-1 or N+1 isotones, so the N=14 gap can be

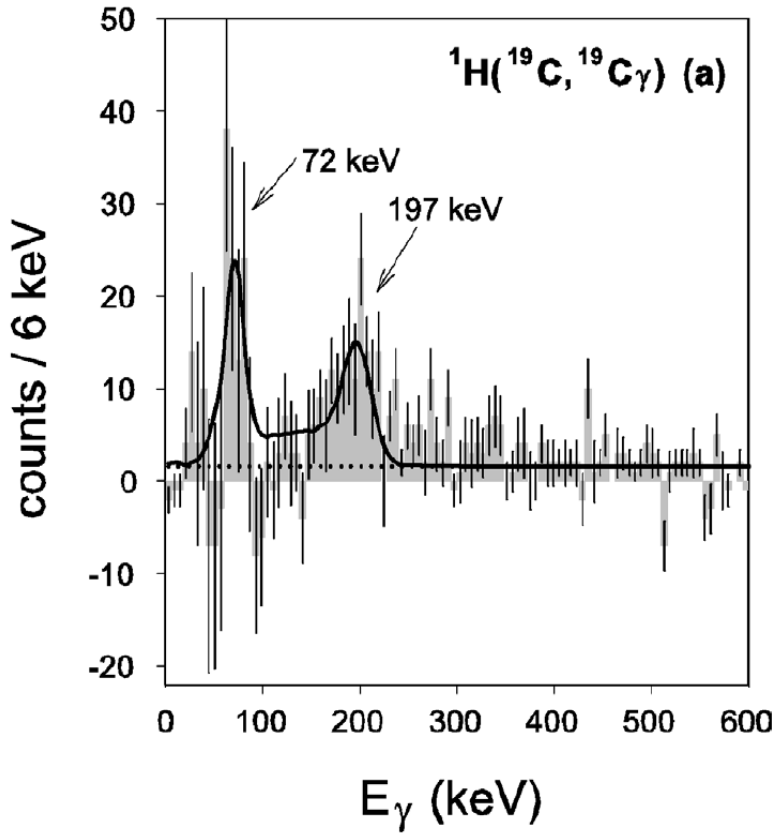

(a) (p,p')

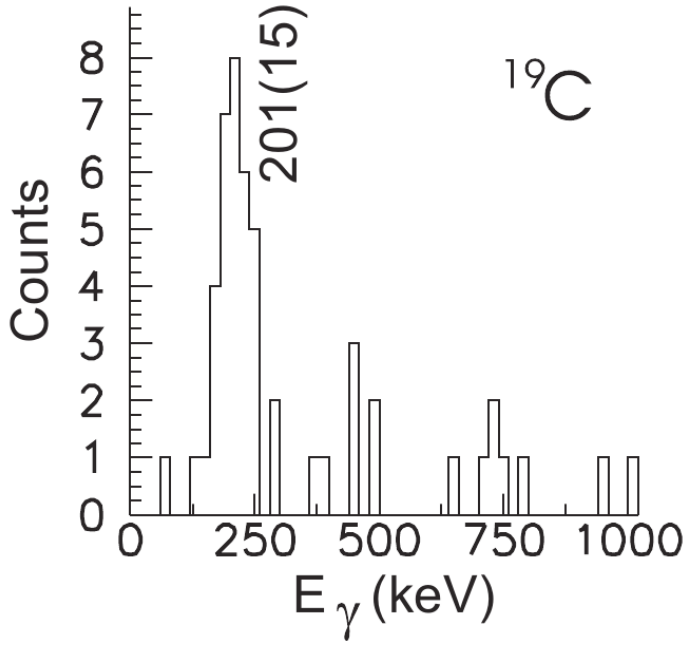

(b) Fragmentation

Figure 2.3: Resulting γ-ray spectrum for bound excited states in ^{19}C from [16] and [12].

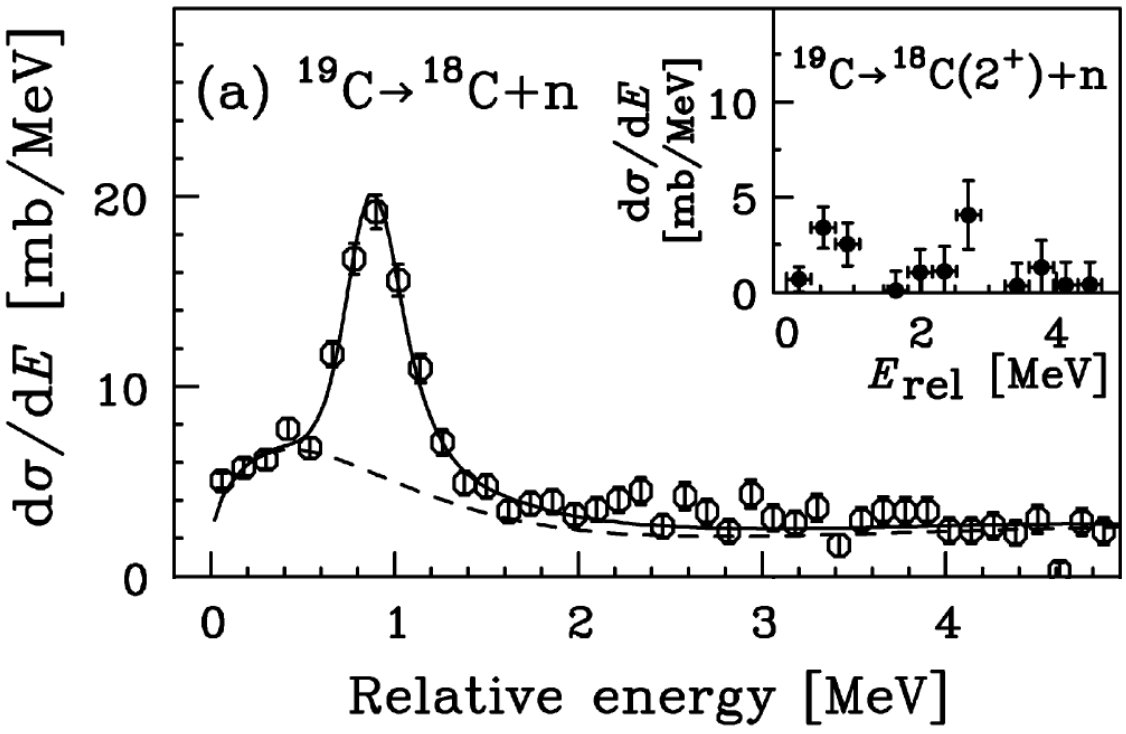

Figure 2.4: Resulting decay energy spectrum for unbound excited states in ^{19}C from [17].

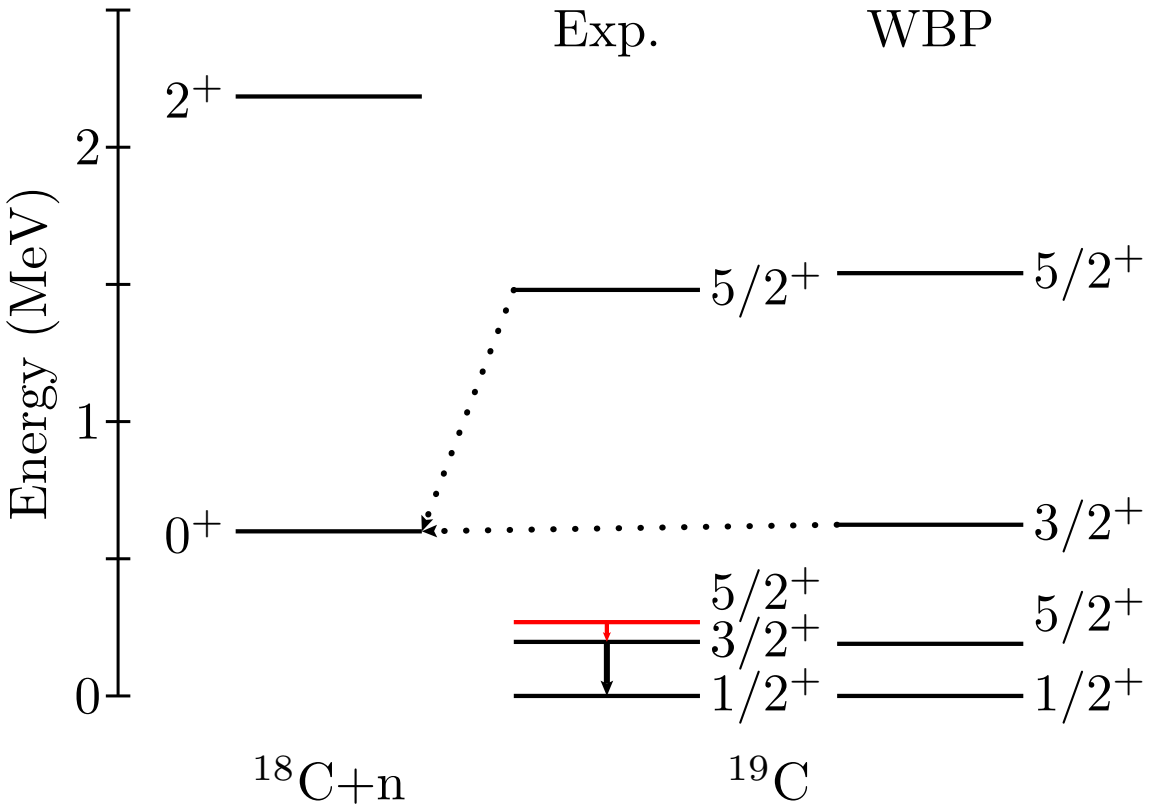

Figure 2.5: Experimental level scheme for ^{19}C based on results from [12, 16, 17]. For interpretation of the references to color in this and all other figures, the reader is referred to the electronic version of this dissertation.

probed by exploring the structure of N=15 isotones. The $\nu 1s_{1/2} - \nu 0d_{5/2}$ energy gap has been determined for ^{23}O and ^{22}N [18, 19], and it is useful to extend this measurement to ^{21}C with its empty $\pi p_{1/2}$ subshell. Prior to this work no spectroscopic information about ^{21}C was known. Figure 2.6 shows the measured energy gap for Z=8,7, where the level schemes are generated from measured states in [18, 13, 19]. A linear extrapolation to Z=6 as first used by [20] is shown as the dashed line, and predicts that the gap will vanish, suggesting degeneracy of the $\nu 1s_{1/2}$ and $\nu 0d_{5/2}$ orbitals. Within the uncertainty of the extrapolation it is possible for the levels to invert. The driver for this vanishing gap is again thought to be the tensor force, which serves to attractively couple the $\pi 0p_{1/2}$ and $\nu 0d_{5/2}$ orbitals while leaving the $\nu 1s_{1/2}$ unchanged. For Z=8, the $\pi 0p_{1/2}$ is full with its two protons, and Z=7 is one proton short and the $\nu 0d_{5/2}$ is correspondingly less bound relative to the $\nu 1s_{1/2}$. Therefore, the removal of a second proton would be expected to cause the $\nu 0d_{5/2}$ to be less bound by approximately the same amount as moving from Z=8 to Z=7. Measuring the $\nu 1s_{1/2} - \nu 0d_{5/2}$ shell gap in ^{21}C would directly test this.

Because Z=6 corresponds to a closed $\pi p_{3/2}$ subshell and N=15 naively corresponds to a full $\nu d_{5/2}$ shell plus one extra neutron, the energy difference between the $1/2^+$ ($\nu 1s_{1/2}$ particle state) and $5/2^+$ ($\nu 0d_{5/2}$ hole state) in ^{21}C directly determines this energy gap. Therefore, it is interesting to populate these two states in ^{21}C to experimentally determine the N=14 $\nu 1s_{1/2} - \nu 0d_{5/2}$ energy gap for carbon.

2.2.3 ^{22}C as a Two-neutron Halo

Since the discovery of the large matter radius of ^{11}Li [21], neutron halos have been a topic of intense study near the neutron drip line. The halo structure results from valence nucleon(s) being very loosely bound which, combined with the short range of the nuclear force, allows them to have a large probability of being found at distances much greater than the normal nuclear radius [22]. The separation energy for the

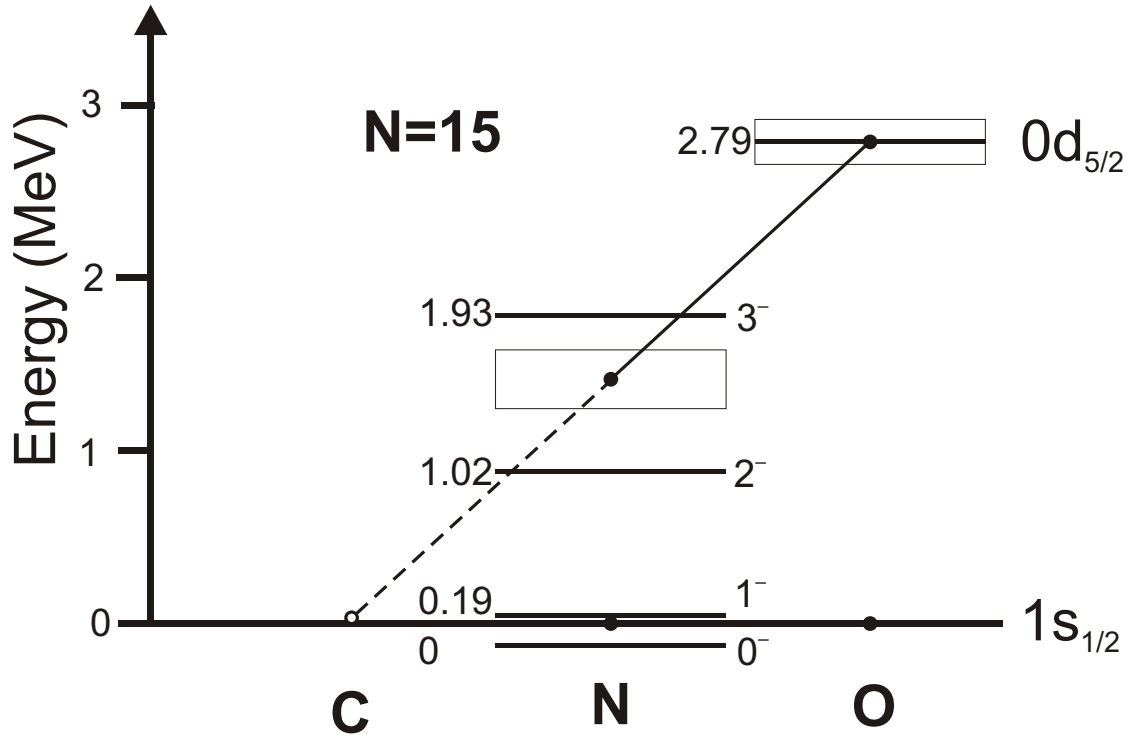

Figure 2.6: Evolution of the $\nu 1s_{1/2} - \nu 0d_{5/2}$ shell gap for N=15 oxygen, nitrogen, and carbon isotones. The dashed line shows a linear extrapolation of the gap to carbon following the prescription of [20], and experimental data are taken from [13, 18, 19].

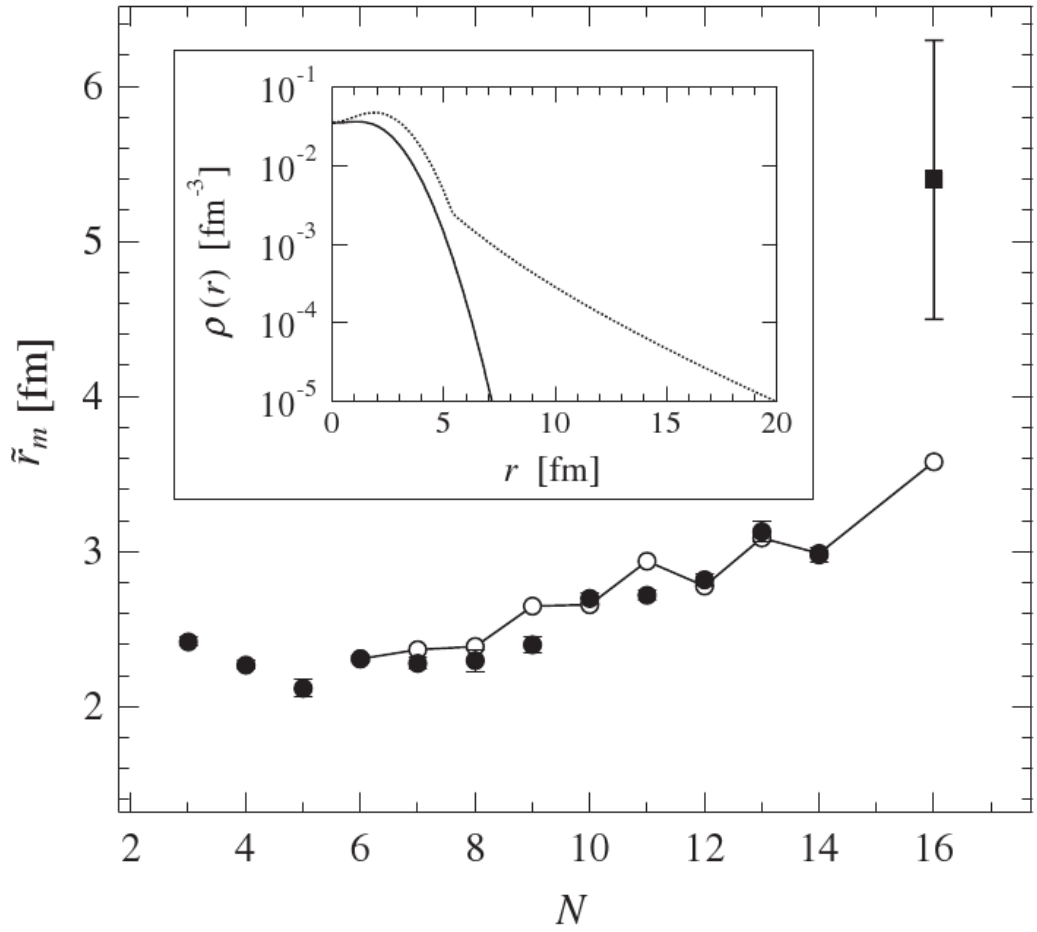

Figure 2.7: Matter radii for carbon isotopic chain, indicating a large increase for ^{22}C [26]. Inset show the matter density and demonstrates a large matter tail thought to be a neutron halo.

valence nucleon(s) is a critical parameter in understanding the halo structure [23, 24, 25].

Recently a large matter radius has been extracted from the measured reaction cross section of ^{22}C via finite-range Glauber analysis under an optical-limit approximation, suggesting that this nucleus exhibits a two-neutron halo [26]. Figure 2.7 shows matter radii for the carbon isotopic chain as a function of neutron number including the latest measurement of ^{22}C from [26]. For N $<$ 16, a fairly regular and compact form is observed but a large discontinuity exists at N = 16, which corresponds to ^{22}C.

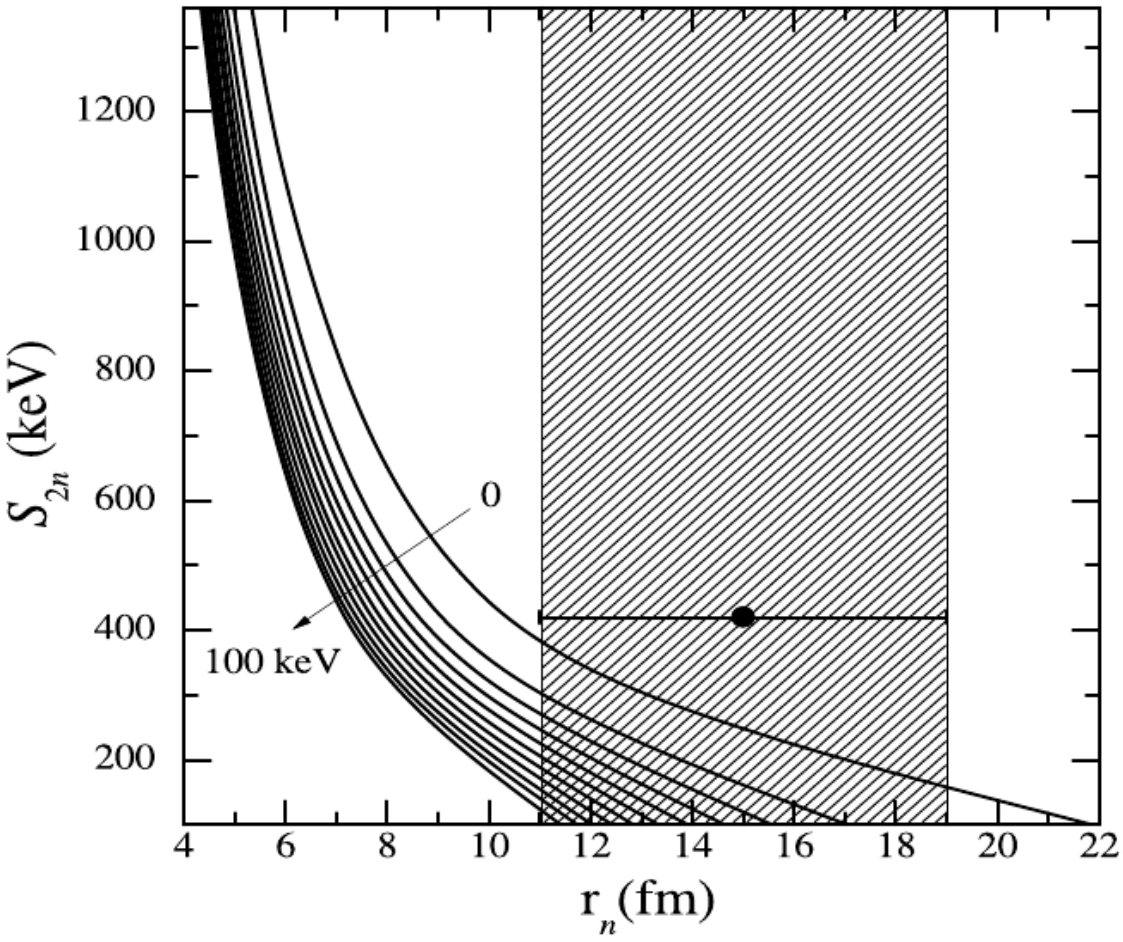

Figure 2.8: Correlations between the two-neutron separation energy and rms neutron halo radius in ^{22}C for given positions of a virtual state in ^{21}C from [27]. Each curve is calculated for a specific energy of the ^{21}C virtual state, and range from 0 to 100 keV in steps of 10 keV.

Inset, the figure shows the extracted proton (solid line) and neutron (dotted) density line shapes. The neutron density extends out to a great distance from the core of the nucleus and suggests a halo with two neutrons in the $\nu 1s_{1/2}$ orbital.

The two-neutron separation energy (S_{2n}) has not yet been measured, but it has been shown that constraints on the S_{2n} of ^{22}C can be placed by measuring the energy of the virtual state in ^{21}C. Recently, Yamashita *et al.* derived a relationship between the ^{22}C two-neutron separation energy and the energy of the virtual state in ^{21}C

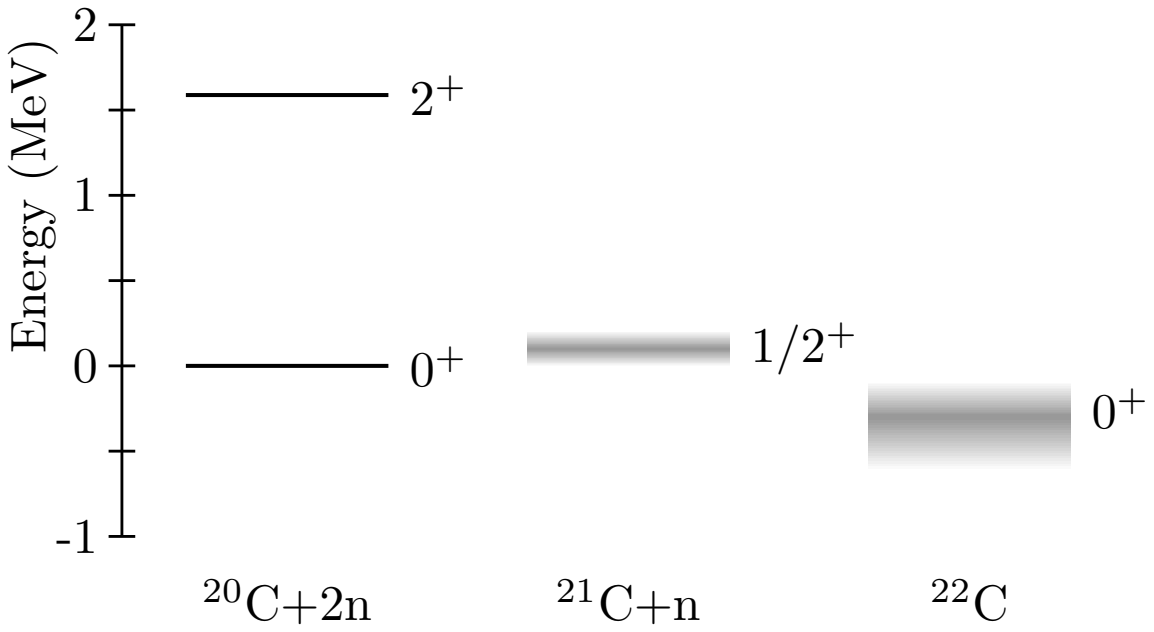

Figure 2.9: Level scheme indicating the predicted locations of ^{21,22}C in energy relative to a ^{20}C core [27].

within the renormalized zero-range three-body model of [27]. Figure 2.8 demonstrates this relationship as lines of constant decay energy for the virtual state in ^{21}C through a phase space of two-neutron separation energy S_{2n} and ^{22}C halo radius r_n. This sort of correlation has been observed in other halo systems [28]. The lines shown correspond to ^{21}C virtual state energies ranging from 0 to 100 keV in steps of 10 keV. The hashed region indicates constraints on this parameter space from [26].

Prior to this work no spectroscopic information about ^{21}C was known, but Yamashita *et al.* suggest that the virtual state should be unbound by less than 100 keV [27]. Their reasoning is shown in Figure 2.8. The 100 keV virtual state curve crosses into the experimentally constrained region at approximately $S_{2n} = 100$ keV, which limits the range of predicted virtual state energies in ^{21}C to $E \leq 100$ keV for this calculation space. Their predictions are illustrated schematically in Figure 2.9, which shows the predicted ground states of ^{21,22}C relative to ^{20}C as a level scheme. Therefore it is interesting to measure the location of the virtual state in ^{21}C to test

this model and provide constraints on the S_{2n} for ^{22}C.

2.3 Decay Energy Lineshapes

In order to extract information from the measured decay energy spectra, the observed line shapes must be modelled in such a way that the input parameters can be related to physics observables. In the present work, there were three possible contributions to the line shapes: narrow resonance structures resulting from the breakup of $\ell = 2$ states, broader virtual resonances arising from the decay of $\ell = 0$ states, and nonresonant background contributions from the decay of high-lying continuum states.

2.3.1 Breit-Wigner Resonance

It is possible to model the decay of a neutron unbound state as the scattering of a neutron from the fragment nucleus with the energy and angle as variables. This description of the breakup can be constructed mathematically within the R-matrix framework [29], and an expression for the cross section as a function of energy $\sigma(E)$ can be derived. While the full derivation of the most general case is beyond the scope of this work, the relevant portions for this work are highlighted below (full details available in [29], and the notation here is kept consistent wherever possible).

The scattering of the neutron from the charged fragment can be modelled as the neutron scattering elastically from some central potential. The radial Schrödinger equation for this situation then reads:

$$\left[\frac{d}{dr^2} - \frac{\ell(\ell+1)}{r^2} - \frac{2M}{\hbar^2}(V-E)\right] u_\lambda(r) = 0 \tag{2.12}$$

This equation has solutions in the form of incoming and outgoing waves I_ℓ and O_ℓ which are Coulomb Hankel functions [30]. The R-matrix formalism is constructed

by exploiting the properties of the wavefunction at the core's "surface," defined as the minimum radial distance between the neutron and core at which the nuclear interaction is unimportant:

$$a = r_0(A_c^{1/3} + A_n^{1/3}) \tag{2.13}$$

Here, r_0 is a parameter describing the nuclear radius and is taken to be 1.4 fm, and A_C and A_n are the mass numbers for the core and neutron respectively. A Green's theorem relation can be used to construct an expression for the relationship between the wavefunction anywhere in the interior of the core and its derivative at the surface for any given energy E:

$$u_E(r) = G(r, a)(adu_E/dr)a \tag{2.14}$$

where

$$G(r, a) = \frac{\hbar^2}{2Ma} \sum_\lambda \frac{u_\lambda(r)u_\lambda(a)}{E_\lambda - E} \tag{2.15}$$

and λ is the index for eigenfunctions for the interior wavefunction which will combine with a shift function to define the locations of observed resonances. The R-matrix then can be defined:

$$R = G(a, a) = \sum_\lambda \gamma_\lambda^2/(E_\lambda - E) \tag{2.16}$$

where

$$\gamma_\lambda = (\hbar^2/2Ma)^{1/2}u_\lambda(a) \tag{2.17}$$

This can be related to a collision matrix U_ℓ

$$U_\ell = \frac{I_\ell}{O_\ell}\frac{1 - L_\ell^* R_\ell}{1 - L_\ell R_\ell} = \exp(2i\delta_\ell) \tag{2.18}$$

where L_ℓ is the logarithmic derivative of O_ℓ:

$$L_\ell = \left.\frac{\rho u'^{\text{out}}_\ell}{u^{\text{out}}_\ell}\right|_{r=a} = S_\ell + iP_\ell \tag{2.19}$$

where S_ℓ is known as a shift factor and P_ℓ as a penetration factor. In the one-level approximation where it is assumed that the spacing between resonances is much larger than their width, the phase shift then is:

$$\delta_\ell = \tan^{-1}\left(\frac{\frac{1}{2}\Gamma_{\lambda\ell}}{E_{\lambda\ell} + \Delta_{\lambda\ell} - E}\right) - \phi_\ell \tag{2.20}$$

where ϕ_ℓ is the hard-sphere scattering phase shift, and

$$\Gamma_{\lambda\ell} = 2\gamma^2_{\lambda\ell} P_\ell \tag{2.21}$$

$$\Delta_{\lambda\ell} = -\gamma^2_{\lambda\ell} S_\ell \tag{2.22}$$

$\Gamma_{\lambda\ell}$ determines how fast the phase changes as E passes through a resonance and therefore defines the width, while $\Delta_{\lambda\ell}$ determines how far the resonance energy is shifted from its eigenvalue $E_{\lambda\ell}$. With the collision function U_ℓ thus completely defined, the cross section can be expressed:

$$\sigma_\ell = \int \sigma(\theta) d\Omega = \frac{\pi}{k^2}\sum_\ell (2\ell+1)|1 - U_\ell|^2 \tag{2.23}$$

$$= \frac{\pi}{k^2} g_j \frac{\Gamma_{\lambda\ell}\Gamma_{\lambda\ell'}}{(E_{\lambda\ell} + \Delta_{\lambda\ell} - E)^2 + \frac{1}{4}\Gamma^2_{\lambda\ell}} \tag{2.24}$$

Because only the relative intensity rather than the absolute cross section is needed for fitting purposes, we collect all constants which serve as scaling factors and write

$$\sigma_\ell = A\frac{\Gamma_\ell}{(E_\ell + \Delta_\ell - E)^2 + \frac{1}{4}\Gamma^2_\ell} \tag{2.25}$$

where

$$\Gamma_\ell = 2\gamma_{\ell\ell}^2 P_\ell \tag{2.26}$$

and

$$\Delta_\ell = -\gamma_{\ell\ell}^2 S_\ell \tag{2.27}$$

which is the Breit-Wigner distribution with an energy dependent width. For this expression, we make the one-level approximation stronger by restricting γ to only include a single eigenfunction of the interior wavefunction. When the resonances are widely spaced this approximation is valid.

2.3.2 S-wave Dynamics

The Breit-Wigner line shape derived above does not describe $\ell = 0$ transitions well, as the lack of an angular momentum barrier causes them to have a broad energy distribution - particularly for high lying states. Therefore, some other mechanism for the description of these transitions must be used if we are to account for their presence in the decay spectra. It is possible to treat the neutron evaporation as the breakup of the projectile by the neutron being knocked out from the projectile by the neutron-target interaction, and then re-interacting from its final state with the core. This model is developed by Blanchon *et al.* in [31], and the highlights of that work are presented here. The coordinate system used for the following calculations is displayed in Figure 2.10.

First order time-dependent perturbation theory defines a transition amplitude for inelastic-like excitations of the form we wish to describe,

$$A_{fi} = \frac{1}{i\hbar} \int_{-\infty}^{\infty} dt \left\langle \psi_f(\mathbf{r}, t) \middle| V_2(\mathbf{r} - \mathbf{R}(t)) \middle| \psi_i(\mathbf{r}, t) \right\rangle \tag{2.28}$$

where ψ_i and ψ_f are the wavefunctions for the initial and final states respectively,

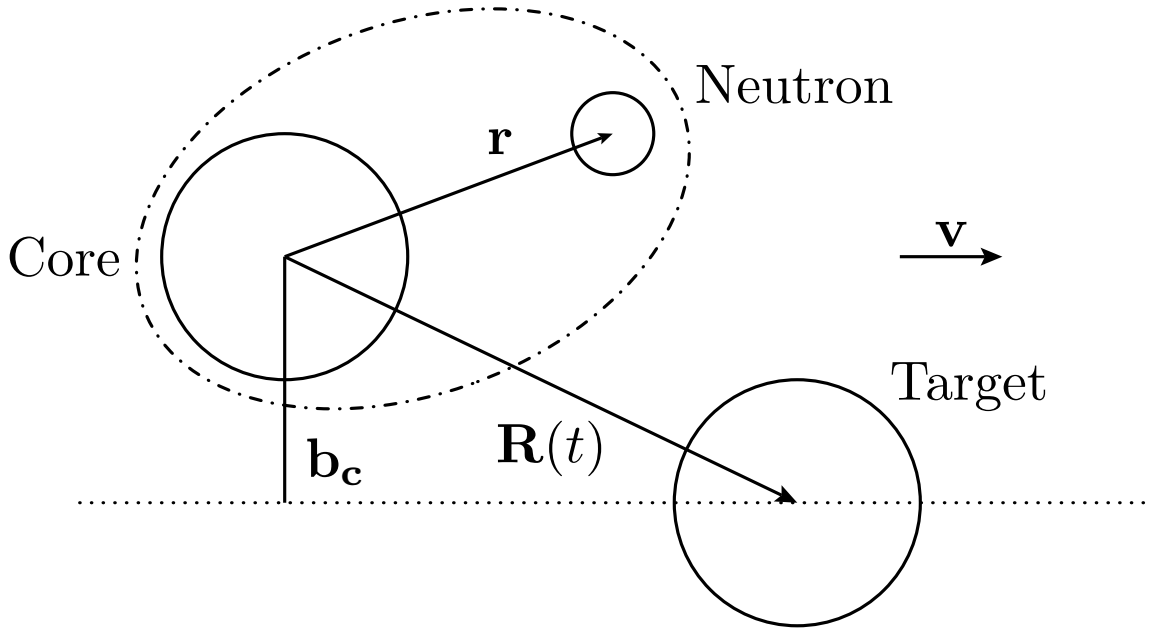

Figure 2.10: Coordinate system and associated parameters for s-wave calculations.

and ψ_f can be either a bound or continuum state. The potential $V_2(\mathbf{r}-\mathbf{R}(t))$ is the interaction which causes the transition and moves past the core/neutron system with velocity v in the z-direction with impact parameter b_C, which is taken to be in the x-direction with $y=0$. Factorizing $\psi_i(\mathbf{r},t)=\phi_i(\mathbf{r})e^{-\frac{i}{\hbar}\epsilon_i t}$, and introducing variables $z-vt=z'$ and $t=(z-z')/v$, the transition amplitude is re-expressed as

$$A_{fi}=\frac{1}{i\hbar v}\int_{t\infty}^{\infty} dxdydzdz'\phi_f^*(x,y,z)\phi_i(x,y,z)e^{iq(z-z')}V_2(x-b_C,y,z') \qquad (2.29)$$

where

$$q=\frac{\epsilon_f-\epsilon_i}{\hbar v} \qquad (2.30)$$

Choosing $V_2(r)$ to be a delta function $V_2(r)=v_2\delta(x)\delta(y)\delta(z)$ with strength v_2, the

integrals for x and y are can be calculated:

$$A_{fi} = \frac{v_2}{i\hbar v} \int_{-\infty}^{\infty} dz \phi_f^*(b_C, 0, z)\phi_i(b_C, 0, z)e^{iqz} \tag{2.31}$$

The δ-function approximation holds best for peripheral reactions (see [31] for more detail). Further defining $\gamma = \sqrt{-2m\epsilon_i}/\hbar$ as the decay length of the initial state and $k = \sqrt{2m\epsilon_f}/\hbar$ as the final momentum in the continuum, and now imposing the restriction of $\ell_i = \ell_f = 0$ results in the following expressions for the wavefunctions:

$$\phi_i(b_C, 0, z) = -\frac{C_i}{4\pi}\frac{e^{-\gamma r}}{r} \tag{2.32}$$

$$\phi_f(b_C, 0, z) = \frac{C_f}{4\pi} i\frac{k}{2}(h_0^{(-)}(kr) - Sh_0^{(+)}(kr)) \tag{2.33}$$

where C_* are normalization coefficients and S is the S-matrix corresponding to the final state interaction of the neutron with the core. With this, the expression for the transition amplitude reads:

$$A_{fi} = -\frac{v_2}{\hbar v}\frac{C_i C_f}{8\pi} I(k, q) \tag{2.34}$$

where

$$I(k, q) = \int_{-\infty}^{\infty} dz \frac{e^{-(\gamma - ik)r} - S^* e^{-(\gamma + ik)r}}{r^2}\cos(qz) \tag{2.35}$$

The probability spectrum to excite a final state then can be expressed:

$$\frac{dP_{in}}{d\epsilon_f} = \frac{2}{\pi}\frac{v_2^2}{\hbar^2 v^2} C_i^2 \frac{m}{\hbar k}\frac{1}{2\ell_i + 1}\sum_{m_i, m_f} |1 - \bar{S}_{m_i, m_f}|^2 |I_{m_i, m_f}|^2 \tag{2.36}$$

where

$$\bar{S} = Se^{2iv} = e^{2i(\delta + v)} \tag{2.37}$$

Finally, the expression for the cross section reads

$$\frac{d\sigma_{-1n}}{d\epsilon_f} = C^2 S \int d\mathbf{b}_C \frac{dP_{in}(b_C)}{d\epsilon_f} P_{ct}(b_C) \tag{2.38}$$

where

$$P_{ct}(b_C) = |S_{ct}|^2 = e^{-\ln 2 \exp[(R_s - b_C)/a]} \tag{2.39}$$

and the strong absorption parameter $R_s \approx 1.4(A_p^{1/3} + A_t^{1/3})$ fm is the distance of closest approach for a trajectory which is 50% absorbed from the elastic channel and $a = 0.6$ fm is the diffuseness. For large impact parameters, the approximation $r = \sqrt{b_C^2 + z^2} \approx b_C + z^2/2b_C$ can be made, which allows for a simple analytic expression for the cross section:

$$\frac{d\sigma}{d\epsilon} \sim \frac{1}{k(\gamma^2 + k^2)} \left(\frac{k\cos\delta + \gamma \sin\delta}{\sqrt{\gamma^2 + k^2}} \right) \tag{2.40}$$

In principle the phase shift δ comes from the calculated S-matrix, but an approximation of $\delta = a_S k$ can be used as a parameterization. As discussed in [31] this approximation slightly over predicts the cross section for higher decay energies, but as discussed in [32] still agrees very well with a full calculation. We therefore have an expression for the decay energy as a function of the variables a_S, γ, and k, where a_S is the scattering length, γ is the decay length and is related to the beam's binding energy as discussed above, and k is related to the decay energy. For any given decay energy calculation, a_S and γ are fixed, which results in a decay energy line shape which can be used for fitting experimental data.

2.3.3 Nonresonant Contributions

In the case of ^{19}C, there is the possibility of background which is uncorrelated with the population of a particular state. This background arises from the population

of high-lying continuum states in ^{20,21}C where the level density is large. These states can evaporate neutrons until the ^{18}C core is reached, and if the neutron(s) resulting from this decay scheme are detected, they will contribute to some sort of background distribution. Figure 2.11 diagrammatically shows this effect. The thick lines correspond to chains of high-lying continuum states evaporating neutrons to other continuum states by the emission of a fairly low energy neutron. These neutrons are more likely to be detected because their relative energy is small and therefore are more likely to make it into the geometric acceptance of the experimental setup. The thin line represents the final decay mode to the ground state of ^{18}C from a high-lying continuum state. This mode is unlikely to be observed because of its high relative energy kick, which will very likely cause its trajectory to lie outside of the setup's acceptances.

Therefore, the background neutrons are unlikely to be directly correlated with the ^{18}C, and result from neutron evaporations through regions of high level density. This lends itself to a statistical model approach, and can be modelled as a Maxwellian distribution [33]. The general approach to this sort of model is summarized below, with full details being covered in [34]. The notation below will conform to [34] wherever possible.

The probability of system C to decay through a specific reaction channel β can be written

$$G_C(\beta) = \frac{k_\beta^2 \sigma_C(\beta)}{\sum_\gamma k_\gamma^2 \sigma_C(\gamma)} \tag{2.41}$$

where the sum of over all possible channels γ, $k = \lambda^{-1}$ is the wave number, and σ_C is the cross section for C to decay. Then, the kinetic energy for channel β with residual nucleus Y is expressed:

$$\epsilon_\beta = \epsilon_{\mathrm{nY}} - E_\beta^* \tag{2.42}$$

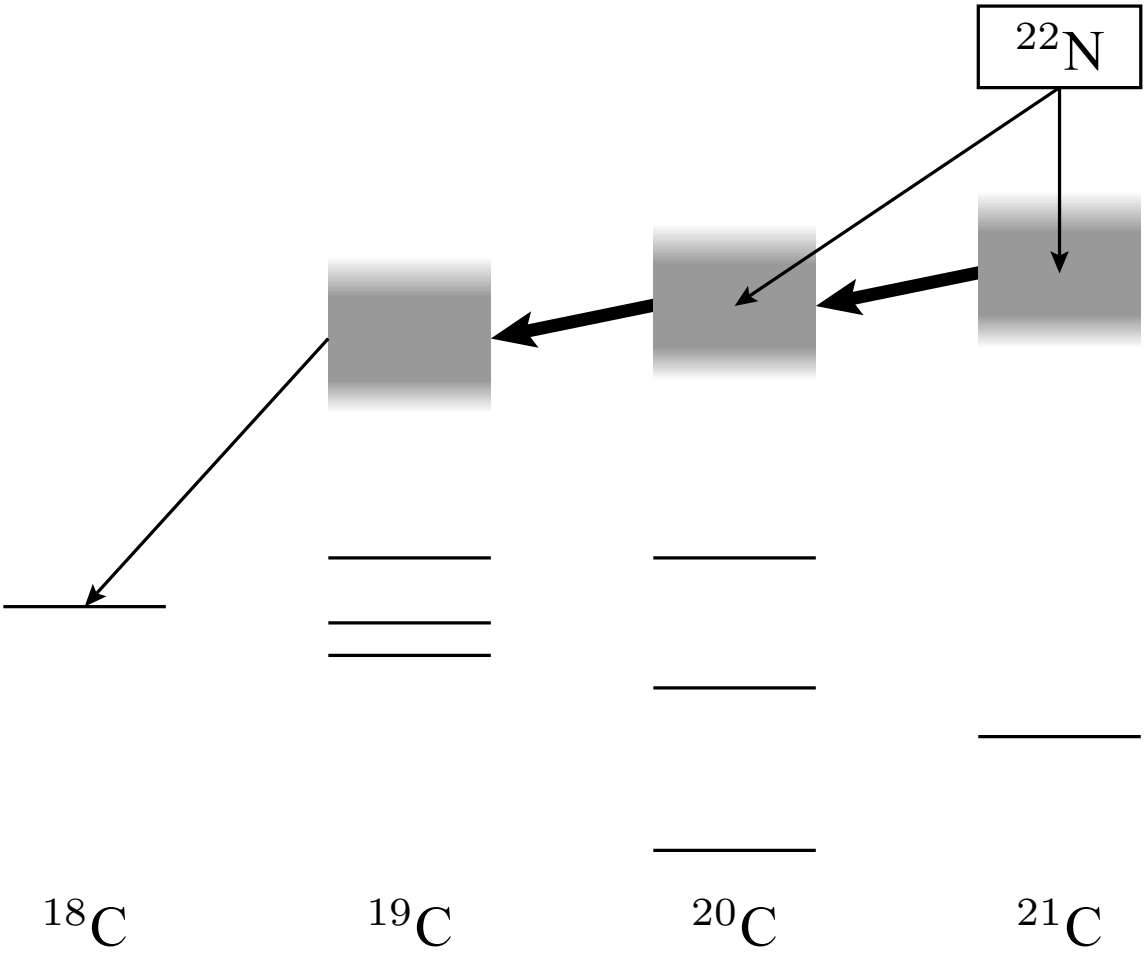

Figure 2.11: Diagrammatic representation of how nonresonant background arises in the decay spectrum for ^{18}C in coincidence with neutrons. Highly excited states in ^{20,21}C are populated by nucleon removal from the ^{22}N beam, and these evaporate neutrons to other high-lying states until ^{19}C* is reached (thick arrows). ^{19}C* decays via emission of a neutron with large decay energy (thin arrow), which is unlikely to be observed because of the geometric efficiency of the setup. Evaporation between continuum states results in neutron emission with lower relative energy, which is likely to be observed and results in background.

where

$$\epsilon_{\mathrm{nY}} = \epsilon + Q_\beta \tag{2.43}$$

and ϵ is the energy of the incoming beam and Q_β is the Q-value of the reaction, and E^*_β is the excitation of the residual nucleus. For a high density of states, the distribution of emitted neutrons between ϵ and $\epsilon + d\epsilon$ is

$$G_n(\epsilon)d\epsilon = \sum_{\epsilon < \epsilon_\beta < \epsilon + d\epsilon} G_C(\beta) \tag{2.44}$$

Because we are interested in a line shape rather than an absolute cross section, we consider only the numerator of 2.41 and write the relative intensity I as

$$I_n(\epsilon)d\epsilon \sim \epsilon \sigma_C(\beta) w_{\mathrm{Y}}(\epsilon_{\mathrm{nY}} - \epsilon)d\epsilon \tag{2.45}$$

where ϵ replaces k^2_β and w is related to the level density. The shape of I can be estimated by taking the Taylor expansion of logarithm of w about ϵ_{nY}:

$$\mathscr{G}(\epsilon_{\mathrm{nY}} - \epsilon) = \log w(\epsilon_{\mathrm{nY}} - \epsilon) = \mathscr{G}(\epsilon_{\mathrm{nY}}) - \epsilon \left(\frac{d\mathscr{G}}{dE} \right)_{E=\epsilon_{\mathrm{nY}}} + ... \tag{2.46}$$

this expansion results in the following expression for I

$$I_{\mathrm{n}}(\epsilon)d\epsilon \sim \epsilon \sigma_C(\epsilon) \exp\left[-\frac{\epsilon}{\Theta(\epsilon_{\mathrm{nY}})} \right] d\epsilon \tag{2.47}$$

where σ_C is a slowly varying function which can be absorbed into the constant, and

$$\frac{1}{\Theta(E)} = \frac{d\mathscr{G}}{dE} \tag{2.48}$$

Therefore, Θ has units of energy and can be interpreted as a nuclear temperature of a thermal neutron source. The dominant feature of this expression is the $e^{-\epsilon/\Theta}$

exponential term. The function used in this work's background modelling is slightly different [35]:

$$f(\epsilon) = \text{const}\sqrt{\epsilon/\Theta^3}e^{-\epsilon/\Theta} \tag{2.49}$$

with parameter Θ a parameter which is fit to the data. The differences in line shape between 2.47 and 2.49 are irrelevant once experimental resolutions are accounted for.

2.4 Estimators: Maximum Likelihood Method

Physics observables were extracted in this work by comparing simulated datasets to the experimental data. Some statistical estimator method was needed to provide tests to compare the simulated and experimental datasets, and the method chosen for this work is the maximum likelihood method. The simulated dataset served to generate a decay energy probability density functional (p.d.f.) $f(\theta)$, where θ is the set of parameters being fit over. The likelihood can then be defined as in [36]:

$$L(\mathbf{X}|\theta) = \prod_{i=1}^{N} f(X_i|\theta) \tag{2.50}$$

where $\mathbf{X} = X_1, X_2, ..., X_N$ is the set of N observations and $f(X_i|\theta)$ is the value of the p.d.f. evaluated at each data point. While $L(\mathbf{X}|\theta)$ and the log-likelihood $\ln L(\mathbf{X}|\theta)$ both provide good test statistics, $\ln L(\mathbf{X}|\theta)$ was used as a test statistic for this work:

$$\ln(L(\mathbf{X}|\theta)) = \sum_{i=1}^{N} \ln(f(X_i|\theta)) \tag{2.51}$$

$L(\mathbf{X}|\theta)$ was maximized by generating a likelihood surface over the relevant decay parameters by populating grid points in the decay parameter phase space with individual simulation runs from which the maximum likelihood could be extracted. The

$n\sigma$ confidence intervals defined as the regions where

$$\ln(L(\mathbf{X}|\theta))_{max} - \ln(L(\mathbf{X}|\theta)) \leq \frac{n^2}{2} \tag{2.52}$$

In order to reduce systematic errors due to modelling deficiencies, the simulated datasets were large and the simulation verified for simple cases before modelling the reactions of interest (more detail in Section 4.5).

Chapter 3

Method

3.1 Invariant Mass Reconstruction

Neutron unbound states decay on very short timescales (order 10^{-21} s), which prevents the direct observation of these nuclei. One way the study of such nuclei can proceed is by the observation of decay products and reconstruction of the properties of the original state. The technique used to perform this reconstruction is that of invariant mass spectroscopy, which is derived from relativistic mechanics. The relativistic four-momentum $\mathbf{P}$ is defined:

$$\mathbf{P} = (E, \mathbf{p}) \tag{3.1}$$

Where E is the total energy and $\mathbf{p}$ is the three-momentum vector. For state i decaying to products f and n (schematically shown in Figure 3.1), conservation of momentum is expressed as

$$\mathbf{P}_i = \mathbf{P}_f + \mathbf{P}n \tag{3.2}$$

and the invariant mass M can be defined in terms of the squares of 3.2

$$M^2 = (\mathbf{P}_f + \mathbf{P}_n)^2 = (E_f + E_n)^2 - |\mathbf{p}_f + \mathbf{p}_n|^2 \quad (3.3)$$

$$= m_f^2 + m_n^2 - 2(E_f E_n - \mathbf{p}_f \cdot \mathbf{p}_n) \quad (3.4)$$

The decay energy can be found by subtracting off the rest masses of the fragment and neutron

$$E_{decay} = M - m_f - m_n = \sqrt{m_f^2 + m_n^2 - 2(E_f E_n - \mathbf{p}_f \cdot \mathbf{p}_n)} - m_f - m_n \quad (3.5)$$

In order to reconstruct the decay energy, the full four-momentum of the fragment and neutron must be measured. Therefore, the objectives of the experimental setup are twofold: to identify particular reaction products and to measure the decay residue four-momenta.

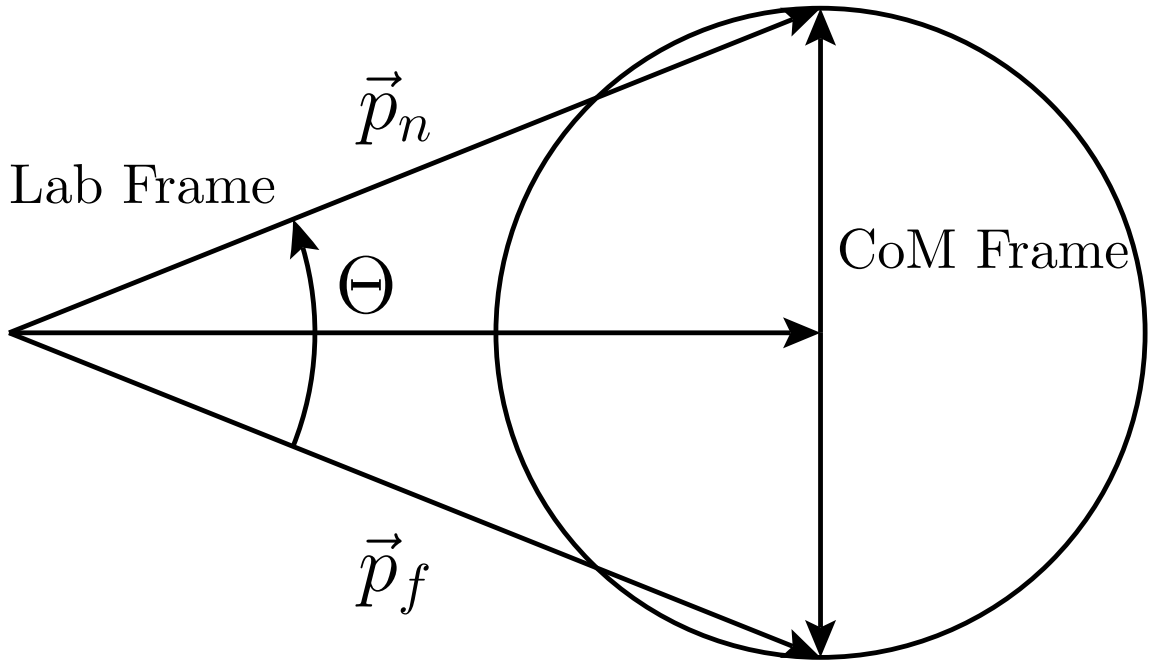

Figure 3.1: Neutron evaporation schematic.

3.2 Beam Production

Population of states in ^{19,21}C was performed by single proton removal from a beam of ^{22}N, a nucleus which is β-unstable with a half-life of 20 ± 2 ms [37]. The NSCL makes use of the fast fragmentation method [38] to produce beams with such short half-lives. The application of this method at the Coupled Cyclotron Facility (CCF) [39] is schematically shown in Figure 3.2.

The primary ^{48}Ca beam was injected from the ion source into the K500 cyclotron, where it was accelerated to 12.5 MeV/A. From there, it was sent through a thin foil which fully stripped it of electrons and injected to the K1200 cyclotron, where ^{48}Ca was accelerated to the nominal primary beam energy of 140 MeV/u. The beam was then extracted from the K1200 and transported to the object position of the A1900 fragment separator [40], where it impinged on a 2068 mg/cm^2 ^{9}Be production target.

The A1900 separates reaction fragments by their momentum and m/q ratios by setting the four dipole magnets of the separator to the expected magnetic rigidity of the final ^{22}N secondary beam. In this experiment, the final dipole was set to a rigidity of 3.856 Tm. A 1057 mg/cm^2 Al wedge degrader was placed after the second dipole of the A1900 to selectively disperse other reaction products relative to the desired ^{22}N and improve the final separation. Momentum slits are inserted at the dispersive image, and serve to tune the acceptance of the device. These slits were at 2.5% momentum acceptance for this experiment. The beam was delivered at an energy of 68 MeV/u and particle rate of 37/s with a purity of 32%. The primary contamination was from light ion production in the Al wedge, while the strongest heavy ion contaminants were ^{26}F at 6% and ^{20}C at 2.8%. All of these could be separated on an event by event basis offline.

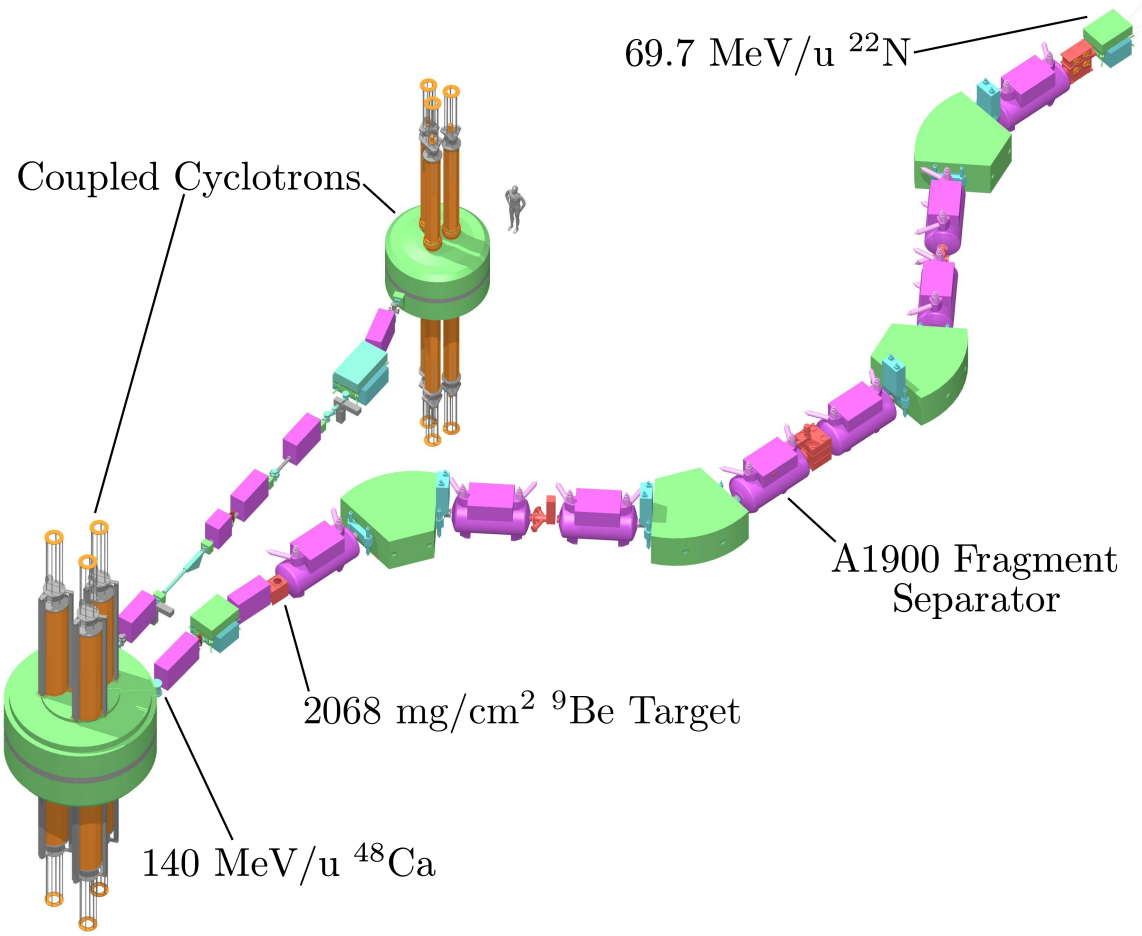

Figure 3.2: Beam production at the CCF.

3.3 Experimental Setup

A schematic of the experimental setup is shown in Figure 3.3. After exiting the A1900, the secondary beam passed through two position-sensitive cathode readout drift chambers (CRDCs). Downstream of the CRDCs, a quadrupole triplet magnet focused the beam onto the 481 mg/cm^2 ^{9}Be reaction target. A 0.254 mm plastic scintillator was placed immediately upstream of the reaction target to determine beam, charged fragment, and neutron time of flight. Neutron-unbound isotopes produced in the reaction target immediately decayed into charged fragments and one or more neutrons. A large-gap superconducting dipole magnet [41] bent the charged fragments away from the beam axis, and the neutrons were detected at forward angles by the Modular Neutron Array (MoNA) [42].

Downstream of the magnet, two more CRDCs separated by 1.82 m provided fragment trajectory information. An ionization chamber and thin plastic scintillator provided energy loss information for element separation, while a thick plastic scintillator provided a total kinetic energy measurement. Additionally, the thin scintillator provided time of flight of the fragments for isotope separation.

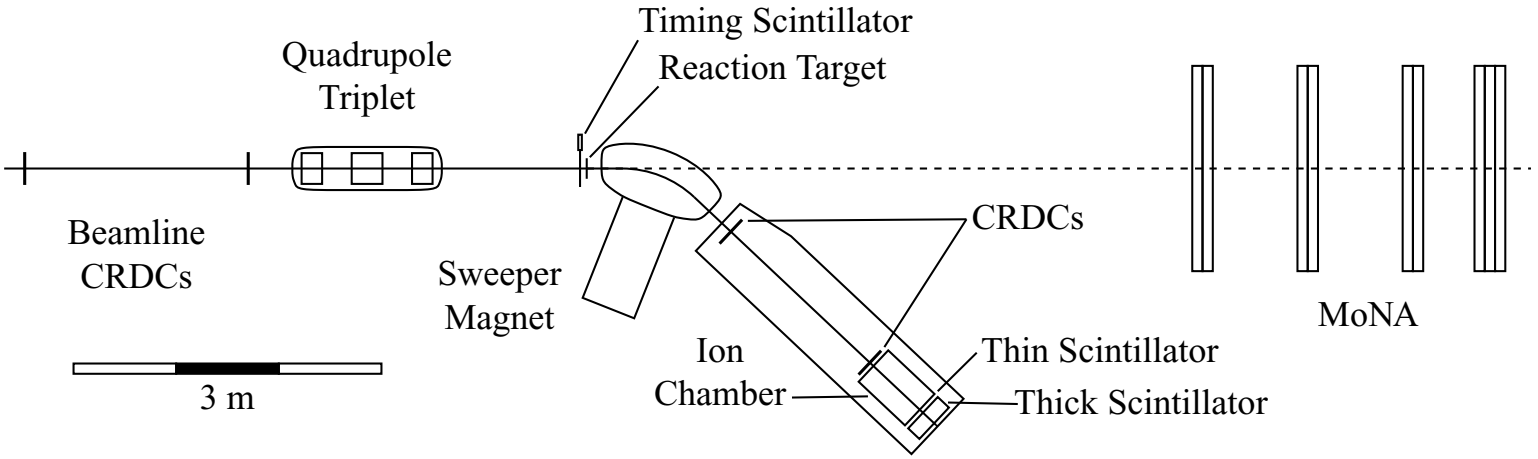

Figure 3.3: Experimental setup diagram.

3.3.1 Beamline Detectors

The incoming beam's trajectory is measured by a pair of CRDCs separated by 2.18 m whose operation is schematically shown in Figure 3.4. The active volume of each detector is filled with a mixture of 80% CF_4 and 20% C_4H_{10} at a pressure of 100 Torr, and incident charged particles ionize this gas. The freed electrons drift under a -150 V drift field toward an anode wire held at 1100 V which collects the charge. Drift time to the anode wire determines position in the non-dispersive plane. The charge collection on the anode in turn induces charge on a series of 64 aluminum pads placed near the anode wire with 2.54 mm pad pitch. A Frisch grid reduces position dependent response effects.

The distribution of charge on each pad can be used to determine the particle's dispersive position in pad space. The charge collected as a function of pad number can be fitted with a Gaussian function whose centroid corresponds to the position of the strike. There is a linear correlation between pad and physical position space, and the slope for that transformation is set by the pad pitch of 2.54 mm. The offset for the dispersive position transformation as well as nondispersive slope and offset are determined by calibration runs taken with a tungsten mask with holes in known locations placed in front of the detector.

A quadrupole triplet magnet was located downstream of the beamline CRDCs to focus the beam onto the 481 mg/cm^2 reaction target. The magnetic field of the triplet is mapped so a forward transformation can be applied to the CRDC trajectory information to construct target emittance parameters.

Three timing signals provide information about the beam time of flight. First, the cyclotron RF signals provide timing information which can be correlated with the primary beam particles impinging on the production target. A pair of scintillators at the A1900 and target chamber positions provide secondary beam time of flight over

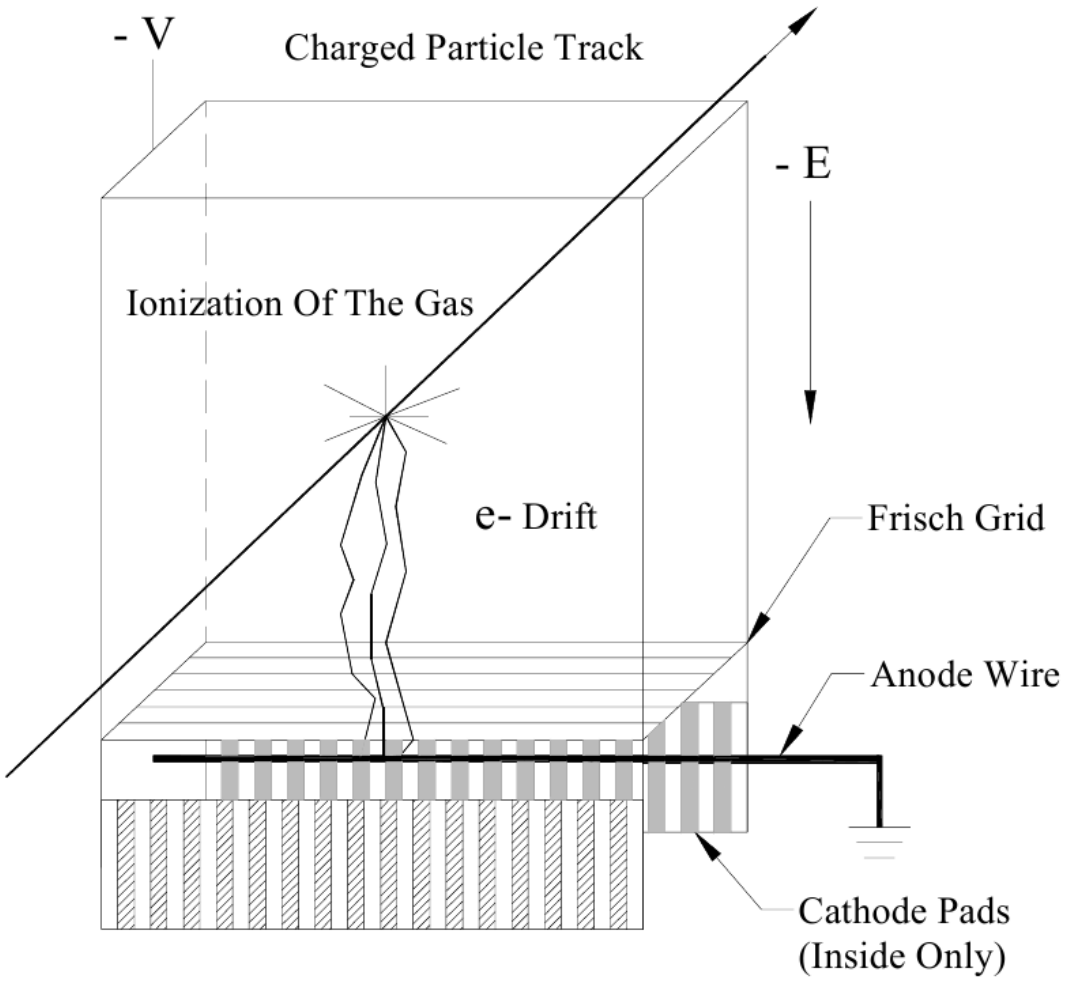

Figure 3.4: Schematic of CRDC operation from [43]. The incident charged particle ionizes the gas in the active volume, and the freed electrons move toward the anode wire under the drift field. A Frisch grid reduces position dependent charge collection effects, and the charge collection on the anode induces charge on the aluminum pads which determines the dispersive position of the interaction. The drift time of the electrons determines non-dispersive position.

a flight path of 11.52 m. Both scintillators are made of the plastic organic scintillator BC-404 [44] and are coupled to one PMT. The A1900 scintillator is 1008 μm thick, and the target chamber scintillator is 254 μm thick. When charged particles pass through an organic scintillator, energy loss through the material causes transitions to excited states of the organic molecule's electron structure, and the prompt fluorescence (τ = 1.8 ns) resulting from their subsequent de-excitation is converted to an electronic signal by the PMT.

3.3.2 Charged Fragment Detection

The large-gap superconducting dipole Sweeper magnet [41] has a bending radius of 1 m, a bend angle of 43°, and a maximum rigidity of 4 Tm. Its 14 cm vertical gap allows for neutron transmission to MoNA, with the consequence of some nonuniformities in the magnetic field which necessitated the careful mapping of its magnetic field properties. The magnetic field was set to a rigidity of 3.7581 Tm for maximum transmission of the ^{20}C reaction fragments during this experiment.

Another pair of CRDCs are located downstream of the sweeper magnet. The basic operation of CRDCs is explained in Section 3.3.1, but the specifications for these CRDCs is somewhat different. These detectors have an active area of 30 $\times$ 30 cm^2 with 128 aluminum pads of pad pitch 2.54 mm for dispersive position measurement, are separated by 1.82 m, and are operated at a pressure of 50 Torr of the same gas mixture as the beamline CRDCs. Additionally, the drift field was set to 500 V and the anode wire held at 1050 V.

Immediately downstream of the CRDCs is an ionization chamber which is used to measure energy loss for element separation (see Section 4.3). This detector has an active volume filled with P-10 gas (90% Ar, 10% CH_4) and is operated at a pressure of 300 torr. Like the CRDCs, a drift field is applied to ionization generated by incident charged particles, and the ionization is recorded by charge collection pads

after passing through a Frisch grid to reduce charge collection position dependence. In this case the drift field is 800 V, the anode is held at 50 V, and 16 collection pads with pad pitch 3.08 cm are arranged from front to back along the device. The active area is 40×40 cm with an interaction length of 53 cm [43]. The charge collected by each pad is summed to create the complete energy loss measurement.

Two more organic plastic scintillators are located immediately downstream of the ionization chamber - one 4.5 mm scintillator to measure the time of flight of reaction products for mass ID (see Section 4.3), and one 150 mm scintillator to stop the beam and provide a total residual energy measurement. These scintillators have a large active area (40×40 cm) and therefore have four PMTs each to collect scintillation light. Their operation is otherwise the same as described for the beam line scintillators in Section 3.3.1 as the scintillation material used is BC-404.

3.3.3 MoNA

MoNA consists of 144 $10 \times 10 \times 200$ cm^3 BC-408 [44] plastic scintillator bars with light guides and PMTs attached to each end. The modules were arranged in walls that were 16 modules tall and centered on the beam axis. Walls of 2 by 16 modules each were positioned with their front faces at 5.90 m, 6.93 m, and 7.95 m from the reaction target as shown in Figure 3.3. A block of three walls was placed at 8.65 m.

Neutrons are detected indirectly by the same method described for charged particles in Section 3.3.1. The uncharged neutrons elastically scatter from protons (hydrogen nuclei) in the hydrocarbon making up the plastic, causing the charged proton to recoil and deposit energy in the scintillation material. De-exciting molecular levels produce photons which travel to each end of a bar and are collected by a PMT and turned into an electric signal which can be recorded. Each PMT has two output signals. The anode signal is sent to a constant fraction discriminator (CFD) to determine the time of the pulse, which is in turn fed into a time to digital converter

(TDC) which measures the time of the signal by using the target scintillator as a common stop. Neutron time of flight was measured from the mean time of the two PMT signals of the detector module that detected a hit, while position across the bar was measured by the time difference between the signals. The dynode signal is sent to a charge to digital converter (QDC) and measures the energy deposition of neutron strikes.

3.3.4 Electronics and DAQ

Detailed descriptions of the electronics and data acquisition (DAQ) for the MoNA/Sweeper set-up can be found in [45, 46] so a brief overview will be included in this work. The Sweeper and MoNA electronics and DAQ are in principle independent and can be operated separately, but are coupled for the purpose of neutron coincidence experiments. Figure 3.5 schematically highlights the important aspects of the detector subsystems from a trigger logic / DAQ perspective.

The trigger logic was implemented by two logical levels of field programmable gate arrays (FPGAs). "Level 1" decides whether MoNA observed a neutron; this is determined by the logical OR of all MoNA CFD signals. "Level 2" makes the final decisions on whether to process the event. The target scintillator signal served as a common stop for the MoNA TDCs and allowed the neutron time of flight measurement. The master trigger was formed by the output of the CFD attached to the thin scintillator's upper left PMT, which indicated that a charged fragment entered the sweeper focal plane chamber. As soon as Level 2 received a trigger, it sent out a "veto" signal to stop all other electronics processing until a decision is made if the data was worth recording. Because the beam rate was low for this experiment, the only requirement for data to be recorded was the presence of the master trigger signal, so data was recorded to disk for every charged fragment event regardless of whether a neutron was in coincidence. A "Computer Go" signal was sent out to all electronics which

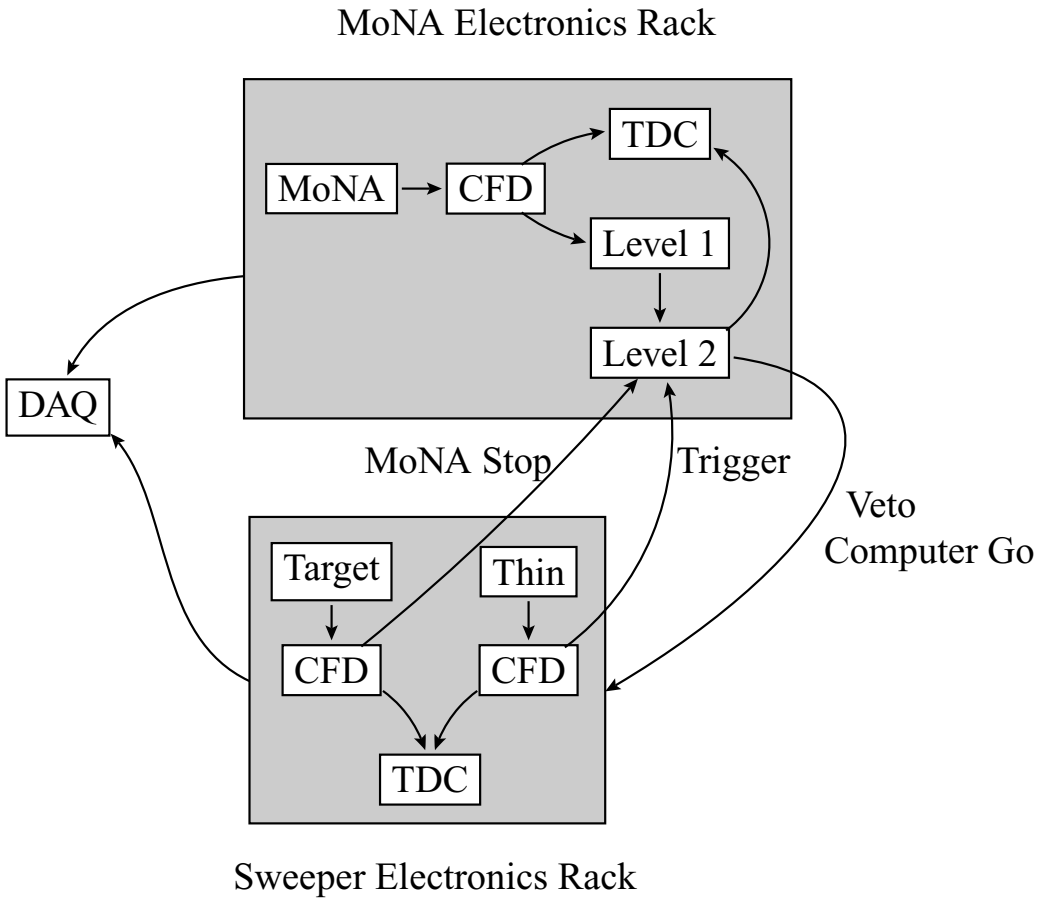

Figure 3.5: Trigger logic diagram.

allowed them to communicate with the DAQ software to record their information.

Chapter 4

Analysis

4.1 Overview

Online data analysis during the experiment was performed using SpecTcl [47], while offline analysis was performed post-experiment using a combination of ROOT [48], SciPy [49], and IPython [50]. Figures and final plots were created in PyX [51]. Calibration data were taken before or during the experiment for different detector systems and calibration parameters extracted in offline analysis. After the calibrations were complete, particle identification could be performed and the neutron-fragment decay reconstructed. Once reconstruction was complete, physics information was extracted by using a Monte Carlo simulation package to model the entire experimental response to differing physics input.

4.2 Calibrations

4.2.1 Timing Scintillators

All beam timing signals were calibrated using knowledge of the electronics modules processing each signal and beam properties. As discussed in Section 3.3, the timing

signals were processed by TDCs, which had a linear response and therefore were calibrated with slopes and offsets. The slopes were directly determined from the TDC range (400 ns) and number of channels (4096), leading to a slope of 0.0977 ns/channel. The raw timing signals included a 20 ns jitter resulting from FPGA processing, as the FPGA operated on a 50 MHz clock. To rectify this, all beam timing signals were converted to nanosecond scale by multiplying by the relevant slope (0.977 ns/ch for all detectors in this setup), and the signal from the upper left PMT of the thin scintillator was then subtracted from all other PMT signals.

As the set-up only measured relative times, some choice had to be made for T = 0 in order to define the offsets; for this analysis, T = 0 was chosen to be beam crossing through the target. To determine the timing offsets for each detector, a run with the target removed and beam tuned to travel through the center of all charged particle detectors was used. The magnetic rigidities of all magnets in the beam line then defined beam velocity at each point in the beam line and therefore the time of beam particles hitting each timing detector relative to the target. Unlike the other timing detectors, the thin scintillator had four PMTs contributing to its timing signal. Therefore, the individual PMT timing signals were calibrated for each event, and signals from those PMTs which fired were averaged to provide the final thin timing signal.

All beam line timing signals drifted over the course of the experiment and had to be shifted on an event by event basis to remove the drift effects. Figure 4.1 displays the centroids of the raw timing signals for each of the major timing detectors as a function of event number throughout the course of the experiment. The thin scintillator is not shown because it was the triggering detector and therefore showed no apparent drift. The drift structures observed were removed with a shift calculated event-by-event by interpolating over a running average created by averaging each detector's time signals in bins $1{\cdot}10^5$ events wide.

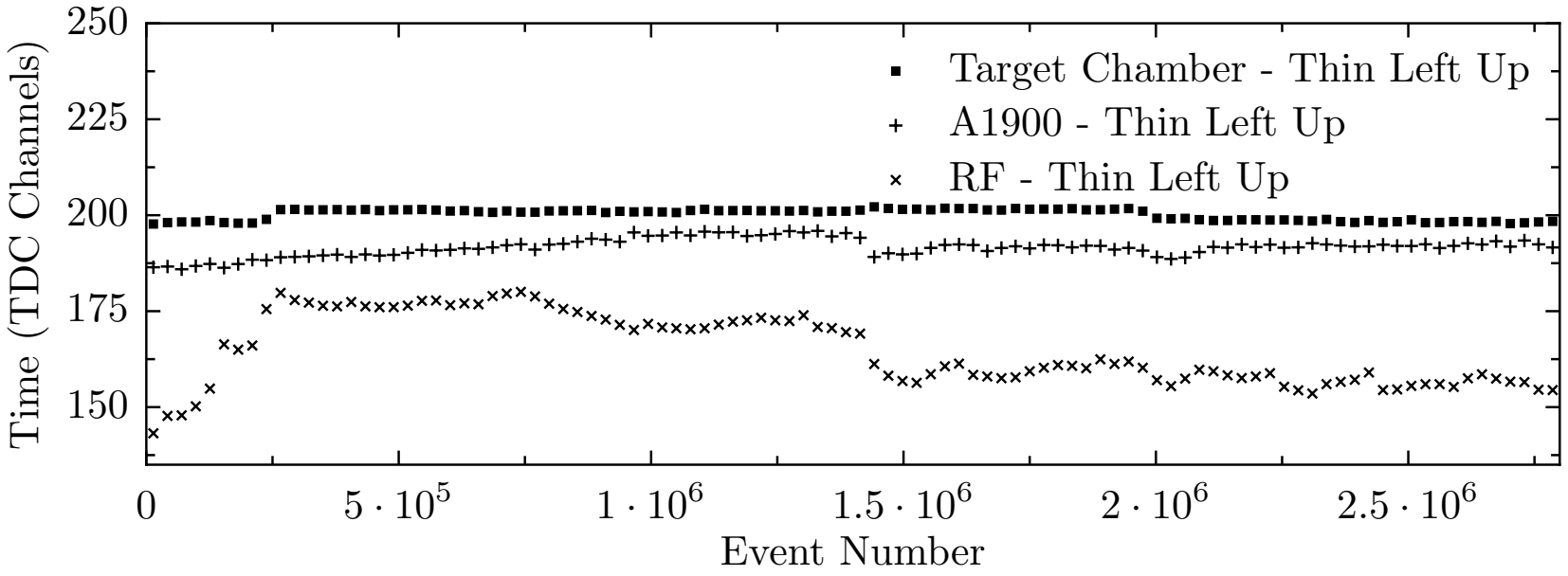

Figure 4.1: Timing drifts as a function of event number for all beam line timing signals.

4.2.1.1 RF Timing Shifts

The RF timing signal is downscaled by a factor of two, so it is possible to see multiple RF timing peaks in the raw RF time spectrum. As shown in Figure 4.2a, there were three RF peaks in the timing spectrum for this experiment, corresponding to two actual timing peaks. The middle peak corresponds to one actual RF signal peak, while the left and right correspond to another peak being split because the physical timing peak is located on the edge of the electronic time gate for accepting signals in the TDC. Lying on the edge of the timing window causes some sensitivity to the gate generation and signal propagation, so a simple shift of the cyclotron frequency (1./23.16 MHz = 43.18 ns) imperfectly matched and small additional shifts were needed to properly line up the peaks and match the line shape of the central peak. Figure 4.2b demonstrates the difference between the two techniques. The shifts corresponding to the cyclotron frequency (dotted line) do not line up with or match the line shape of the middle peak (solid), but agreement is achieved with an additional shift of 0.5 ns to the left peak and 0.7 ns to the right peak (dashed line).

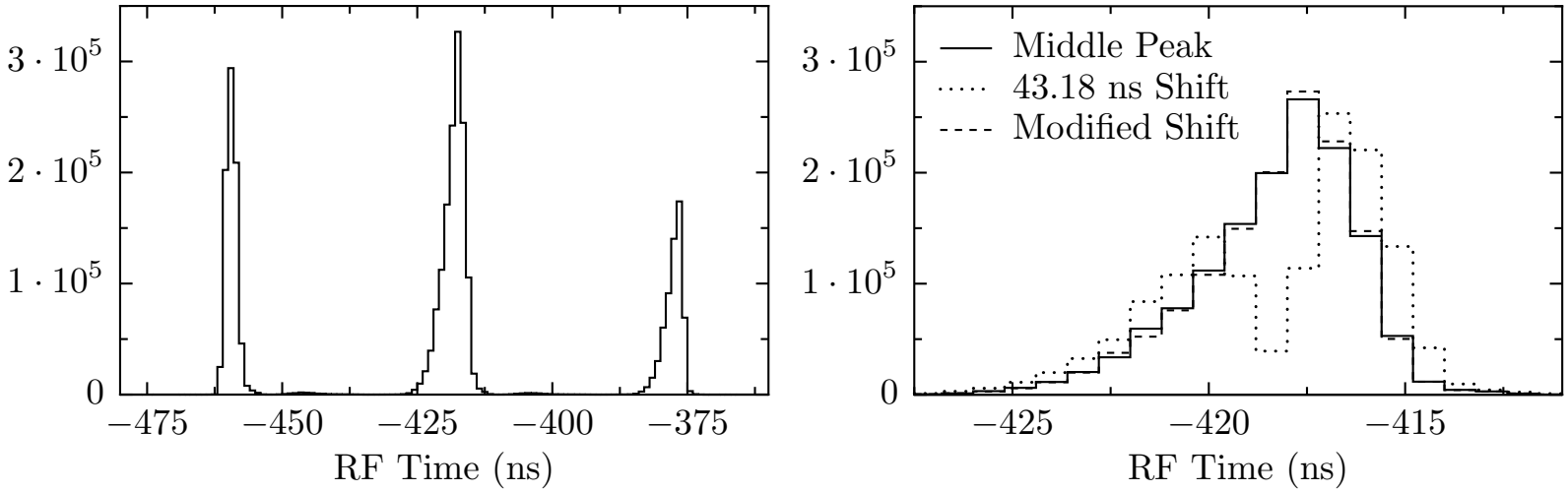

(a) RF Time before shifts

(b) RF Timing shifts

Figure 4.2: The downscaled RF timing signal showing up as three peaks in an uncorrected time spectrum (a). In (b), the 43.18 ns shift corresponding the cyclotron frequency does not match the middle RF peak, while adjusting the shift parameters slightly (see text) results in good agreement.

4.2.1.2 Virtual Target Scintillator Timing

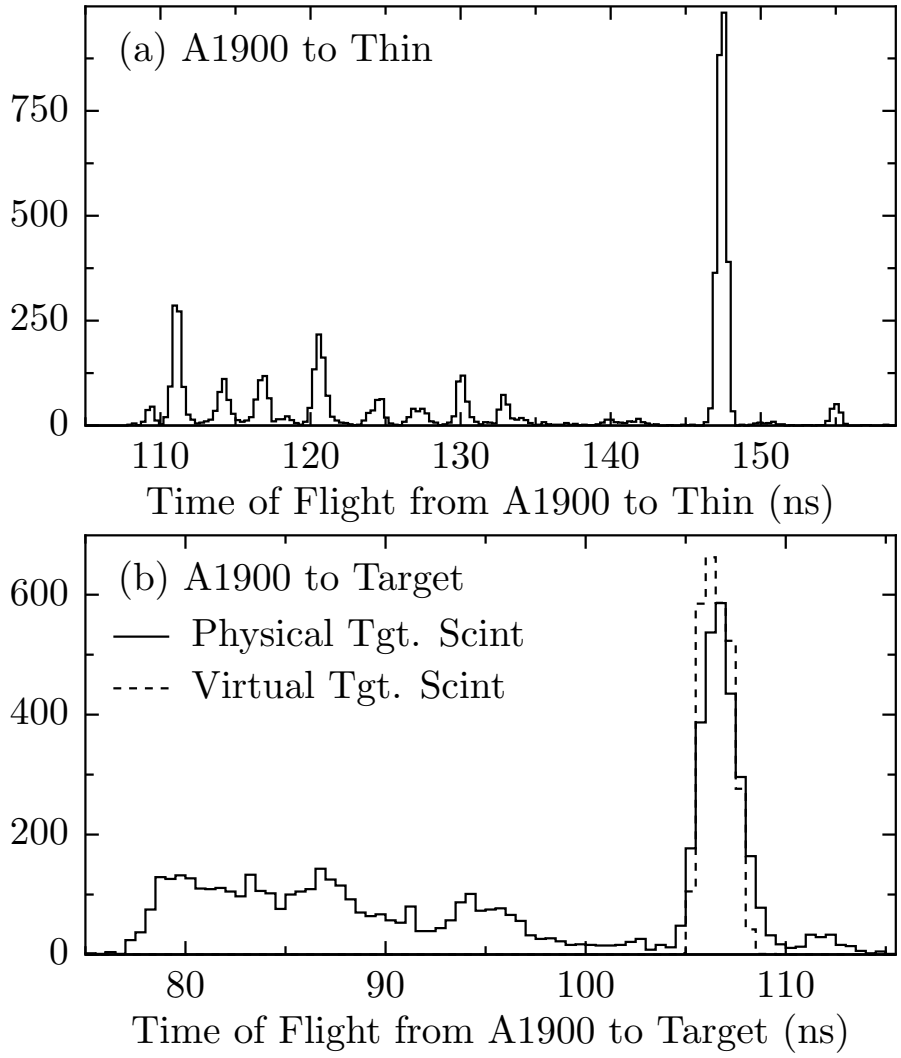

Figure 4.3: Resolution comparison between the target chamber and thin scintillators for a no-target run. The beam particle peaks in the spectrum utilizing the target chamber scintillator (right solid) is a factor of 2.5 wider than the corresponding peaks in the time spectrum utilizing the thin scintillator (left) despite the A1900 to thin flight path being longer. This widening is entirely due to resolution effects. The virtual target scintillator (right dashed) improves the resolution by ∼20%.

The target chamber timing scintillator had poor timing resolution during the experiment which critically degraded the quality of isotopic separation. Figure 4.3 demonstrates the degraded resolution by showing two time of flight spectra for a run where the target was removed, the momentum slits of the A1900 were reduced to

0.5%, and the beam was sent through the middle of all charged particle detectors. The left spectrum shows the resulting time of flight from the A1900 scintillator to the thin scintillator, while the right spectrum displays time of flight from the A1900 scintillator to the target chamber scintillator. Despite the A1900 to thin scintillator path length being longer, the A1900 to target chamber timing spectrum has significantly wider peaks corresponding to the various incoming beam particles - a factor of roughly 2.5. This widening is entirely due to the timing resolution of the target chamber scintillator during this experiment. Therefore, a virtual timing signal was constructed event by event from the timing signals of the RF and A1900 using knowledge of the beam properties and LISE++ calculations to account for the various locations where the beam lost energy. Figure 4.4 will serve as a notational reference for the following discussion, and shows what beam line elements come into play with the calculations that follow.

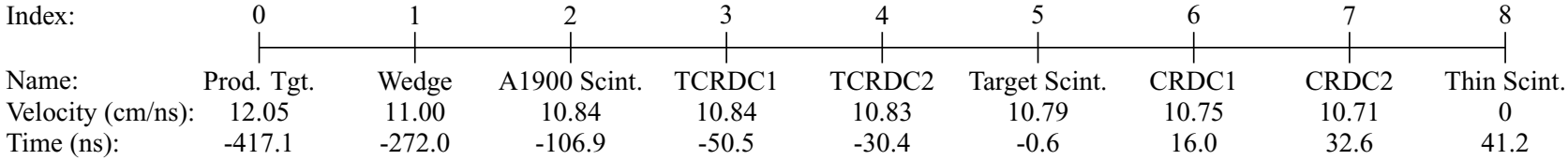

Figure 4.4: Notational reference for virtual target scintillator calculations

In order to properly calculate the timing signal of this virtual target scintillator, the relationship between velocities of the beam going into and exiting from each beam line element must be understood. Energy loss calculations were performed using LISE++ near the beam velocity for the achromatic wedge, the A1900 scintillator, and beamline CRDCs. Figure 4.5 demonstrates this relationship for every point where the beam lost energy before the target chamber. In all cases the relationship is linear, which simplifies the problem of calculating a beam velocity and propagating it to the target. For the discussion below, the following notation will be used: V_{ij} will represent the velocity between points i and j, T_{ij} will be the time of flight for beam particles between those points, D_{ij} will represent the distance between the beam line elements, m_i will represent the slope for the linear relationship between velocity before and after beam line element i, and b_i will represent the offset.

Constructing the virtual target chamber scintillator begins with the time of flight between the RF signal (assigned to correspond to the location of the primary beam production target) and A1900 scintillator. There is one issue however: the achromatic wedge mentioned in Section 3.2 is between the primary target and A1900 scintillator, and the unmeasured energy loss there can change the predicted beam velocity by approximately 8% and therefore introduce systematic errors in the calculation. Therefore, let us consider the problem where we have points 0, 1, and 2 (see Figure 4.4) and wish to calculate the velocity between 1 and 2. If we can calculate this quantity, the aforementioned velocity relationships can be used to propagate beam velocity and time of flight anywhere in the beam line. We are given T_{02} and $\mathrm{V}_{12} = \mathrm{m}_1\mathrm{V}_{01} + \mathrm{b}_1$. Then,

$$\begin{aligned} T_{02} = T_{01} + T_{12} &= \frac{D_{01}}{V_{01}} + \frac{D_{12}}{m_1 V_{01} + b_1} \\ T_{02} V_{01}(m_1 V_{01} + b_1) &= D_{01}(m_1 V_{01} + b_1) + D_{12} V_{01} \end{aligned}$$

Rearranging,

$$T_{02}m_1V_{01}^2 + (T_{01}b_1 - D_{12} - D_{01}m_1)V_{01} - D_{01}b_1 = 0$$

Therefore we must simply solve the quadratic formula for the correct root and exploit the linear velocity relationships:

$$\begin{aligned} V_{01} &= \frac{-b \pm \sqrt{b^2 - 4ac}}{2a} \\ a &= T_{02}m_1 \\ b &= T_{01}b_1 - D_{12} - D_{01}m_1 \\ c &= -D_{01}b_1 \\ V_{12} &= m_1V_{01} + b_1 \end{aligned}$$

The positive root has the correct behavior in the limit ΔV = 0 (no energy loss, or wedge thickness = 0) so that one is used. With this in hand, we have the velocity of the beam between the wedge and the A1900 scintillators. Because we know that, the correlations between velocities everywhere the beam loses energy, and the distances between all the beam elements we can predict what the time of flight between the A1900 and target chamber scintillators was without having to use the signal from the physical target chamber scintillator.

In Figure 4.3, the dashed line corresponds to the virtual target scintillator being used for time of flight calculations. The improvement in timing resolution was $\sim$20% over the physical scintillator, which made isotope separation possible. Velocity correlations must be calculated for each beam particle as each beam component has different energy loss characteristics, so only the ^{22}N beam component is shown.

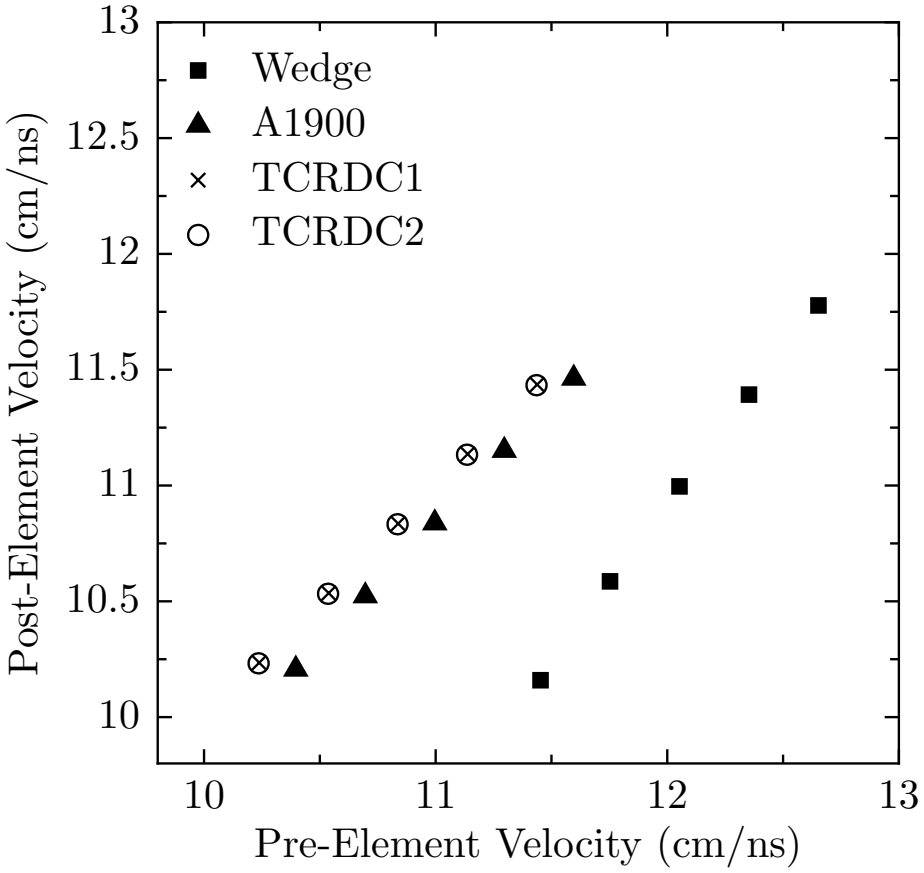

Figure 4.5: Velocity relationships calculated by LISE for all beam-line elements necessary for virtual target scintillator calculations. All trends are linear, and the CRDC trends lie very near each other because the energy loss is minimal through those detectors.

4.2.2 Tracking Detectors

Linear calibration parameters were used to calibrate all CRDCs, both in the beam line and focal plane chamber. The slope in the x direction was fixed by the pad pitch of 2.54 mm. The x offset, y slope, and y offset for a given detector were determined by sweeping beam across the face of the detector with a mask placed in front of it with holes drilled at known positions. An example calibration spectrum is shown in Figure 4.6. Well defined holes and slits are observed which can then be used to calculate the relevant calibration parameters.

The x position in each CRDC was determined by the distribution of charge on its

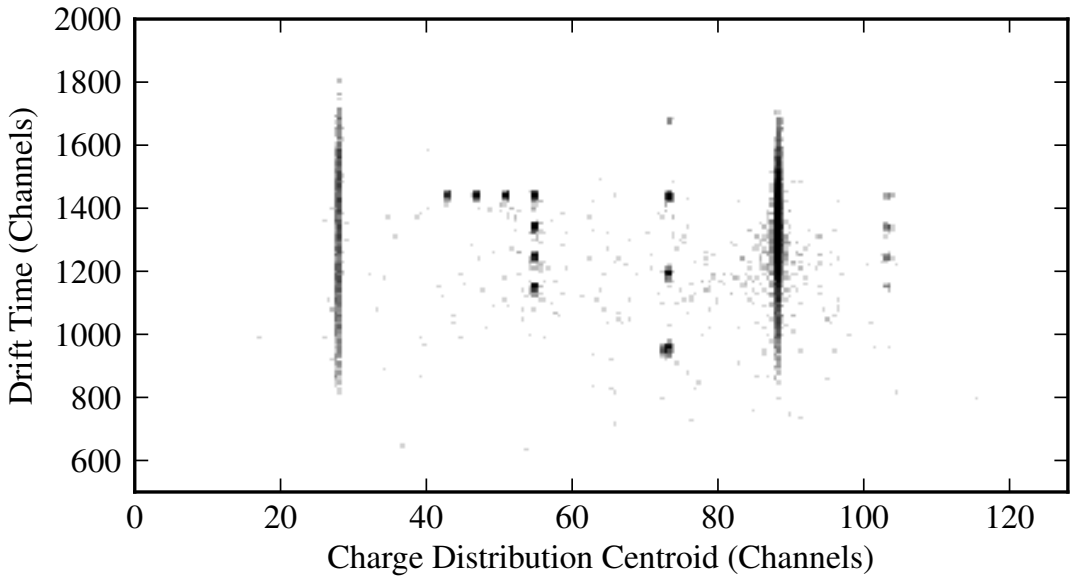

Figure 4.6: Sample mask hole position spectrum for CRDC2. The positions of the holes are known which enables the mapping of the raw detector information onto physical units.

pads. The pad data were read out every 25 ns, and the sum for each pad was then determined after a pedestal subtraction. Beam swept across the detector was used to gain match the pads relative to each other. A Gaussian fit to the charge distribution for each event was used to determine the x position of that particle.

A technical issue with the gas handling system for the focal plane CRDCs resulted in a discontinuity near event $2{\cdot}10^6$ demonstrated in Figure 4.7, which shows the centroids for the drift times of each CRDC as a function of event number throughout the experiment. The events near the discontinuity were discarded, as the rapidly changing detector properties resulted in unacceptable resolution losses when attemping to correct the detectors in that region. The drift time signal which generates the y position information for each CRDC was multiplicatively corrected on an event by event basis by interpolation over a histogram describing the time drift.

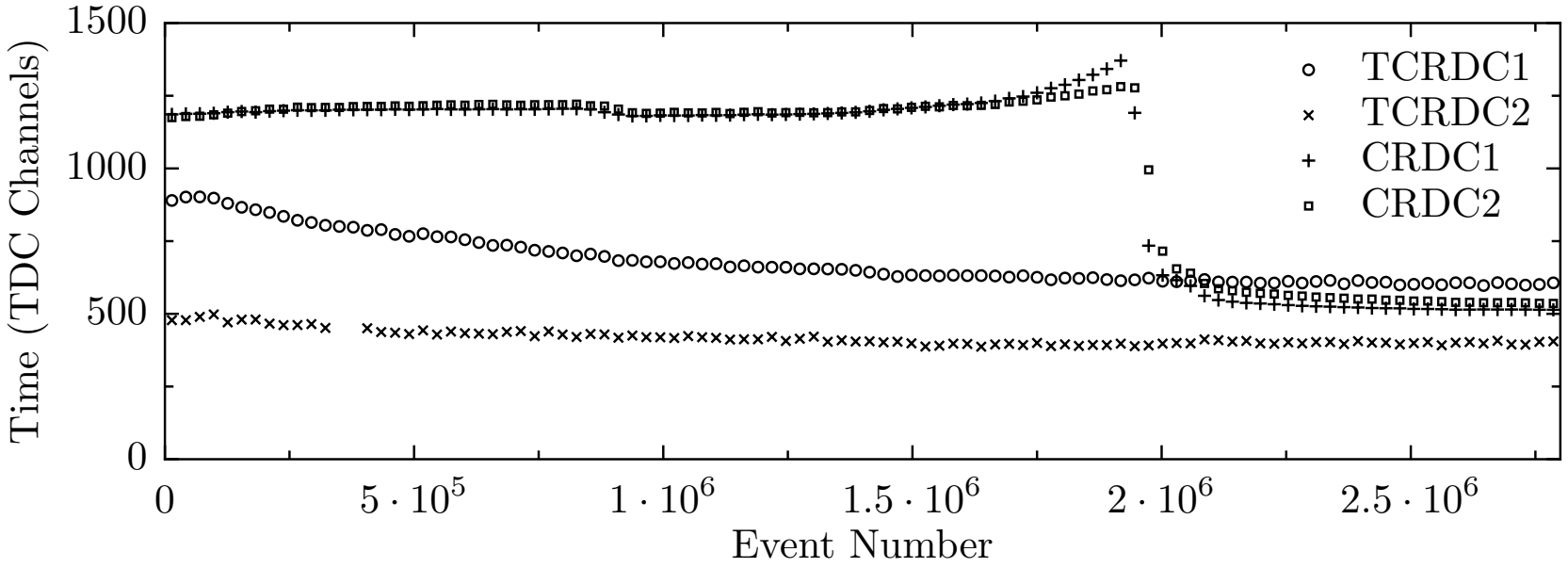

Figure 4.7: Drift time of ions in all CRDCs as a function of event number. The discontinuity near event $2{\cdot}10^6$ resulted from a technical issue changing the drift velocity of ions in the focal plane CRDCs.

The beam line tracking CRDCs suffered a less severe change in the drift time signal demonstrated in Figure 4.7, which was corrected with a multiplicative scaling factor in the same fashion as the focal plane CRDCs. Additionally, one of the TCRDCs had a technical issue with its charge collection such that the x position spectrum was distorted. The issue and its resolution are shown in Figure 4.8. On the left, the x position spectrum for a no-target run shows sharply peaked structures in place of a smooth distribution of beam particles. The shaded regions show where the detector was functioning reliably, albeit at a very low efficiency.

The event by event position information from that TCRDC was not salvageable at a useful efficiency, but removing the events in the spikes allowed a correlation between the x position spectra of both tcrdcs to be observed as shown in the right hand spectrum of Figure 4.8. This correlation was used to calculate the incoming beam trajectory in the x plane without using the affected TCRDC on an event by event basis. The trajectory of the beam particles could still be propagated forward to the target chamber for use with the reconstruction process later in the analysis. The y position information from the detector was not affected by this charge collection issue and could be utilized without further treatment.

4.2.3 dE, E Scintillators

The eight PMTs of the ΔE and total E scintillators were gain matched and corrected for position dependence due to light attenuation in the plastic. Each PMT was corrected for drift event by event. A no-target run with the beam centered in the focal plane was then used to gain match all PMTs with the beam travelling straight through the middle of the both scintillators. To produce the complete energy signal for each scintillator, the top and bottom PMTs were separately averaged and then the root mean square of the top and bottom pairs taken. X and y correction parameters for this signal were then obtained by sweeping beam across the face of the detectors and

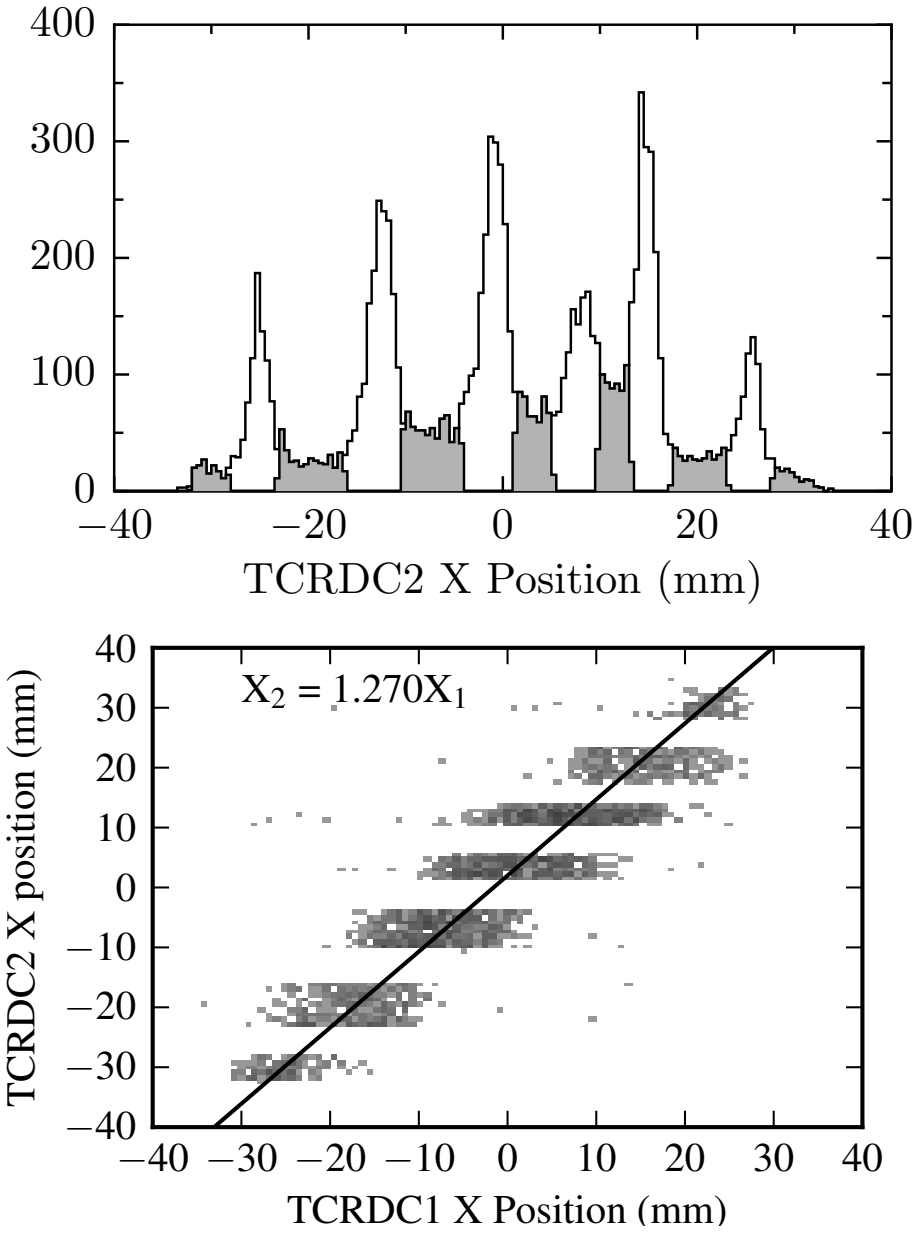

Figure 4.8: TCRDC2 charge collection issue (left) and the correlation between TCRDC positions used to replace the physical device's x position information.

using the CRDC information to obtain positions on each scintillator. The dominant position dependence was in the x direction, and this dependence is shown for both detectors in Figure 4.9. In both cases, the total energy signal for each scintillator was plotted as a function of x position at the detector, and a fit function generated to describe the position dependence. This function was then used to generate a multiplicative correction event by event, the results of which are also demonstrated in Figure 4.9.

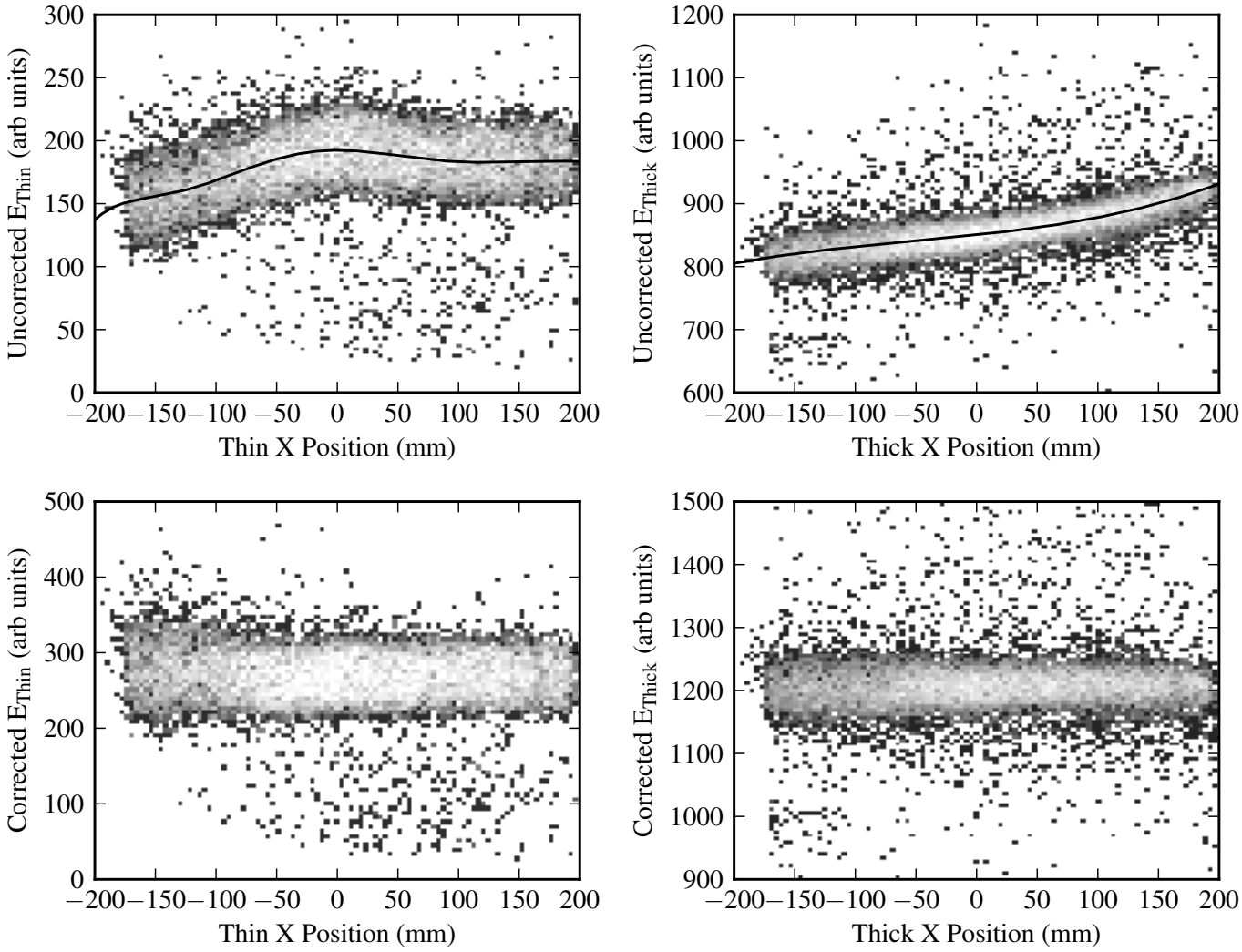

Figure 4.9: Thin (top left) and thick (top right) response as a function of x position and the corresponding correction curves. The bottom panels show the correction taking effect for both scintillators, which results in a flattened spectrum with position correlations removed.

4.2.4 Ionization Chamber

As discussed in Section 3.3.2, the ionization chamber has 16 charge collection pads whose signals are summed to obtain a ΔE measurement for element separation of reaction products. Therefore, the energy loss calibration of the ionization chamber proceeded by:

$$\Delta E = \sum_{i=0}^{15} q_i f_i(y,t) \tag{4.1}$$

$$f_i(y,t) = S/d_i(y,t) \tag{4.2}$$

Where q_i is the raw charge collection for an individual pad, $f_i(y,t)$ is a gain matching function, S is a scaling factor for setting the overall scale of the calibrated energy loss spectrum, and $d_i(y,t)$ is function characterizing the pad response as a function of position. The function $f_i(y,t)$ required special treatment because of the particular behaviour of this device during the experiment.

The primary cause of the more challenging calibration of this detector is demonstrated in Figure 4.10, which shows each charge collection pad's signal as a function of y position in the ion chamber. Pads 7 and 9-12 either collected no or very little charge, and therefore were not used in the calculation of the total ΔE measurement. All other pads show a severe position dependence which contributed to the poor resolution in Figure 4.12. In particular, the individual pad responses were sufficiently different to require independent treatment, so each pad was characterized separately and the pad signals combined after gain matching.

Finally, Figure 4.11 shows the response of one pad as a function of y position over the first 20 hours of the experiment. It is clear that the overall structure of the detector response does not change, but smaller substructures develop and evolve as a function of time. Because of the sharp rising and falling regions of the response

function, it was important to capture the time evolution of each pad's response with as fine a time binning as possible. Therefore, the data was divided into sections corresponding to timescales of roughly 45 minutes, each overlapping by half that value. Each pad's response was captured as a function of position for each section, and the sections chained together to form a surface characterizing the pad response as a function of position and time. Bilinear interpolation across this surface was then used to generate a multiplicative correction parameter, which could be combined with a global scaling parameter to create an event-by-event $f_i(y,t)$ to gain match each pad. Pads 0, 8, and 13 were beyond this technique's ability to recover and their inclusion in the total ion chamber signal spectrum degraded it, so $f_i(y,t)$ was set to 0 for those pads. Therefore, pads 1-6 and 14-15 were used to generate the final ΔE signal from the ion chamber. The results of this correction method are summarized in Figure 4.12, where the right panel demonstrates reasonable Z separation while the left does not.

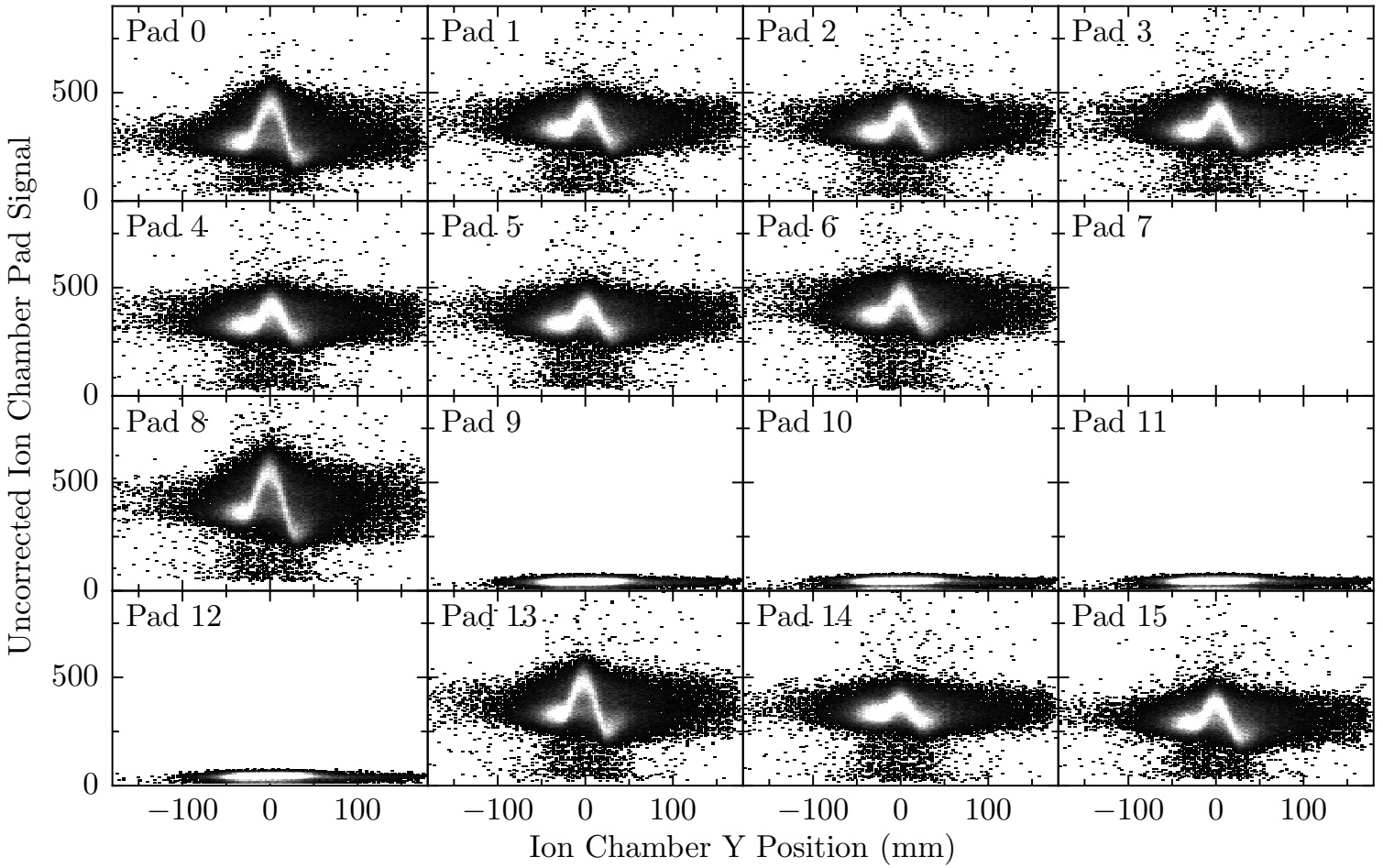

Figure 4.10: Sample ionization chamber pad signal vs. Y position for all pads.

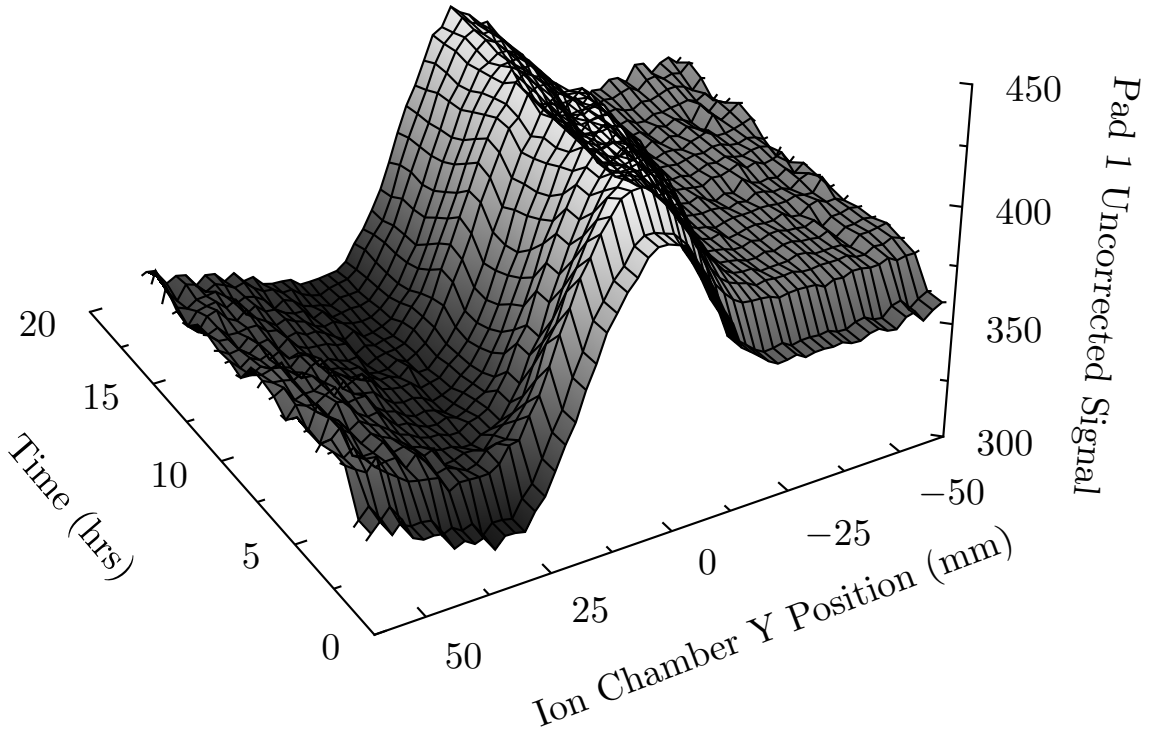

Figure 4.11: Position and time dependence of pad 1.

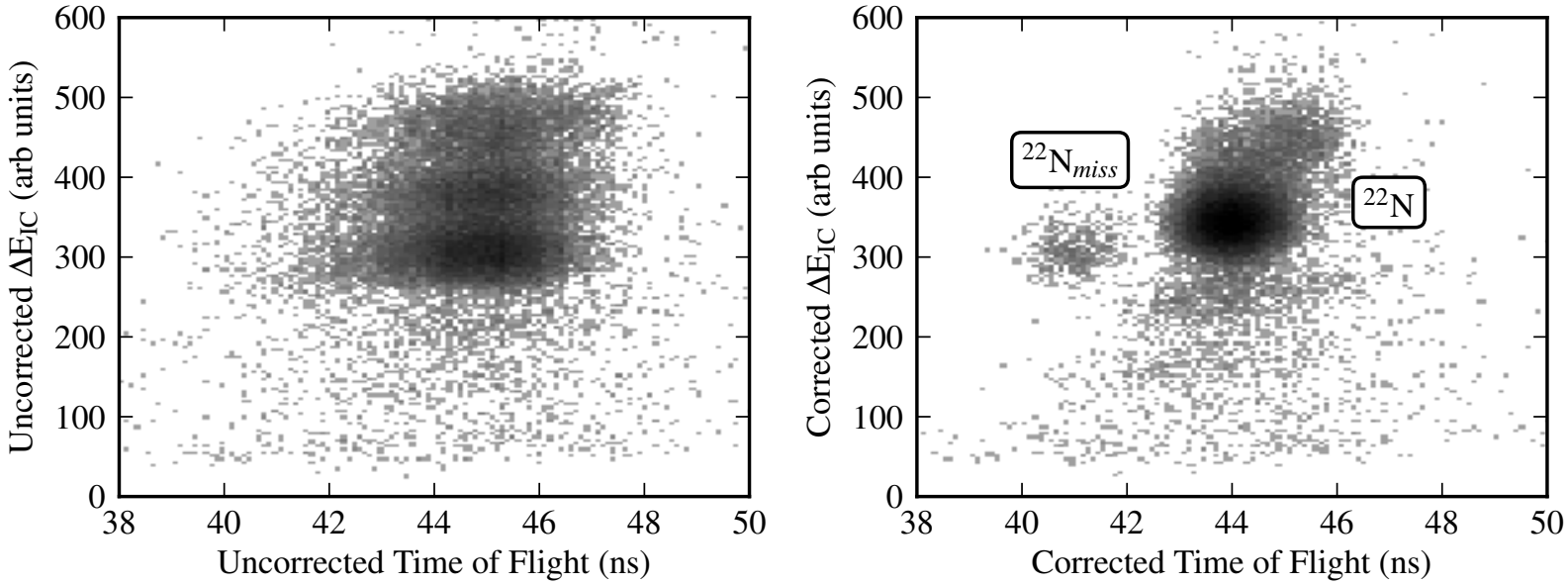

(a) Before Corrections

(b) After Corrections

Figure 4.12: Resolution comparison of uncorrected ion chamber and physical target scintillator (a) to corrected ion chamber and virtual target scintillator (b). Element separation is only possible in (b), and the improved timing resolution allows clean separation of ^{22}N missing the target.

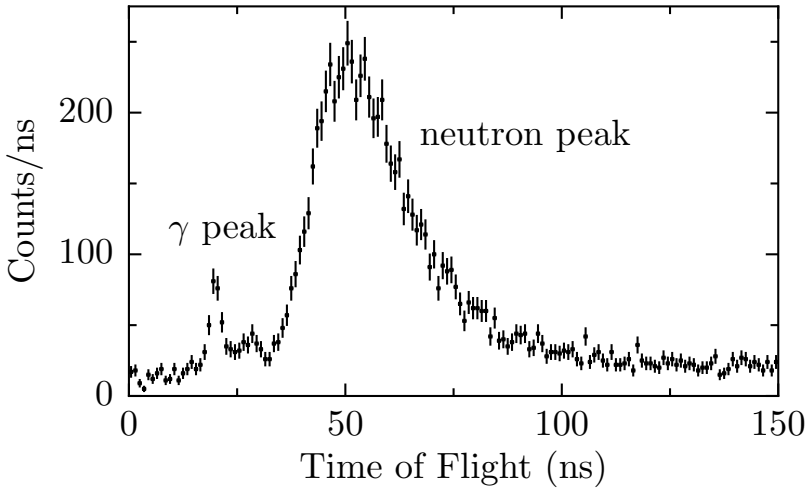

Figure 4.13: γ-ray timing.

4.2.5 MoNA

MoNA provided information about the neutron time of flight, trajectory, and deposited energy. Each PMT on each bar output an energy and time signal. Cosmic muons were used to gain match and perform a linear calibration of the energy signals for each PMT as muons deposit roughly 20.5 MeVee (MeV electron equivalent) in 10 cm of BC-408. The time signal from each PMT is ultimately sent into a TDC. The response of all MoNA TDCs was linear, so their signals were calibrated using slopes and offsets. The slopes were determined by pulsing the electronics with a timing calibrator, and offsets from cosmic muons travelling through multiple bars.

Time of flight was measured by the mean time of both PMT signals from a struck bar, and required a timing offset for MoNA relative to the target. A thick collimator was placed in the target chamber and γ-rays from the target striking the front face of MoNA were used to determine this offset. Figure 4.13 shows an example time of flight spectrum for the collimator run, where two peaks are noticeable. The sharply defined early peak results from prompt γ-rays and is used to determine the offset, while the slower, broad peak results from neutrons.

Finally, to ensure the veracity of the γ timing, CFD walk in the MoNA electronics had to be accounted for. It has been observed in several experiments that the mean timing signal from MoNA is systematically shifted for low energy deposition events. This effect is demonstrated in Figure 4.13, which shows the time of flight for a γ timing run as a function of energy deposition [52]. There is a clear correlation between time and energy deposition for the events which deposit a small amount of energy. This effect has been characterized and shown to be a consistent property of the MoNA electronics, so while this experiment did not accrue sufficient statistics in a γ timing run to independently characterize the walk, correction parameters could be taken from other experiments and used with confidence. The walk shift function took the form:

$$t_{corr} = t - \begin{cases} -2.56625e^{-0.62272/q} + 1.6531 & \text{for q} < 1.8 \\ \dfrac{2.861}{q} - 1.761 & \text{for q} > 1.8 \end{cases} \tag{4.3}$$

Here, t is the uncorrected time of flight, q is the energy deposited in MoNA in MeVee, and t_{corr} is the walk corrected time of flight. This completed the characterization and calibration of MoNA. With all calibrations performed, the momentum of neutrons arriving at MoNA could be fully described for use in the reconstruction process.

The y and z position of neutron hits in MoNA were determined by which bar was struck. The time difference between signals at each end of a bar was used to determine x-position, and was calibrated using cosmic muons.

4.3 Particle Identification

In order to reconstruct the reactions of interest for the ^{18,20}C + n systems, all fragments entering the sweeper had to be separated in Z and A. The incoming beam

was not pure, so the first step was the selection of events correlated to the ^{22}N incoming beam. Figure 4.14a demonstrates the constituents of the beam for this experiment by showing ΔE versus time of flight from the A1900 scintillator to the thin scintillator for a no-target run with beam running through the center of all charged particle detectors. The ^{22}N is labelled and corresponds to the single most intense particle spot. This component comprised 32% of the total beam, and arrived at the target with a rate of 37/s. The remaining fraction of the beam was dominated by light ions created in the achromatic wedge at the central point of the A1900 which populate the lower left section of the figure. The nearest heavy ion contaminant to the beam of interest was ^{20}C, which comprised roughly 2.8% of the total beam and could be separated in a time of flight spectrum. Beam selection for the production runs is shown in Figure 4.14b, where ΔE in the target chamber scintillator is plotted versus the time of flight from the A1900 scintillator to the target chamber scintillator. The primary separation is in time of flight, and ΔE is used to reduce contamination from lighter ions. Once again the ^{22}N is labelled and corresponds to the single brightest particle spot in the spectrum. The sharp cut structure on the high end of ΔE corresponds to the signal coming from the PMT on the target scintillator saturating its QDC for some events, which did not affect the timing or the separation for lighter ions.

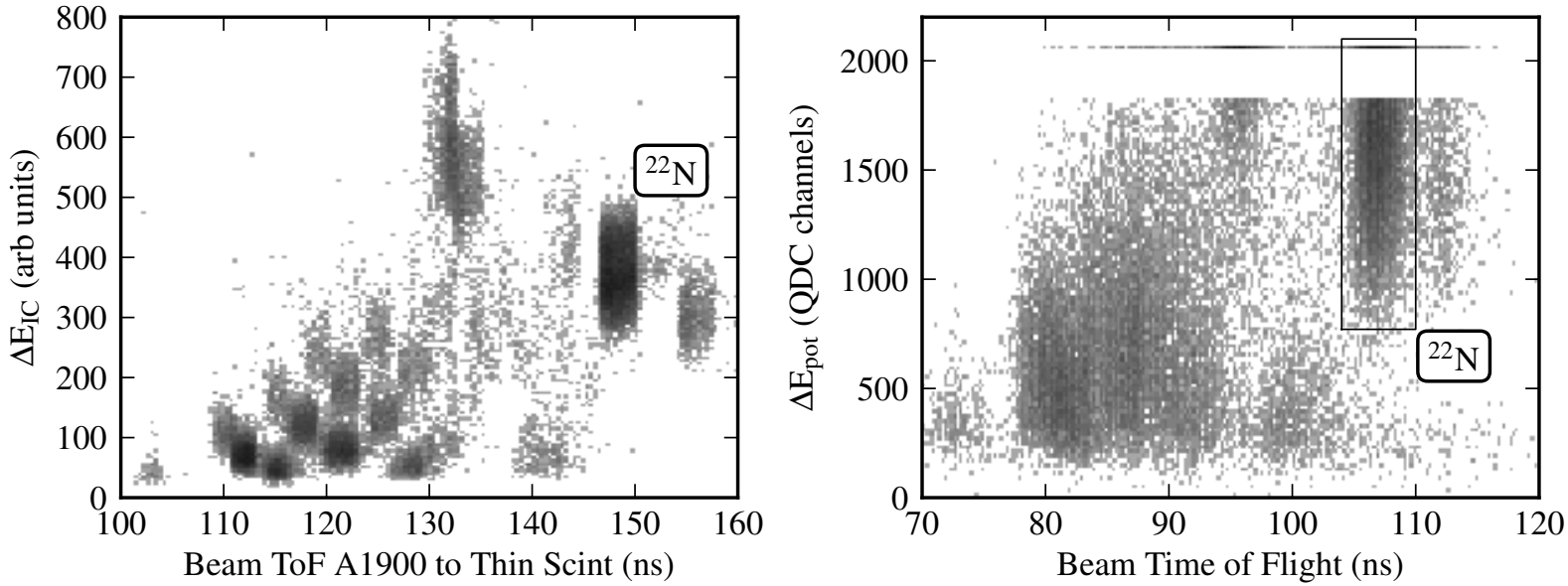

(a) Beam Profile.

(b) Beam ID Spectrum.

Figure 4.14: Beam profile and beam ID spectra.

The next step is Z separation of the reaction fragments. A simplification of the Bethe-Bloch formula results in the relation $\Delta E \propto \frac{Z^2}{v^2}$, which suggests that Z separation is best achieved through an energy loss measurement with its Z^2 dependence. Energy loss is correlated with the square of the particle's velocity, which further suggests that two dimensional separation of energy loss versus a parameter correlated to velocity would be optimal. The experimental setup has two independent measurements correlated with velocity - a time of flight and a total kinetic energy measurement in the thick scintillator. Both of these are plotted against the energy loss in the ionization chamber as shown in Figure 4.15. In both cases the different elements appear as slanted regions through the parameter space, indicative of the correlations mentioned above. The ^{22}N secondary beam appears as the most intense region for both spectra, and results from unreacted secondary beam reaching the focal plane detectors. This can be used as a reference, and defines the Z=6 reaction fragments of interest to be the locus of points just below the beam spot as indicated on both spectra. Gates on both spectra were applied to reduce contamination levels, and a neutron coincidence gate used to further reduce the amount of unreacted beam entering the reaction gate.

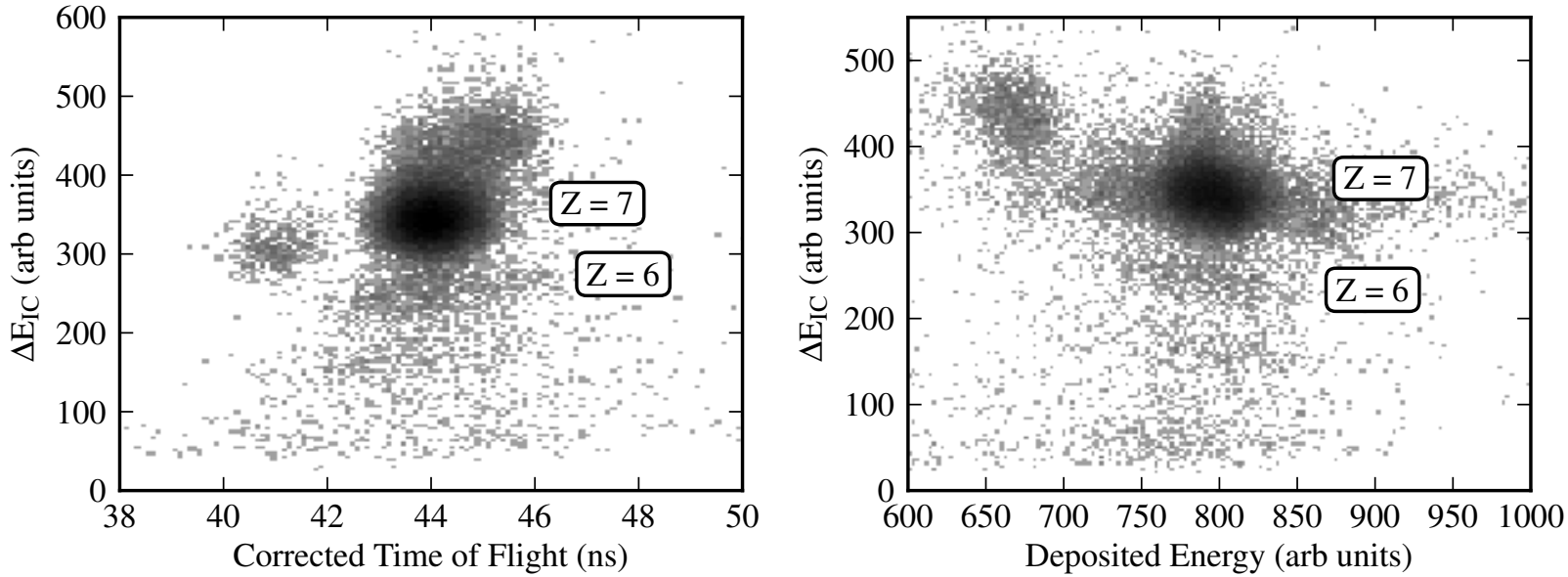

(a) Z ID from ΔE vs. Time of Flight.

(b) Z ID from ΔE vs. E.

Figure 4.15: Element separation by two different methods - ΔE vs. Time of Flight and ΔE vs. E. Both methods are combined to reduce contamination from unreacted beam.

Isotope separation for the reaction fragments was achieved using the time of flight information provided by the virtual target scintillator combined with the post-target trajectory information. Figure 4.16a illustrates simulated particle tracks corresponding to three different isotopes of the same element travelling through the sweeper magnet. The different isotopes have different magnetic rigidity, which causes them to bend differently in a dipole field and therefore travel different trajectories, which in turn makes separation possible. Complications arise from spreads angle and momentum distribution, which smear out the individual isotopic signatures through the magnet. The definition of magnetic rigidity serves to illustrate this:

$$B\rho = \frac{mv}{q} \tag{4.4}$$

$$t = A\left(\frac{Du}{B\rho q}\right) \tag{4.5}$$

The time of flight t for each isotope is related to its track length D and magnetic rigidity $B\rho$, and these are affected by the emittance of the incoming beam, straggling through the target, reaction dynamics and subsequent neutron evaporation, and the nonuniform nature of the sweeper's magnetic field. Therefore, within each isotope D and $B\rho$ have a width which smears out the time of flight. These effects can be correlated with the reaction fragment's emittance in the focal plane, and in a traditional spectrometer such as the S800 this appears as correlations with the focal plane angle. The right panel of Figure 4.16 demonstrates the application of this method to our setup, showing a plot of x (dispersive) angle versus time of flight. No hint of separation can be observed, which can be attributed to the properties of the sweeper magnet. Position and angle measured at the focal plane are highly correlated; consequently, a naive 2D separation is impossible without reducing the correlation space by at least one parameter. A systematic mechanism to visualize and account for these strong correlations has been developed (see [52] for the original

work).

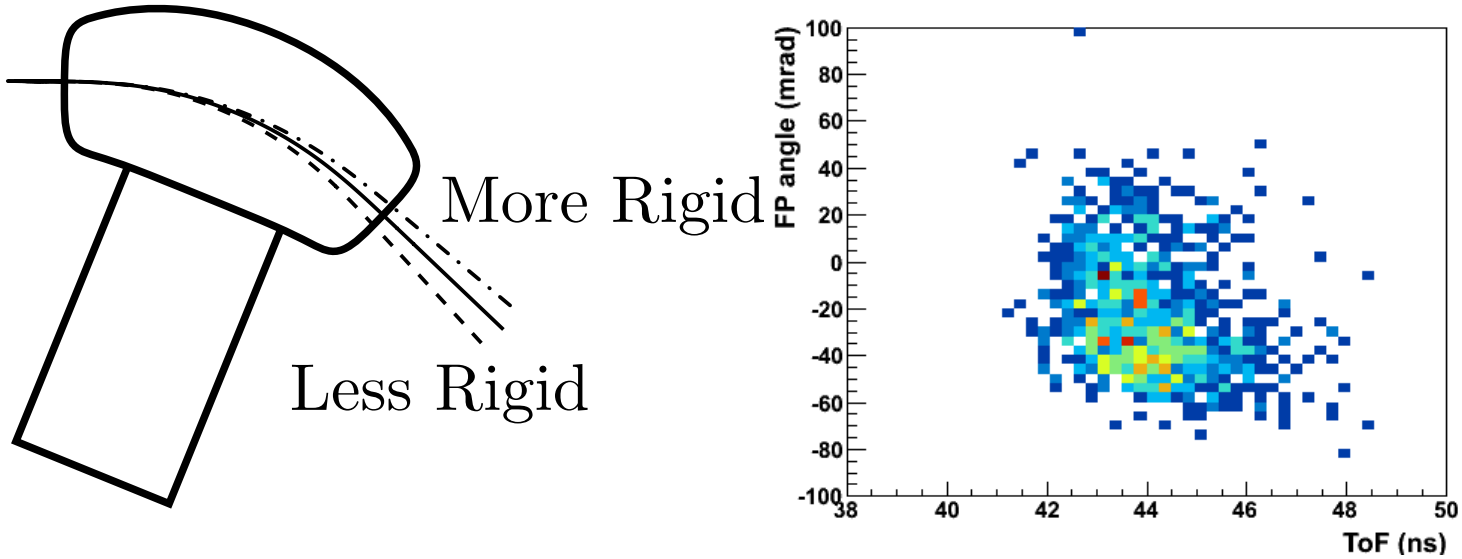

(a) Particle tracks.

(b) Traditional PID.

Figure 4.16: Particle tracks for different carbon isotopes through the sweeper magnet (a), and a traditional particle ID attempt from plotting dispersive angle vs. time of flight (b). Correlations between angle, position, and time of flight preclude such a treatment (see text).

The strongest correlations that need to be accounted for are those between time, measured position, and measured angle in the focal plane. An example visualization of the correlations is shown in Figure **??**, where bands can be seen in a 3D scatter plot of those parameters [53]. In this experiment, the low beam rate and previously discussed technical reasons result in Figure 4.18, in which the correlation curves can still be seen albeit more faintly due to the smaller number of counts in the spectrum. Reducing this separation to two parameters proceeds by determining the correlations between the angle and position parameters, which is accomplished by first projecting the 3D scatter plot into the angle/position plane.

This is accomplished by dividing the angle/position plane into a number of small regions, and calculating the average time of particles entering those regions. This calculation results in the plot shown in Figure 4.19, where the angle/position plane make up the y and x axes and the average time is represented by color. The correlation between the angle and position in the focal plane is seen as lines of constant color running through the image. A curve can be drawn which then represents this correlation, and a reduced parameter created which accounts for the correlations between angle and position:

$$e = \theta_x - f(x) \tag{4.6}$$

This emittance parameter e can be plotted against time of flight to obtain the first separation. Figure 4.20a shows a high statistics example to illustrate the technique, while 4.20b shows how it looked for this experiment. Bands can be seen forming along a diagonal line through this parameter space. To improve the separation, these 2D correlations can be further reduced to a single parameter (corrected time of flight) and that parameter plotted against all other charged particle parameters to remove correlations. To make this reduction, a simple linear projection of the form

$$t_{cor} = t - e/s \tag{4.7}$$

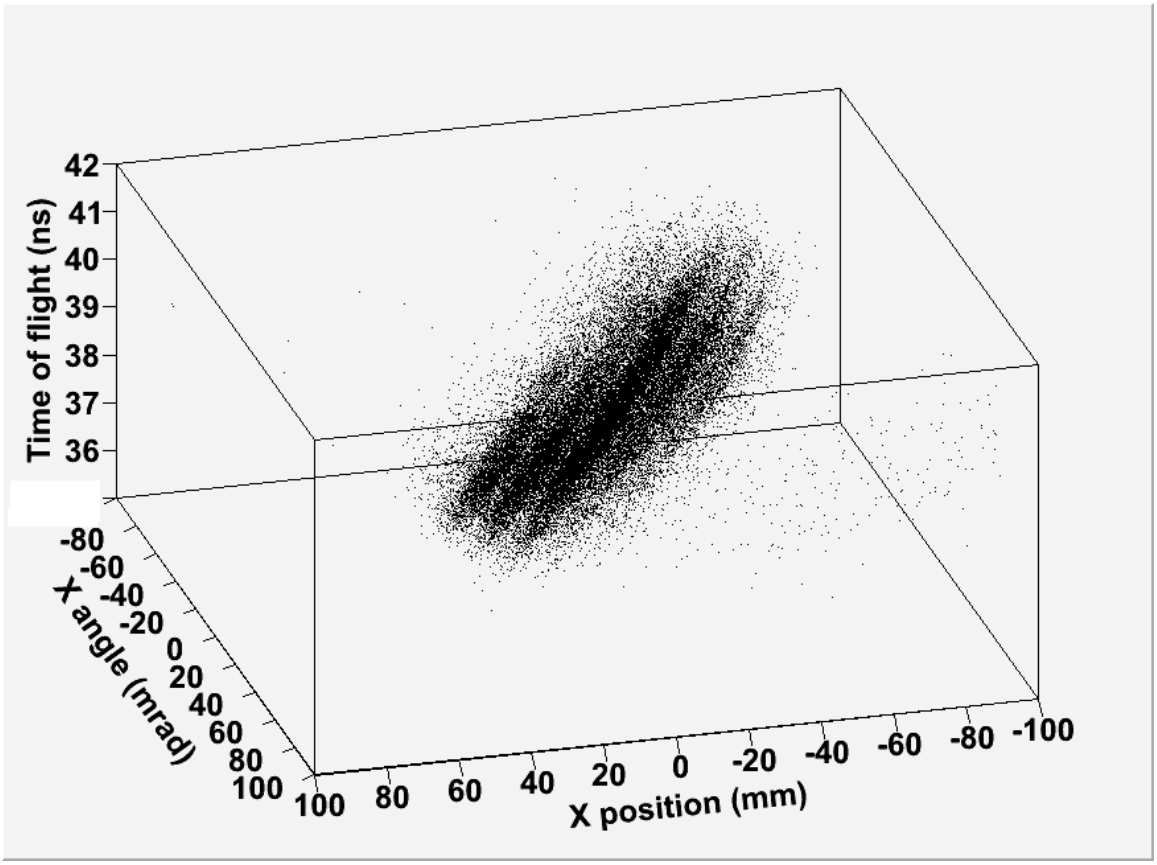

Figure 4.17: Example Correlations

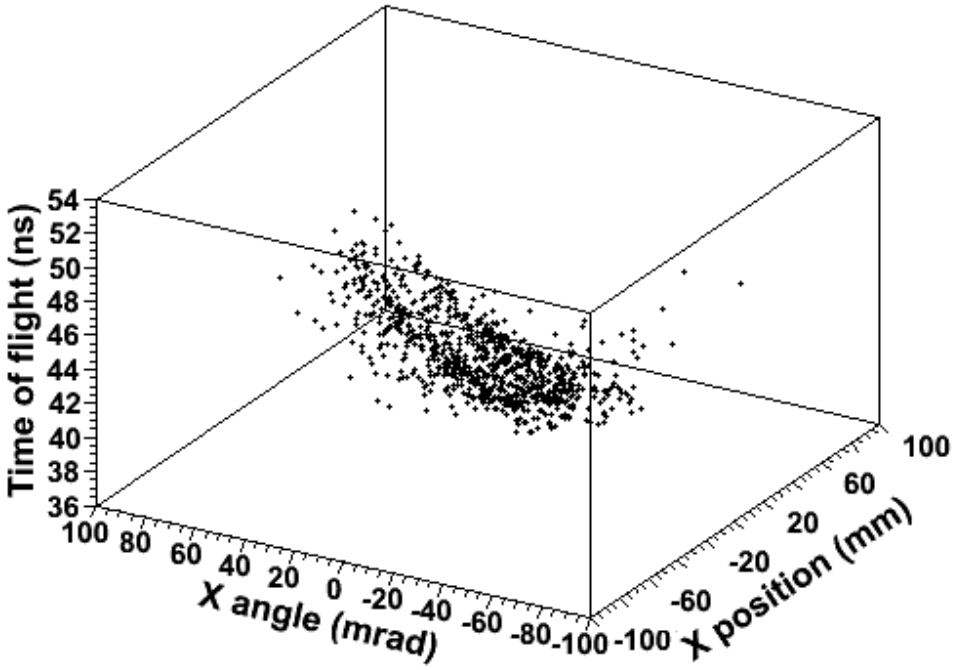

Figure 4.18: Correlations

is performed, where s is the slope the bands follow in Figure 4.20. With this in place and other correlations with nondispersive position and angle removed, the corrected time of flight can be used for isotope identification. Figure 4.21a demonstrates a high statistics example result from this technique, while 4.21b demonstrates particle separation for the Z=6 reaction fragments of this experiment. The separation is more limited in this experiment than the example, but there are clear indications of three isotopes in the spectrum. These have been identified as $^{18\text{-}20}$C, with the unresolved momentum tail of ^{17}C seen as the tail on the left side of 4.21b. Because of the somewhat limited separation, conservative isotope gates were placed on the corrected time of flight and are represented by the grey regions. Both ^{18}C and ^{20}C fragments were resolved at the cost of some 20% of their counts and a cross contamination 2%. ^{19}C was contaminated from both ^{18,20}C fragments and therefore its contamination level was 16%. As a result, detailed analysis was performed on ^{18,20}C fragments but

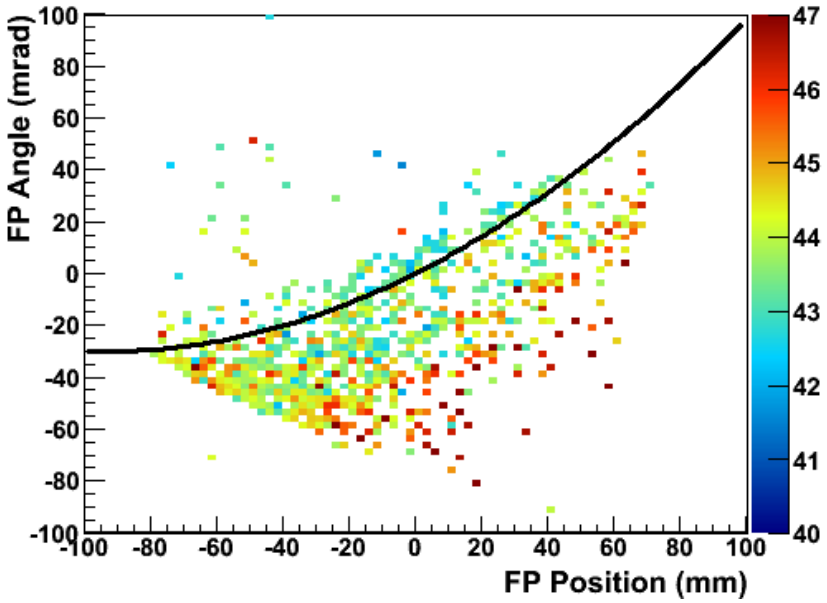

Figure 4.19: Projection of correlations into 2D.

not ^{19}C.

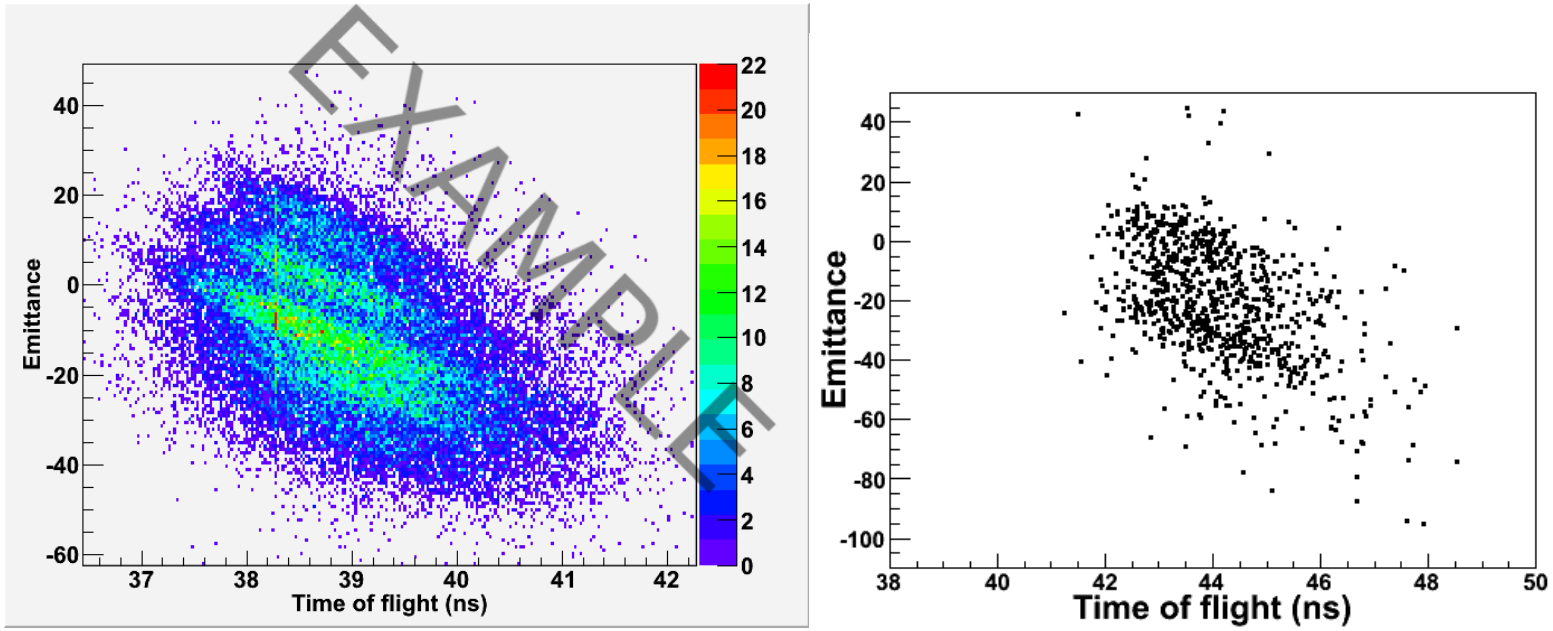

(a) Example Reduction.

(b) Reduction.

Figure 4.20: "Emittance" parameter vs. time of flight.

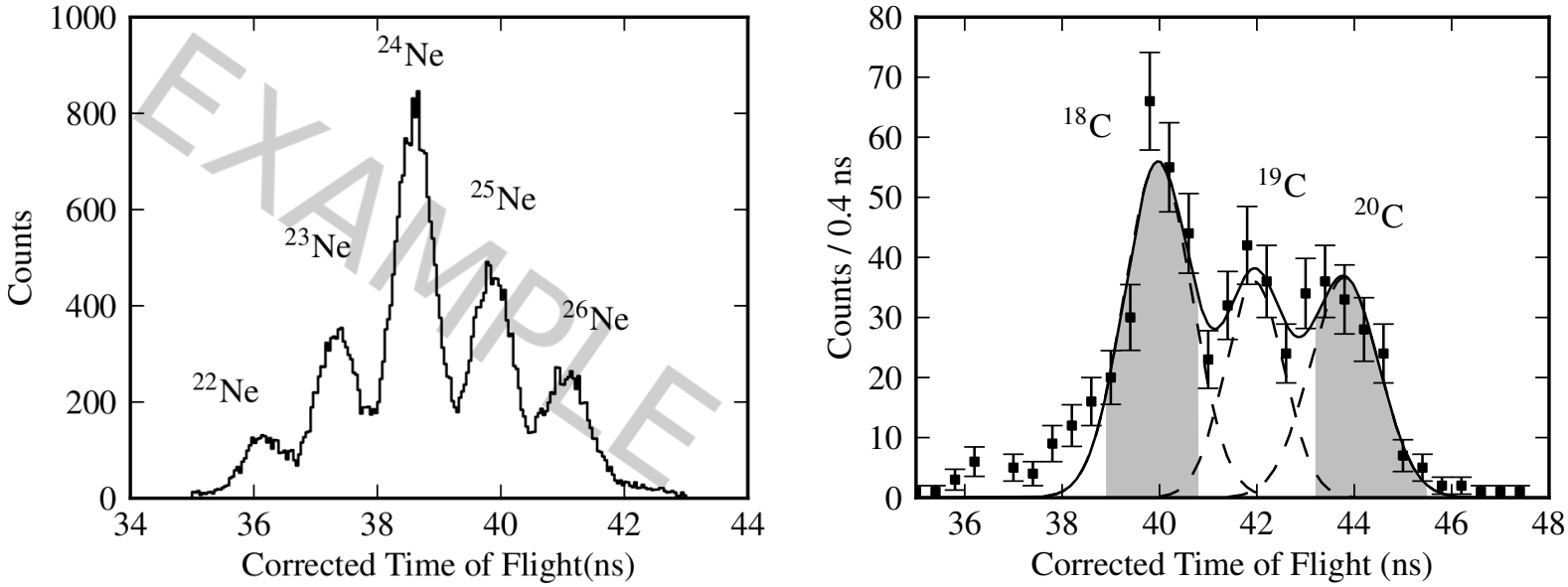

(a) Example PID.

(b) PID.

Figure 4.21: Final corrected time of flight with grey regions indicating particle gates.

4.4 Reconstruction

As discussed in Section 3.1, calculating the decay energy of neutron unbound states by the invariant mass method requires the measurement of the neutron and charged fragment momentum four-vectors. Constructing these vectors proceeds by an indirect method utilizing knowledge of the magnetic field of the sweeper for the charged fragment, and by ray-tracing for the neutron.

4.4.1 Fragment Momentum Four-Vector

The post-magnet trajectory of the fragment is directly measured by the experimental setup, and the quantities needed for reconstructing a decay energy are those of the fragment at the target (Section 3.1). Therefore, the post-magnet trajectory information must be tracked back to the target by some means. Because these two frames are related by ion optics through a magnetic field, this is a tractable problem if the magnetic field is known. The magnetic field of the sweeper was measured by seven Hall probes evenly spaced and mounted vertically on a movable cart which was stepped through the track of the sweeper at regular intervals (more details given in [45]).

The ion-optics code COSY INFINITY [54] generated a matrix M which related the post-magnet trajectory information to a target momentum 4-vector:

$$\begin{bmatrix} x^{\text{crdc1}} \\ \theta_x^{\text{crdc1}} \\ y^{\text{crdc1}} \\ \theta_y^{\text{crdc1}} \\ L \end{bmatrix} = M \begin{bmatrix} x^{\text{target}} \\ \theta_x^{\text{target}} \\ y^{\text{target}} \\ \theta_y^{\text{target}} \\ E^{\text{target}} \end{bmatrix} \tag{4.8}$$

To define a momentum 4-vector, the target quantities needed from Equation 4.8 are E^{target}, θ_x^{target}, and θ_y^{target} and as mentioned above, none of these is directly

measured. Post-sweeper tracking provides x^{crdc1}, θ_x^{crdc1}, y^{crdc1}, and θ_y^{crdc1}, while the forward tracking from the beam line CRDCs provides x^{target} and y^{target} (the angle information is destroyed by the reaction in the target). Direct matrix transformations to rearrange for the desired quantities in terms of the measured ones is impossible because the track length L is unknown. An approach commonly used by COSY to overcome this obstacle is to assume $x^{\text{target}} = 0$, However, this assumption is only valid for systems where the beam spot is small, and breaks down for the larger beam distributions encountered in this setup (order of 2 cm).

It is however possible to perform a partial inversion of M to obtain the needed transformation matrix. In particular, matrix operations were performed to exchange pairs of terms on each side of Equation 4.8 (see [55] for details). A condition for the successful swapping of terms is that they have a high degree of correlation with each other. The resulting expression is:

$$\begin{bmatrix} \theta_x^{\text{target}} \\ y^{\text{target}} \\ \theta_y^{\text{target}} \\ L \\ E^{\text{target}} \end{bmatrix} = M_p \begin{bmatrix} x^{\text{crdc1}} \\ \theta_x^{\text{crdc1}} \\ y^{\text{crdc1}} \\ \theta_y^{\text{crdc1}} \\ x^{\text{target}} \end{bmatrix} \tag{4.9}$$

where now quantities measured by the setup are on the right side and can be related to quantities we are interested in on the left though a transformation matrix which can be calculated with COSY.

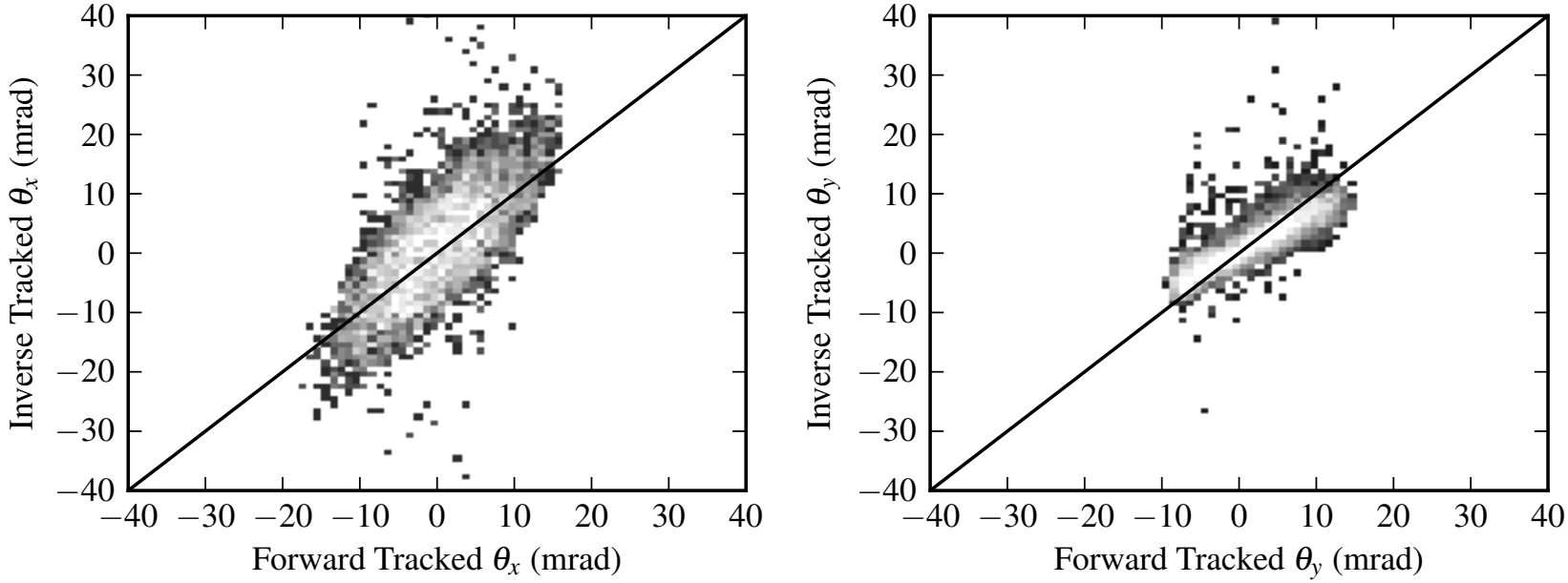

Figure 4.22: Consistency check for magnetic field map transformations showing reasonable agreement between the forward and inverse tracking processes.

Performing this reconstruction process required transformations between and alignment of three different coordinate systems (pre-quadrupole, target chamber, and post-sweeper), so it was necessary to perform consistency checks in a case where the ion optics should be straightforward. Therefore, data was taken with the production target removed, and the beam placed at a defined point in the focal plane. Example comparison spectra are shown in Figure 4.22 for the beam travelling near the center of the magnet and focal plane. The lines show the perfect correlation line between the forward and inverse tracked parameters. The agreement of the data is reasonable, with the systematic deviations seen being insufficient to affect the reconstruction of the decay energy. The magnetic field is best understood near the center of the sweeper which results in the best agreement. As a result, the sweeper is generally tuned such that the primary reaction fragments of interest are focused near the center.

4.4.2 Neutron Momentum Four-Vector

The neutron four-momentum must be determined to fully reconstruct the mass of the initial unbound state. MoNA is time and position sensitive, so it is possible to construct this vector by measuring the neutron flight path and time of flight (ToF).

The full position vector (x,y,z) must be determined for each neutron, where the target is taken to be (0,0,0). The y and z components were determined by the measured location of the struck bar. Neutron strikes were assumed to occur at the center of each bar in the y and z directions, leading to a 5 cm uncertainty for those components of the position measurement. The x component was determined by the calibrated time difference between the two PMTs on the struck detector module, resulting in a FWHM resolution of 7.5 cm [46].

The neutron ToF was determined from the calibrated average of the timing signals from the PMTs on each end of a bar. The start time for each TDC came from the PMTs on the struck bar, while the stop time resulted from the target chamber

scintillator. The ToF was calibrated using cosmic ray muons and γ rays from the target as described in Section 4.2.5. The calculation of the neutron kinetic energy then proceeded by first determining the velocity:

$$v = \frac{R}{ToF} \tag{4.10}$$

Where R is the length of the position vector of the neutron strike. Then from relativistic mechanics:

$$\begin{aligned} \beta &= v/c & (4.11)\\ \gamma &= \sqrt{\frac{1}{1-\beta^2}} & (4.12)\\ KE_{neut} &= M_n(\gamma - 1) & (4.13) \end{aligned}$$

Where M_n is the rest mass of the neutron. With the trajectory and kinetic energy of the neutron thus determined, the four-vector can be fully defined and combined with the fragment four-vector to determine the decay energy.

4.5 Simulation

The measured decay energy spectrum is heavily influenced by resolution and acceptance effects resulting from the characteristics of the experimental setup. This smearing was accounted for numerically with a Monte Carlo simulation which included resolution and acceptance effects for each detector in the setup. Reaction dynamics and decay properties were used as inputs to create the neutron and charged fragment within this framework, and those particles were propagated to their respective detectors. Particles which missed a detector used in the analysis were flagged, and the response functions for each detector encountered were folded into the gen-

eration of a simulated dataset which could be analyzed using the same software the experimental data used. Therefore the two datasets could be directly compared and free parameters adjusted until spectra matched between the datasets.

The simulation begins with ^{22}N beam particles generated at the position of TCRDC1 with some energy and emittance distribution. The parameters associated with these degrees of freedom are fixed by comparing the simulated datasets to runs taken with the target removed and beam sent down the center of all detectors. The response of TCRDC1 (actual particle position convoluted with the x and y resolutions of the detector) is recorded, and the particle propagated forward through TCRDC2 to the reaction target. The reaction in the target is treated by a Goldhaber model [56] with a friction term [57]. The neutron decay is then modelled by one of the evaporation mechanisms discussed in Section 2.3. The neutron and fragment final products are treated separately from this point forward.

The neutron is first propagated to the window at the downstream end of the sweeper magnet, where the geometric acceptances of the window flag events which would have struck the steel encasing the window. From there the neutron is propagated to the front face of MoNA, where the acceptance of MoNA flags neutrons which miss it. The discretization in the y and z directions and position resolution along the length of the struck MoNA bar (x direction) are all accounted for in the final event properties.

The charged particle is propagated from the reaction target to CRDC1 by a transformation matrix generated by COSY as discussed in Section 4.4.1. Here the detector's resolutions and acceptances are accounted for, and the particle allowed to freely drift to CRDC2 and finally the thin scintillator, where their respective responses are recorded.

Because of the technical issue with the TCRDC2 x position spectrum, the incoming beam angular distribution could not be constrained directly. Instead, the

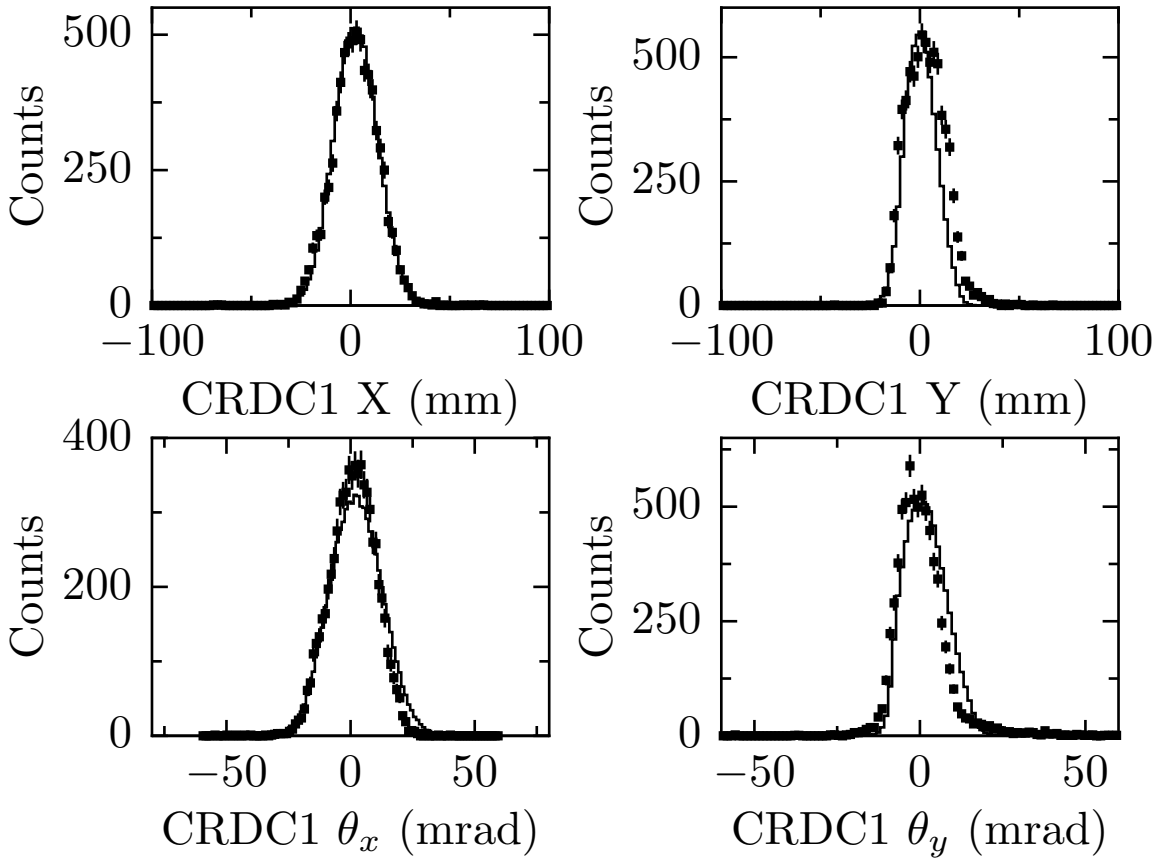

Figure 4.23: Comparison of simulation to data for ^{22}N reaction fragments.

position distribution for TCRDC1 was matched, and the angle and energy distributions matched by comparing to the focal plane CRDC spectra for a no-target, centered beam run. Figure 4.23 shows the comparison of simulation to data for this run. The agreement in x is quite good while the agreement in y degrades because of shortcomings in the magnetic field map's treatment of the y direction.

Reaction model parameters can then be verified by comparing charged fragment focal plane and inverse tracked spectra to data. Because of the relative mass between the neutron and fragment, the fragment focal plane emittance spectra are insensitive to the neutron evaporation. These checks are performed for each reaction fragment being analyzed, and the resulting spectra are shown for ^{20,18}C in Figures 4.24 and 4.25 respectively. The statistics are much lower than the unreacted beam run, but the agreement is still reasonable. Once again the best agreement is in x because of the properties of the magnetic field map. It should be mentioned that the comparison to reaction fragments probes a much wider region of the simulation's validity, as the individual emittance distributions are wider because of the reaction and the ^{18}C fragments populated the edge of the fragment acceptances which probes the fringe of the magnetic field map.

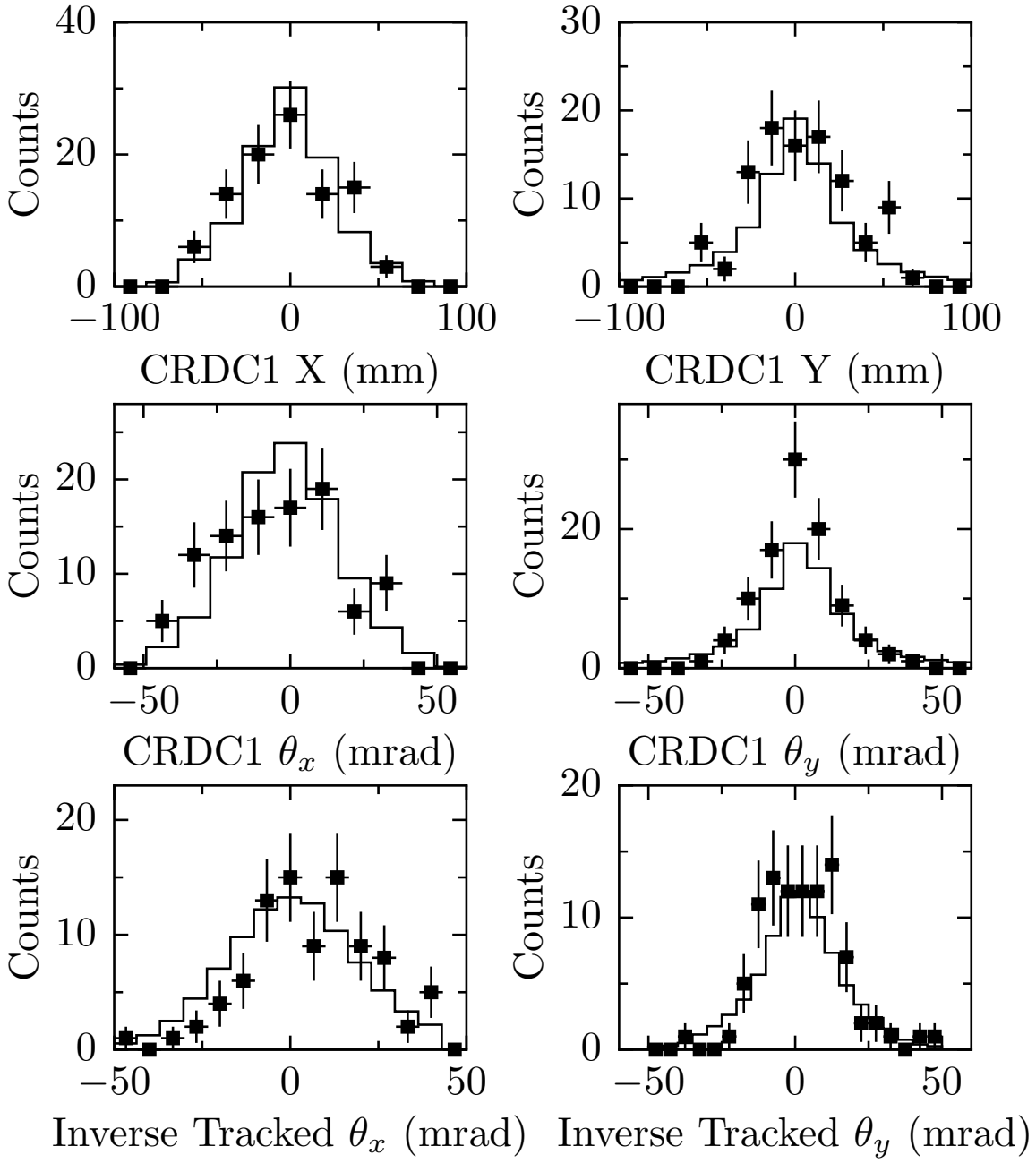

Figure 4.24: Comparison of simulation to data for ^{20}C reaction fragments.

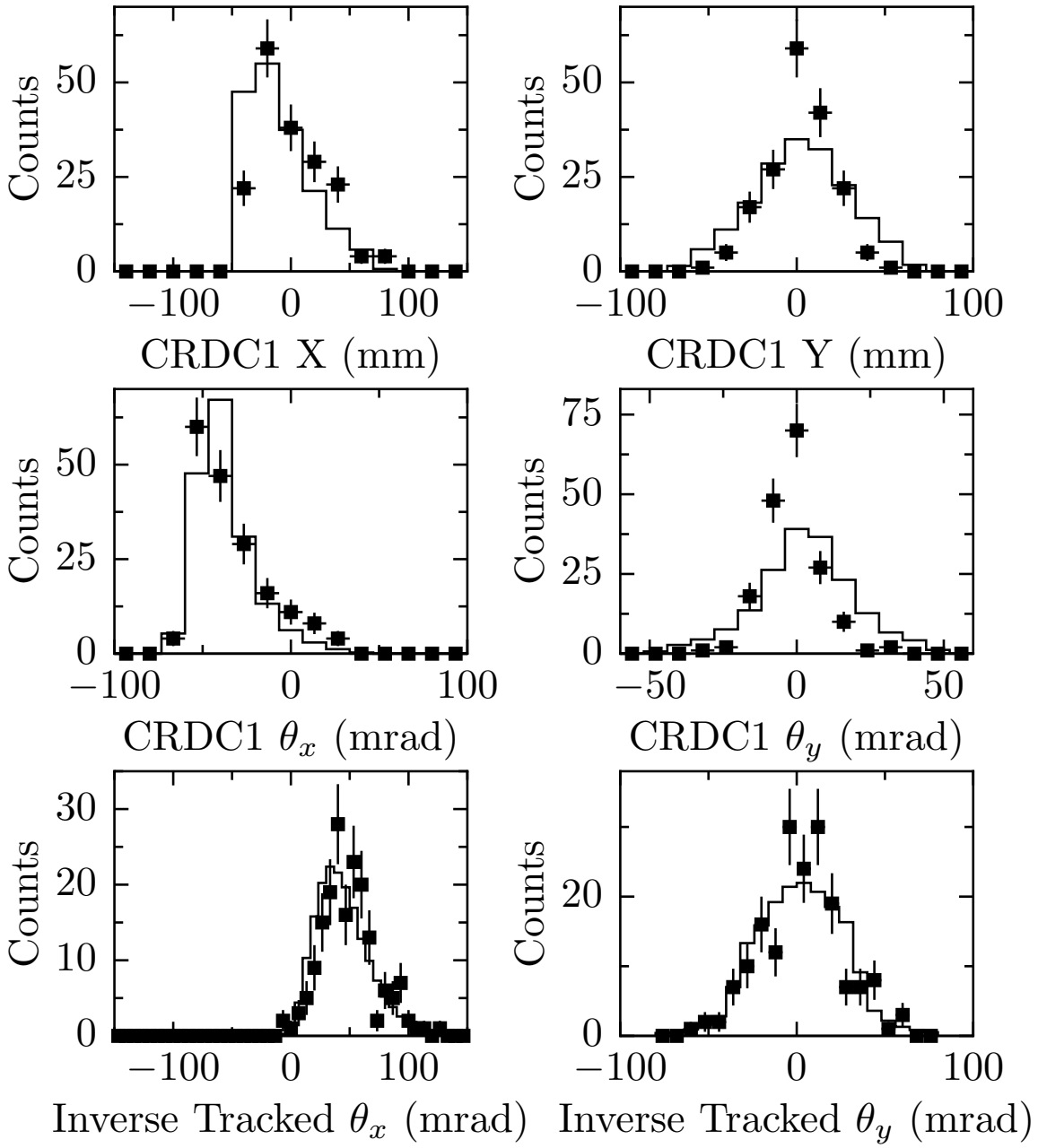

Figure 4.25: Comparison of simulation to data for ^{18}C reaction fragments.

Chapter 5

Discussion

As discussed in Section 2.2, ^{19}C was studied with the intent of determining whether its $5/2^+_1$ excited state was bound with respect to neutron decay and resolve questions raised by prior work. Nothing is know about ^{21}C beyond its instability, and populating states in this nucleus could provide constraints on the halo nucleus ^{22}C as well as probe the $\nu 1s_{1/2} - \nu 0d_{5/2}$ shell gap for N=15 isotones.

5.1 ^{19}C Results

In the intervening time between when prior measurements which extracted spectroscopic information for ^{19}C were published and this work, a new mass evaluation's results became available [58]. The new neutron separation energy of ^{19}C was 308±5 keV, compared to the old value of 580±9 keV [59]. As discussed in Section 3.1, the excitation energy of a neutron unbound state of a bound nucleus depends on the neutron separation energy $E^* = E_{decay} + S_n$ and as a result the position of the $5/2^+_2$ state in ^{19}C was shifted down by roughly 300 keV with the new evaluation. This effect is shown in the level scheme of Figure 5.1 which compares the level schemes generated from the two mass evaluations to theoretical calculations. The new mass

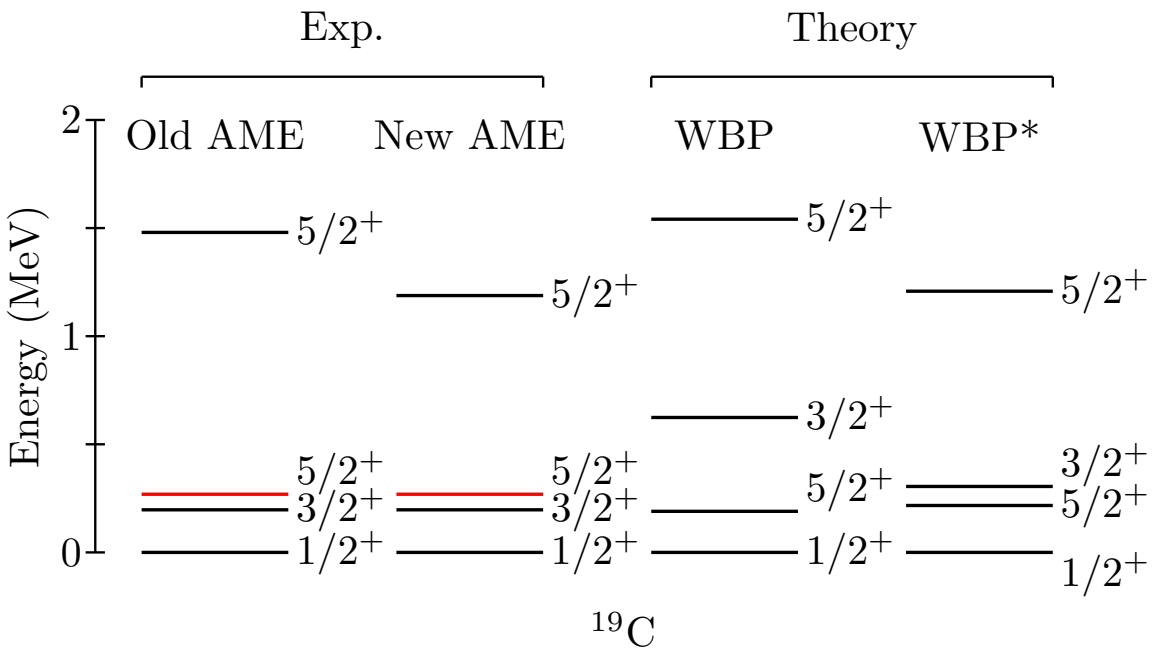

Figure 5.1: Comparison of level schemes for ^{19}C using old and new mass evaluations. Note that only the neutron unbound $5/2^+_2$ is affected by the change in relative mass. The new level scheme is better described by WBP*, consistent with observations for other neutron rich carbon isotopes.

causes the ^{19}C level scheme to be described better by the WBP* interaction, which puts it in agreement with the systematic compression of level schemes observed for the even-even neutron rich carbon isotopes. The position of the bound states was unaffected as excitation energy proceeds directly from the γ-ray energy associated with their de-excitation. The evaluation of the following results utilizes the new evaluated masses.

^{19}C was produced by 1p2n removal from the ^{22}N beam. While part of the cross section proceeded via a direct reaction, other reaction channels were also available. In particular, it was possible to populate high lying continuum states in ^{20,21}C which would decay by neutron emission to a variety of states in ^{19}C, schematically represented by Figure 2.11. Therefore, it was expected that in addition to any possible resonance structures, there would be an additional background contribution of the

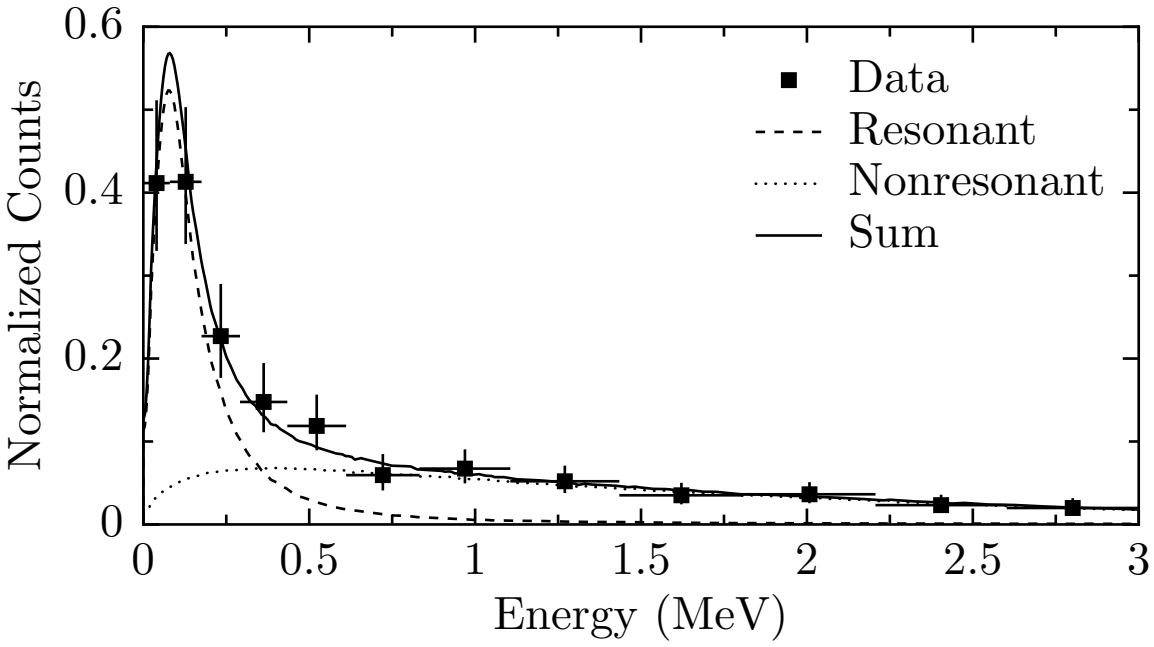

Figure 5.2: Best fit to experimental data (solid line) along with the relative contributions of a 76±14 keV resonance (dashed) constituting 54% of the spectrum and nonresonant background from high lying continuum states (dotted) modelled as a Maxwellian distribution with Θ=2.44 MeV.

form discussed in Section 2.3.3. Figure 5.2 demonstrates the best fit to data (solid line) utilizing the techniques set forth in Section 2.4. This fit had two components: a Breit-Wigner resonance (2.3.1) at 76±14 keV (dashed line) comprising 54% of the spectrum, and a non-resonant contribution in the form of a Maxwellian distribution (2.3.3) with a temperature of 2.44 MeV (dotted line). The cross section to populate the resonance was estimated to be 0.8±0.2 mb. The fit was not sensitive to the width of the distribution. As mentioned in 2.3.1, the energy dependent width of the Breit Wigner line shape for l=2 has only a weak dependence on the input width, and this combined with the resolution effects of the setup to make any constraint impossible. Therefore, the fits were performed using the expected single particle width of 10 keV.

Assignment of this state was guided by shell model calculations. As shown in the level scheme of Figure 5.3 and discussed in 2.2, a low lying triplet of states is expected, and within the uncertainties of these calculations it is possible that they

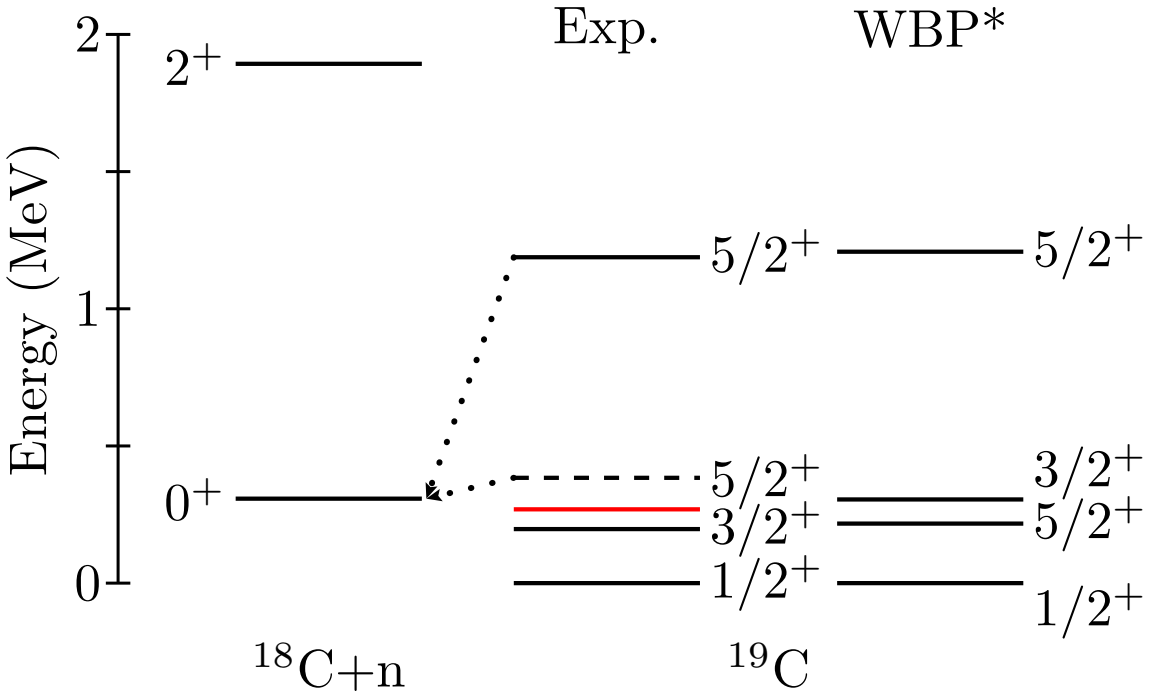

Figure 5.3: Level scheme of ^{19}C compared to theory relative to ^{18}C+n with both the Elekes state (solid red) and our state (dashed) included.

be neutron unbound. Given the agreement between [12, 16] regarding the placement and assignment of the $3/2^+$ and the determination of the ground state to be spin and parity $1/2^+$ [60], the best explanation for a near-threshold resonance would be the $5/2^+_1$ at 383±15 keV (shown as the dashed line in Figure 5.3). This immediately begs two questions. The first is why this work's spectrum differs from that of [17] as displayed in Figure 5.4, while the second is how to handle the prior assignment of the $5/2^+_1$ to a bound state at 269±7 keV [16].

Resolving the questions regarding our results compared to the other neutron spectroscopy work is a matter of interpreting the effects of reaction mechanisms. In particular, the two experiments used different reaction mechanisms to populate excited states in ^{19}C - [17] using (p,p') and this work using fragmentation. The selectivity of these reaction mechanisms is different. In particular, for (p,p') it is possible to compare the relative population of different transitions with the same Δl in a fashion

described by [61] by writing the cross section as:

$$\sigma_{pp'}(\theta) \approx |M_{pp'}|^2 A(\theta) \tag{5.1}$$

where

$$M_{pp'} = b_p^h M_p + b_n^h M_n \tag{5.2}$$

and M_* are transition matrix elements which can be calculated from shell model and b_* are interaction strengths which can be taken from literature. In particular, from [61], $b_p \approx 0.25$, $b_n \approx 0.75$. Therefore, the relative population strength can be defined:

$$\sigma_2/\sigma_1 = |M_{pp'2}|^2/|M_{pp'1}|^2 \tag{5.3}$$

Because the transitions of interest have the same Δl (both states being $5/2^+$ and populated from the $1/2^+$ ground state), the angular form factor $A(\theta)$ for their cross sections should be approximately the same and therefore will cancel. Calculating the relative cross section for the $5/2^+_*$ states therefore is a matter of obtaining the relevant matrix elements from shell model. These calculations were performed with the WBP and WBT interactions, and the resulting relative population estimation was $\sigma_2/\sigma_1 \geq 13$. The resulting contribution of the $5/2^+_1$ state to the RIKEN spectrum is displayed as the red bars on Figure 5.4. Within their estimated background it is possible that this state would go unnoticed.

To determine why this work did not observe the $5/2^+_2$, a $1p$-$2n$ stripping cross section estimate following the Eikonal method of [62] expanded to account for three particle stripping was performed for two cases [63]. First, a lower limit for the removal of a $\pi 1p_{1/2}$, $\nu 2s_{1/2}$, $\nu 1d_{5/2}$ cluster from ^{22}N was estimated to be 0.32 mb, and should dominantly feed the $5/2^+_1$.This result is consistent with our estimated cross section of 0.8$\pm$0.2 mb. The cross section to remove a $\pi 1p_{1/2}$, $2\nu 1d_{5/2}$ cluster

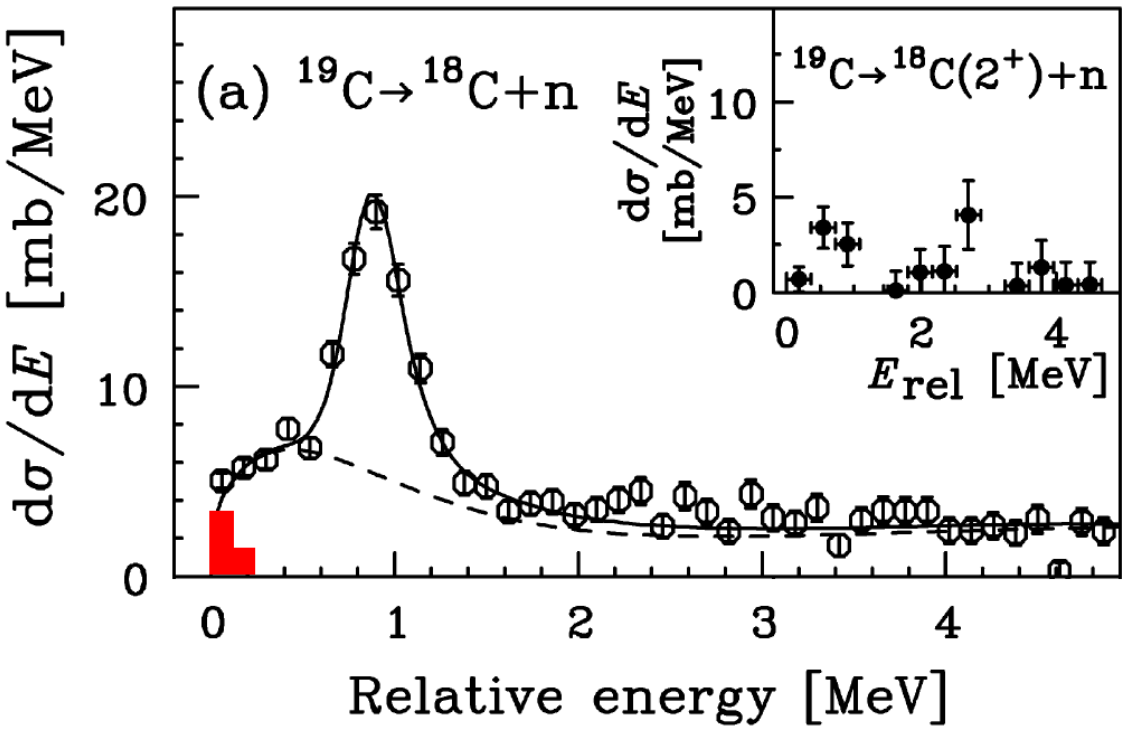

Figure 5.4: Experimental spectrum from [17] with the estimated strength of the $5/2^+_1$ shown in red.

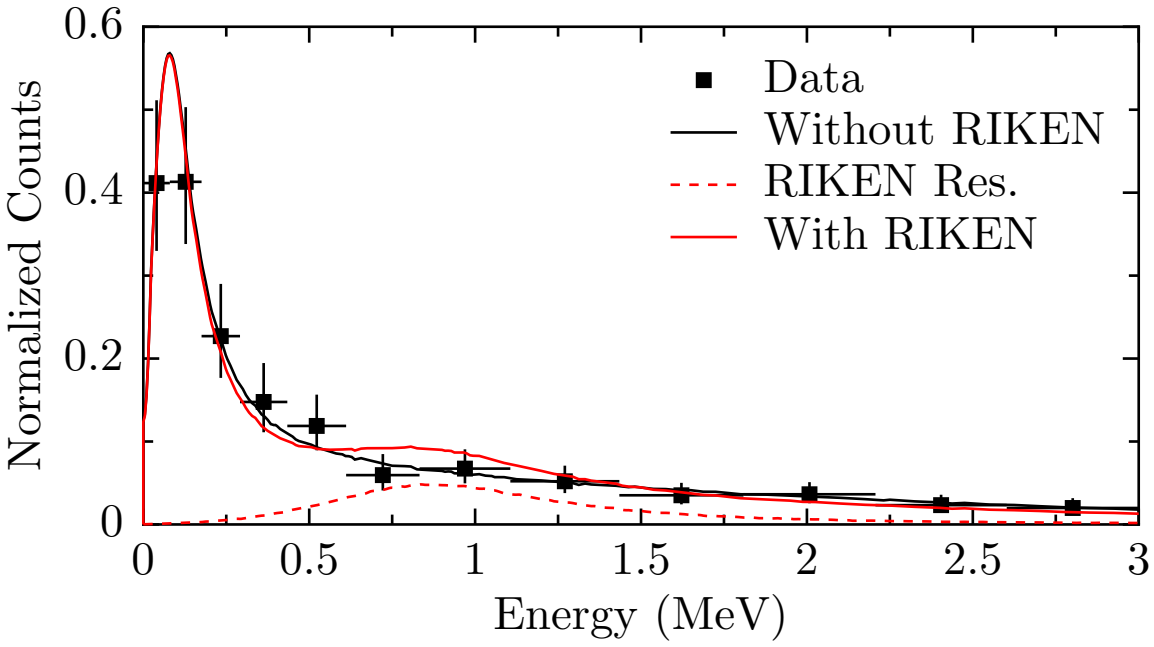

Figure 5.5: Our experimental spectrum with a best fit including the $5/2^+_2$ state from [17] with relative population determined by cross section estimates from [63].

from the ^{22}N beam was calculated to be 0.69 mb, a process which could populate either the ground state or the $5/2^+_2$ in ^{19}C. Using WBP calculations, we estimated the overlap to the ground state to be twice that to the $5/2^+_2$, which results in a cross section of 0.23 mb to populate the $5/2^+_2$. Folding this state into our simulated data set with the relative population constrained to $\sigma_2/\sigma_1 = 0.23$ mb$/0.32$ mb $= 0.71$ results in the solid red line in Figure 5.5. This shows a comparison between best fit results with and without the inclusion of the $5/2^+_2$, and which demonstrates that the experimental setup's efficiency and resolution for that state would not be sufficient to resolve it from nonresonant background given the limited statistics of the measurement.

This leaves the question of prior assignment of the $5/2^+_1$ to a bound state. A recent cross section measurement for neutron stripping from a ^{20}C beam producing ^{18}C requires the $5/2^+_1$ to be neutron unbound to reproduce the magnitude of the cross section [63]. The table for their ^{20}C stripping results is shown in Figure 5.6,

Reaction	E_x (MeV)	J^π	$\sigma_{-1n(e)}$ mb	σ_{exp} (mb)	R_s
(^{20}C(0^+),^{19}C(J^π))	0.190	$5/2^+$	111.17		
S_{1n}(^{20}C)=2.90 MeV		Inclusive	192.2	126(10)	0.66(5)

Figure 5.6: Calculated neutron stripping cross sections of the $5/2^+_1$ relative to the total [63].

and the predicted contribution of the $5/2^+_1$ shown relative to the total predicted cross section. In particular, it is worth noting that the $5/2^+_1$ constitutes roughly 60% the total calculated cross section. Without that contribution their description of the stripping process breaks down, and would show a stark aberration from the cross section systematics observed in that work.

Furthermore, Elekes *et al.* quote a cross section of 4.2 ± 0.5 mb to populate the $5/2^+_1$, which is a factor of 2 lower than that of the $5/2^+_2$ (8.6±0.4 mb) [17]. This relative population ratio of 2 is a factor of 6 lower than the ratio of 13 calculated predicted by shell model calculations.

The level scheme in Figure 5.3 demonstrates that the WBP interaction does not capture the known level density well, and the WBP*, while performing better still incorrectly predicts the ordering of the excited states. The performance of the WBP interaction can be understood as the phenomenological description of the *sd* shell neutrons breaking down for such asymmetric nuclear matter. In particular, the reduction in TBME for WBP* suggests that the neutrons are less bound because of the relative absence of protons compared to the nuclei which were fit over to produce the neutron sd shell interaction utilized by WBP. It is possible that extending the fit range of the WBP to include more recent neutron rich data would improve its description of these level schemes.

However, the large degree of reduction and incorrect ordering suggests there might be physics beyond the interaction mechanisms going into the WBP interaction. In particular, [6] performed calculations on the Z=8 isotopic chain and was able to

reproduce the binding of the neutron rich isotopes and correctly predict the location of the oxygen drip line by including three body forces in an interaction model developed from fundamental NN forces. It is possible that calculations in a more realistic interaction framework such as this would better describe the neutron rich carbon isotopes.

5.2 ^{21}C Results

Figure 5.7(a) shows the experimentally determined decay energy for ^{21}C. The data (black squares) are distributed over a broad energy range and do not exhibit any obvious resonance. A sharp resonance was not expected because the $\ell = 2$ states were not expected to be populated in the proton removal reaction from the ^{22}N ground state, which is accepted to possess a J^{π} of 0^{-} [13, 64]. The calculated spectroscopic factors for the $\ell = 2$ $5/2^{+}$ and $3/2^{+}$ excited states in ^{21}C are 0 and 0.05, respectively. In contrast, the spectroscopic factor for populating the $\ell = 0$ $1/2^{+}$ state is 0.75.

Therefore, the decay energy spectrum was fit assuming a pure s-wave decay, with the line shape for the decay determined as in [31]. The scattering length was allowed to freely vary in the fitting process from 0 to -100 fm with all other parameters constrained to fixed values. Because of the low number of counts in the spectrum, the fitting process used an unbinned likelihood technique. The fitting process favored the limit of $|a_s| < 1.5$ fm, with the best fit being $a_s = -0.05$ fm (shown in Figure 1(a) as grey triangles). Folding geometrical acceptances, detector resolutions, and live time together we estimate the production cross section for this state to be 1.1 ± 0.23 mb. Figure 5.7(b) demonstrates the sensitivity of the present set-up to any potential low energy virtual state. It compares the line shape for an s-wave at the limit of $a_s = -1.5$ fm (dot-dashed line) with the line shapes for s-wave decays with $a_s = -15$ fm (dashed line) and $a_s = -50$ fm (solid line). It is clear that any low lying s-wave state

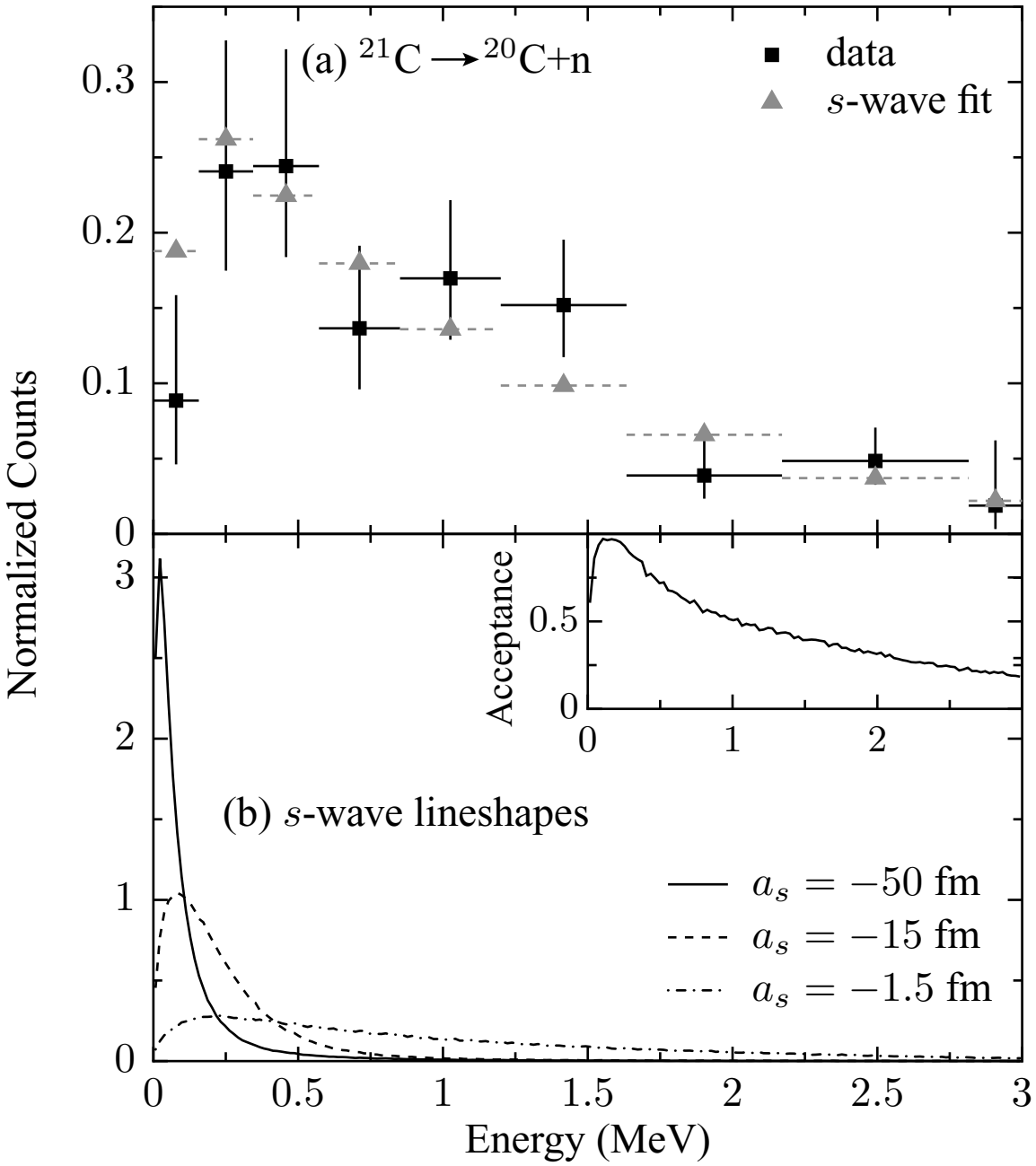

Figure 5.7: Reconstructed decay energy spectrum for ^{21}C (a), where squares represent data points and triangles represent an s-wave curve of a_s = -0.05 fm with the same binning as the data. Panel (b) demonstrates the sensitivity of the setup to a low-lying virtual state by showing simulated decay energy line shapes for s-waves with differing scattering lengths. The inset shows the geometric efficiency of the setup as a function of decay energy.

would have been apparent in the decay energy spectrum.

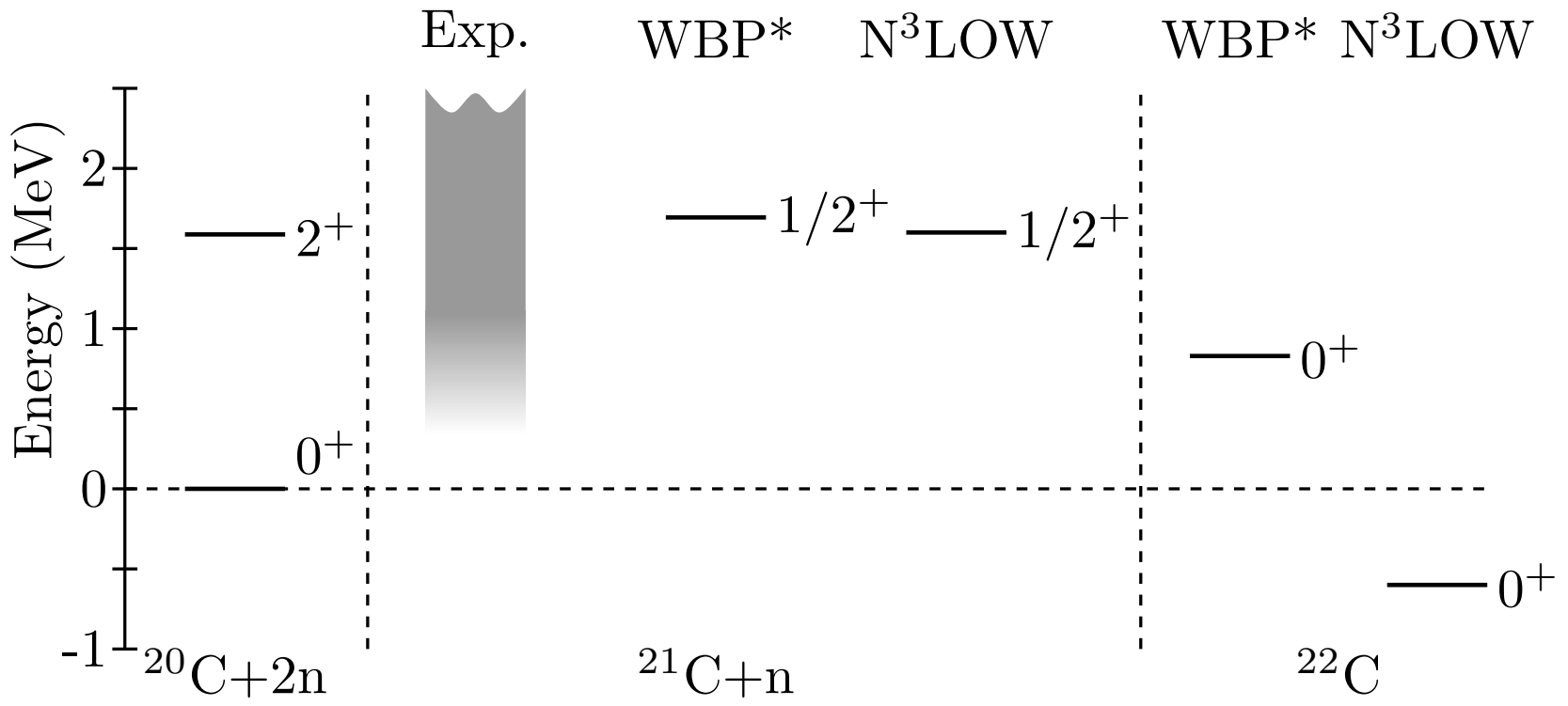

Figure 5.8: Experimental level schemes of ^{20,21}C and theoretical level schemes of ^{21,22}C, with ^{20}C data from [65, 12] and N^{3}LOW predictions from [66]. The lack of a resonance structure in the ^{21}C decay energy spectrum indicates that the virtual state's strength is broadly spread as indicated by the grey region. This is consistent with WBP* and N^{3}LOW calculations which predict ^{21}C to be unbound by 1.7 MeV and 1.6 MeV, respectively. The calculations show a 1.2 MeV spread in the predicted ^{22}C binding energy.

Figure 5.8 compares the present experimental results with two different shell model calculations. First, we performed calculations with NuShellX@MSU [67] in a truncated $s-p-sd-pf$ model space with a modified WBP [7] interaction labeled WBP*. In this interaction the neutron *sd* TBME were reduced to 0.75 of their original value in order to reproduce a number of observables in neutron rich carbon isotopes [12]. The second model is based on an effective Hamiltonian from the chiral N^{3}LOW nucleon-nucleon potential [66]. As shown in the figure, the models agree in their description of ^{21}C, but have a 1.2 MeV spread in predicted binding for ^{22}C. This suggests a breakdown in the shell model description of ^{22}C.

As discussed in Section 2.2.3, Yamashita *et al.* derived a relationship between the ^{22}C two-neutron separation energy and the energy of the virtual state in ^{21}C within the renormalized zero-range three-body model of [27]. Figure 5.9 demonstrates this relationship as lines of constant decay energy for the virtual state in ^{21}C through a phase space of two-neutron separation energy $S_{2\mathrm{n}}$ and ^{22}C halo radius r_{n}. This sort of correlation has been observed in other halo systems [23]. The lines shown correspond to ^{21}C virtual state energies ranging from 0 to 100 keV in steps of 10 keV.

The shaded grey region indicates where ^{22}C is likely to reside in this parameter space given current experimental constraints. The limits on r_{n} were calculated from the matter radius of ^{22}C (extracted from the reaction cross section via finite-range Glauber analysis under an optical-limit approximation) assuming a ^{20}C core [26], and the upper boundary is a consequence of $S_{\mathrm{n}} < 0$ for ^{21}C. The original work restricted calculations to $S_{2\mathrm{n}} \geq 100$ keV. As shown in Figure 5.9, the 100 keV virtual state curve crosses into the experimentally constrained region at approximately $S_{2\mathrm{n}} = 100$ keV, which limits the range of predicted virtual state energies in ^{21}C to $E \leq 100$ keV for this calculation space. A 100 keV virtual state energy corresponds to $a_s = -15$ fm, which is not supported by our data.

If the calculations were extended to $S_{2\mathrm{n}} < 100$ keV, it might be possible to

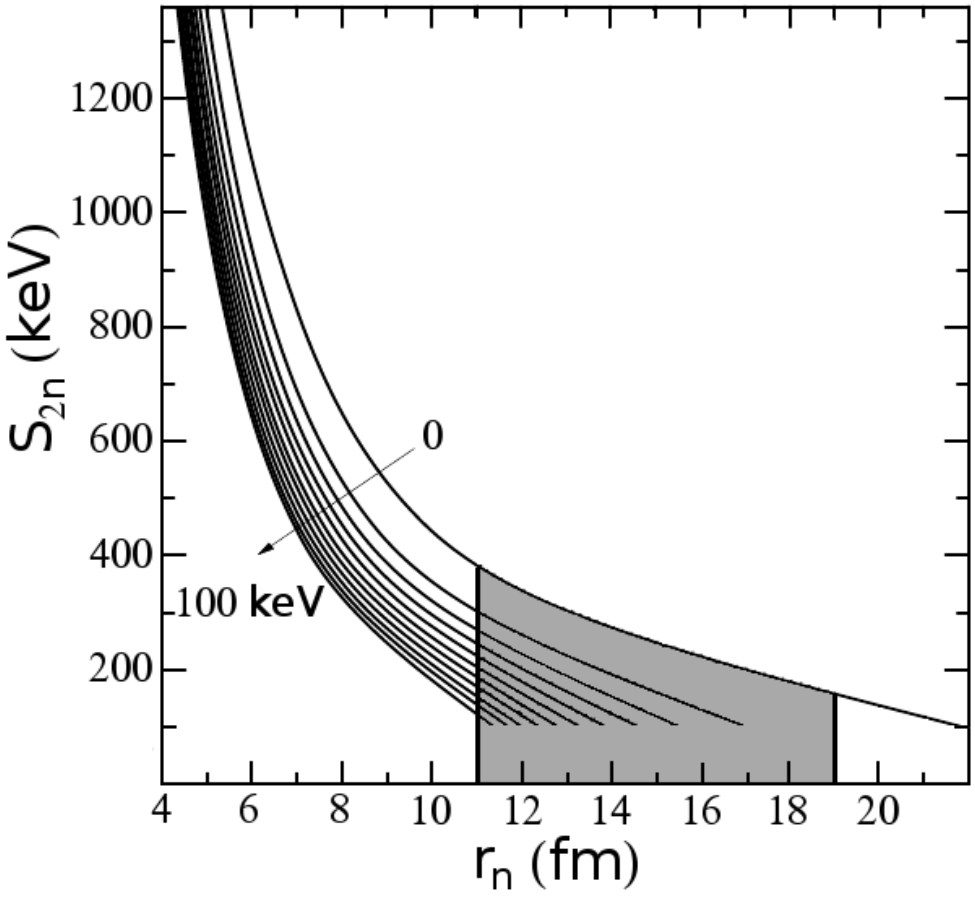

Figure 5.9: Correlations between the two-neutron separation energy and rms neutron halo radius in ^{22}C for given positions of a virtual state in ^{21}C from [27]. The shaded grey area indicates the region of interest to find the ^{22}C S_{2n} and r_n. Constraints on r_n are extracted from the measured reaction cross section of ^{22}C.

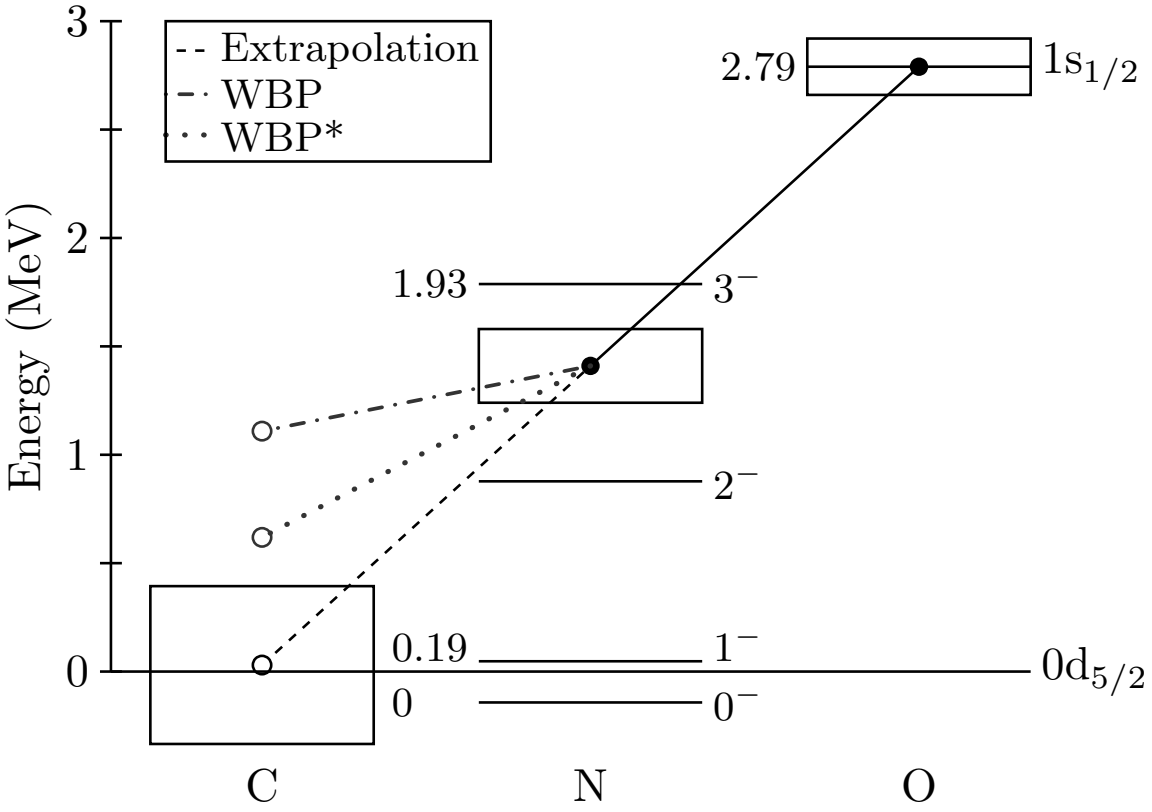

Figure 5.10: Evolution of the $\nu 1s_{1/2} - \nu 0d_{5/2}$ shell gap for N=15 Oxygen, Nitrogen, and Carbon isotones. The dashed line shows a linear extrapolation of the gap to Carbon following the prescription of [20], while the dotted and dashdotted lines show the results of WBP* and WBP calculations respectively. Experimental data taken from [18, 13, 19].

calculate correlations in the S_{2n} / r_n space which are consistent with our limit on the scattering length. Given the crossing point for the 100 keV virtual state energy curve at $S_{2n} = 100$ keV, such a curve calculated for a virtual state with $a_s = -1.5$ fm would require $S_{2n} \ll 100$ keV. Therefore, we conclude that the limit of $|a_s| < 1.5$ fm placed on the virtual state energy in ^{21}C constrains the ^{22}C S_{2n} to be much less than 100 keV, which further reinforces the current evidence that ^{22}C is a loosely bound halo system.

It would be interesting to measure the $\nu 1s_{1/2} - \nu 0d_{5/2}$ shell gap for N=15 isotones. In ^{21}C, this amounts to measuring the energy gap between the $1/2^+$ (one particle in

the $\nu s_{1/2}$) and $5/2^+$ (one hole in the $\nu d_{5/2}$). While this experiment did not populate the $5/2^+$, it is possible to speculate on where the $5/2^+$ might appear in a decay energy spectrum for an experiment that would populate that state. As discussed in [18], one method of predicting the evolution of the shell gap is a linear extrapolation first put forth in [20]. The dashed line in Figure 5.10 demonstrates the result of this method, whereby one observes that the gap disappears. Within the uncertainty of the extrapolation, the levels could in fact invert in a fashion similar to the level inversion observed in ^{15}C [20]. By this prediction, an experiment populating the $5/2^+$ would observe the resonance above 800 keV. The dash-dotted and dotted lines in Figure 5.10 show the WBP and WBP* shell model predictions of 0.6 MeV and 1.1 MeV for the energy gap respectively. There is some precedent for shell gaps to bend over near the neutron dripline for N=7 [68] which lends credence to the shell model prediction. By this prediction, the $5/2^+$ state should be above 1.6 MeV in decay energy. Given the spread in possible locations for this state, it would be interesting to populate the $5/2^+$. Shell model calculations predict the ground state wavefunction of ^{20}C to posses a mixed configuration which may allow ^{20}C(d,p)^{21}C to populate both states.

Chapter 6

Summary and Conclusions

In this work, the excitation energy of a neutron unbound excited state of ^{19}C was measured, and a limit placed on the scattering length of a virtual state in ^{21}C. These states were populated by nucleon removal reactions from a ^{22}N beam produced by fast fragmentation at the Coupled Cyclotron Facility at the NSCL. Charged fragments resulting from these reactions were bent from the beam axis by a large-gap dipole magnet and identified by a suite of charged particle detectors. Neutrons were detected at forward angles by MoNA, and the decay energy of the neutron evaporation reconstructed using the invariant mass method. A Monte Carlo simulation was used to account for resolution and acceptance effects in the modelling of the data, and the decay energy spectra were fit using combinations of several different line shapes depending on the physics case.

In the case of ^{19}C, the fitting took the form of a Breit-Wigner resonance at 76 ± 14 keV comprising 54% the total spectrum, and a Maxwellian distribution for the remaining non-resonant background. Utilizing the latest evaluated mass tables, this state was assigned to be an excited state of ^{19}C at 383 ± 15 keV.

Shell model calculations were performed to aid in the interpretation of this result. Calculations were performed in a truncated $s-p-sd-pf$ model space using both the

WBP and a modified WBP* interaction, where WBP* had empirical modifications performed to reproduce observables for neutron rich carbon isotopes. Comparison to these calculations results in the assignment of the state in ^{19}C to the $5/2^+_1$ state. The resulting experimental level scheme suggests physics beyond the WBP* interaction, and it is speculated that more realistic interactions developed from fundamental 2- and 3-body forces may be able to reproduce the level schemes.

^{21}C was fit using a pure s-wave line shape, and the fit favored the limit of $|a_S| <$ 1.5 fm. This result was compared to predictions from a renormalized zero-range three-body model which calculated correlations between the energy of the ^{21}C virtual state, the matter radius of the halo nucleus ^{22}C, and the two-neutron separation energy for ^{22}C. This comparison suggests that ^{22}C is bound by much less than 100 keV, which reinforces the current evidence that ^{22}C is a loosely bound halo system.

This work has put a constraint on one of the two levels in ^{21}C necessary to measure the N=14 shell gap in carbon. Preliminary calculations suggest that a future experiment utilizing ^{20}C(d,p)^{21}C would likely populate both the $1/2^+$ and the $5/2^+$ and be able to determine this energy gap.

BIBLIOGRAPHY

[1] I. Brida, S. C. Pieper, and R. B. Wiringa, "Quantum monte carlo calculations of spectroscopic overlaps in $a \leqslant 7$ nuclei," *Phys. Rev. C*, vol. 84, p. 024319, Aug 2011.

[2] M. G. Mayer, "On closed shells in nuclei," *Phys. Rev.*, vol. 74, pp. 235–239, Aug 1948.

[3] M. G. Mayer, "On closed shells in nuclei. ii," *Phys. Rev.*, vol. 75, pp. 1969–1970, Jun 1949.

[4] O. Haxel, J. H. D. Jensen, and H. E. Suess, "On the "magic numbers" in nuclear structure," *Phys. Rev.*, vol. 75, pp. 1766–1766, Jun 1949.

[5] R. D. Woods and D. S. Saxon, "Diffuse surface optical model for nucleon-nuclei scattering," *Phys. Rev.*, vol. 95, pp. 577–578, Jul 1954.

[6] T. Otsuka, T. Suzuki, J. D. Holt, A. Schwenk, and Y. Akaishi, "Three-body forces and the limit of oxygen isotopes," *Phys. Rev. Lett.*, vol. 105, p. 032501, Jul 2010.

[7] E. K. Warburton and B. A. Brown, "Effective interactions for the 0p1sd nuclear shell-model space," *Phys. Rev. C*, vol. 46, pp. 923–944, Sep 1992.

[8] T. Otsuka *et al.*, "Magic numbers in exotic nuclei and spin-isospin properties of *NN* interaction," *Phys. Rev. Lett.*, vol. 87, p. 082502, 2001.

[9] T. Otsuka, T. Suzuki, R. Fujimoto, H. Grawe, and Y. Akaishi, "Evolution of Nuclear Shells due to the Tensor Force," *Phys. Rev. Lett.*, vol. 95, p. 232502, 2005.

[10] T. Otsuka, T. Matsuo, and D. Abe, "Mean Field with Tensor Force and Shell Structure of Exotic Nuclei," *Phys. Rev. Lett.*, vol. 97, p. 162501, 2006.

[11] M. Stanoiu, M. Belleguic, Z. Dombrdi, D. Sohler, F. Azaiez, B. A. Brown, M. J. Lopez-Jimenez, M. G. Saint-Laurent, O. Sorlin, Y.-E. Penionzhkevich, N. L. Achouri, J. C. Anglique, C. Borcea, C. Bourgeois, J. M. Daugas, F. De Oliveira-Santos, Z. Dlouhy, C. Donzaud, J. Duprat, S. Grvy, D. Guillemaud-Mueller, S. Leenhardt, M. Lewitowicz, S. M. Lukyanov, W. Mittig, M. G. Porquet, F. Pougheon, P. Roussel-Chomaz, H. Savajols, Y. Sobolev, C. Stodel, and J. Timr, "Observation of bound excited states in ¹⁵b," *The European Physical Journal A - Hadrons and Nuclei*, vol. 22, pp. 5–8, 2004. 10.1140/epja/i2004-10078-8.

[12] M. Stanoiu *et al.*, "Disappearance of the N=14 shell gap in the carbon isotopic chain," *Phys. Rev. C*, vol. 78, p. 034315, 2008.

[13] D. Sohler, M. Stanoiu, Z. Dombrádi, F. Azaiez, B. A. Brown, M. G. Saint-Laurent, O. Sorlin, Y.-E. Penionzhkevich, N. L. Achouri, J. C. Angélique, M. Belleguic, C. Borcea, C. Bourgeois, J. M. Daugas, F. D. Oliveira-Santos, Z. Dlouhy, C. Donzaud, J. Duprat, Z. Elekes, S. Grévy, D. Guillemaud-Mueller, F. Ibrahim, S. Leenhardt, M. Lewitowicz, M. J. Lopez-Jimenez, S. M. Lukyanov, W. Mittig, J. Mrázek, F. Negoita, Z. Podolyák, M. G. Porquet, F. Pougheon, P. Roussel-Chomaz, H. Savajols, G. Sletten, Y. Sobolev, C. Stodel, and J. Timár, "In-beam γ-ray spectroscopy of the neutron-rich nitrogen isotopes $^{19-22}$n," *Phys. Rev. C*, vol. 77, p. 044303, Apr 2008.

[14] H. Ueno, K. Asahi, H. Izumi, K. Nagata, H. Ogawa, A. Yoshimi, H. Sato, M. Adachi, Y. Hori, K. Mochinaga, H. Okuno, N. Aoi, M. Ishihara, A. Yoshida, G. Liu, T. Kubo, N. Fukunishi, T. Shimoda, H. Miyatake, M. Sasaki, T. Shirakura, N. Takahashi, S. Mitsuoka, and W.-D. Schmidt-Ott, "Magnetic moments of $n17$ and $b17$," *Phys. Rev. C*, vol. 53, pp. 2142–2151, May 1996.

[15] P. Thirolf, B. Pritychenko, B. Brown, P. Cottle, M. Chromik, T. Glasmacher, G. Hackman, R. Ibbotson, K. Kemper, T. Otsuka, L. Riley, and H. Scheit, "Spectroscopy of the 21+ state in 22o and shell structure near the neutron drip line," *Physics Letters B*, vol. 485, no. 1-3, pp. 16 – 22, 2000.

[16] Z. Elekes, Z. Dombrdi, R. Kanungo, H. Baba, Z. Flp, J. Gibelin, . Horvth, E. Ideguchi, Y. Ichikawa, N. Iwasa, H. Iwasaki, S. Kanno, S. Kawai, Y. Kondo, T. Motobayashi, M. Notani, T. Ohnishi, A. Ozawa, H. Sakurai, S. Shimoura, E. Takeshita, S. Takeuchi, I. Tanihata, Y. Togano, C. Wu, Y. Yamaguchi, Y. Yanagisawa, A. Yoshida, and K. Yoshida, "Low-lying excited states in 17,19c," *Physics Letters B*, vol. 614, no. 3-4, pp. 174 – 180, 2005.

[17] Y. Satou *et al.*, "Unbound excited states in 19,17C," *Phys. Lett.*, vol. B660, pp. 320–325, 2008.

[18] M. J. Strongman *et al.*, "Disappearance of the N=14 shell," *Phys. Rev.*, vol. C80, p. 021302, 2009.

[19] A. Schiller, N. Frank, T. Baumann, D. Bazin, B. A. Brown, J. Brown, P. A. DeYoung, J. E. Finck, A. Gade, J. Hinnefeld, R. Howes, J.-L. Lecouey, B. Luther, W. A. Peters, H. Scheit, M. Thoennessen, and J. A. Tostevin, "Selective population and neutron decay of an excited state of $o23$," *Phys. Rev. Lett.*, vol. 99, p. 112501, Sep 2007.

[20] I. Talmi and I. Unna, "Order of levels in the shell model and spin of $be11$," *Phys. Rev. Lett.*, vol. 4, pp. 469–470, May 1960.

[21] I. Tanihata, H. Hamagaki, O. Hashimoto, Y. Shida, N. Yoshikawa, K. Sugimoto, O. Yamakawa, T. Kobayashi, and N. Takahashi, "Measurements of interaction cross sections and nuclear radii in the light p-shell region," *Phys. Rev. Lett.*, vol. 55, pp. 2676–2679, Dec 1985.

[22] P. G. Hansen, A. S. Jensen, and B. Jonson, "Nuclear halos," *Annu. Rev. Nucl. Sci.*, vol. 45, no. 1, pp. 591–634, 1995.

[23] P. G. Hansen and B. Jonson, "The neutron halo of extremely neutron-rich nuclei," *Europhys. Lett.*, vol. 4, no. 4, p. 409, 1987.

[24] A. S. Jensen, K. Riisager, D. V. Fedorov, and E. Garrido, "Structure and reactions of quantum halos," *Rev. Mod. Phys.*, vol. 76, pp. 215–261, Feb 2004.

[25] C. Gaulard, C. Bachelet, G. Audi, C. Gunaut, D. Lunney, M. de Saint Simon, M. Sewtz, and C. Thibault, "Mass measurements of the exotic nuclides 11li and 11,12be performed with the mistral spectrometer," *Nuclear Physics A*, vol. 826, no. 1-2, pp. 1 – 23, 2009.

[26] K. Tanaka, T. Yamaguchi, T. Suzuki, T. Ohtsubo, M. Fukuda, D. Nishimura, M. Takechi, K. Ogata, A. Ozawa, T. Izumikawa, T. Aiba, N. Aoi, H. Baba, Y. Hashizume, K. Inafuku, N. Iwasa, K. Kobayashi, M. Komuro, Y. Kondo, T. Kubo, M. Kurokawa, T. Matsuyama, S. Michimasa, T. Motobayashi, T. Nakabayashi, S. Nakajima, T. Nakamura, H. Sakurai, R. Shinoda, M. Shinohara, H. Suzuki, E. Takeshita, S. Takeuchi, Y. Togano, K. Yamada, T. Yasuno, and M. Yoshitake, "Observation of a large reaction cross section in the drip-line nucleus ^{22}**C**," *Phys. Rev. Lett.*, vol. 104, p. 062701, Feb 2010.

[27] M. Yamashita, R. M. de Carvalho, T. Frederico, and L. Tomio, "Constraints on two-neutron separation energy in the borromean 22c nucleus," *Phys. Lett. B*, vol. 697, no. 1, pp. 90 – 93, 2011.

[28] I. J. Thompson and M. V. Zhukov, "Effects of ^{10}Li virtual states on the structure of ^{11}Li," *Phys. Rev. C*, vol. 49, pp. 1904–1907, Apr 1994.

[29] A. M. Lane and R. G. Thomas, "R-matrix theory of nuclear reactions," *Rev. Mod. Phys.*, vol. 30, pp. 257–353, Apr 1958.

[30] F. Nunes, *Nuclear Reactions for Astrophysics: Principles, Calculation and Applications of Low-Energy Reactions*. Cambridge University Press, 2009.

[31] G. Blanchon, A. Bonaccorso, D. M. Brink, A. Garcia-Camacho, and N. Vinh Mau, "Unbound exotic nuclei studied by projectile fragmentation," *Nucl. Phys.*, vol. A784, pp. 49–78, 2007.

[32] G. F. Bertsch, K. Hencken, and H. Esbensen, "Nuclear Breakup of Borromean Nuclei," *Phys. Rev.*, vol. C57, pp. 1366–1377, 1998.

[33] K. J. L. Couteur and D. W. Lang, "Neutron evaporation and level densities in excited nuclei," *Nuclear Physics*, vol. 13, no. 1, pp. 32 – 52, 1959.

[34] J. Blatt and V. Weisskopf, *Theoretical Nuclear Physics*. Springer-Verlag, New York, 1979.

[35] M. Galassi, *GNU Scientific Library Reference Manual*, 3rd ed.

[36] F. James, *Statistical Methods in Experimental Physics*. World Scientific, 2nd ed., 2006.

[37] C. S. Sumithrarachchi, D. J. Morrissey, A. D. Davies, D. A. Davies, M. Facina, E. Kwan, P. F. Mantica, M. Portillo, Y. Shimbara, J. Stoker, and R. R. Weerasiri, "States in ^{22}o via β decay of ^{22}n," *Phys. Rev. C*, vol. 81, p. 014302, Jan 2010.

[38] Isao and Tanihata, "Radioactive beam facilities and their physics program," *Nuclear Physics A*, vol. 553, no. 0, pp. 361 – 372, 1993.

[39] F. Marti, P. Miller, D. Poe, M. Steiner, J. Stetson, and X. Y. Wu, "Commissioning of the coupled cyclotron system at nscl," *AIP Conference Proceedings*, vol. 600, no. 1, pp. 64–68, 2001.

[40] D. J. Morrissey, B. M. Sherrill, M. Steiner, A. Stolz, and I. Wiedenhoever, "Commissioning the a1900 projectile fragment separator," *Nuc. Instr. Meth. in Phys. B*, vol. 204, pp. 90 – 96, 2003.

[41] M. Bird, S. Kenney, J. Toth, H. Weijers, J. DeKamp, M. Thoennessen, and A. Zeller, "System testing and installation of the nhmfl/nscl sweeper magnet," *IEEE Trans. Appl. Supercond.*, vol. 15, pp. 1252 – 1254, 2005.

[42] T. Baumann, J. Boike, J. Brown, M. Bullinger, J. Bychoswki, S. Clark, K. Daum, P. DeYoung, J. Evans, J. Finck, N. Frank, A. Grant, J. Hinnefeld, G. Hitt, R. Howes, B. Isselhardt, K. Kemper, J. Longacre, Y. Lu, B. Luther, S. Marley, D. McCollum, E. McDonald, U. Onwuemene, P. Pancella, G. Peaslee, W. Peters, M. Rajabali, J. Robertson, W. Rogers, S. Tabor, M. Thoennessen, E. Tryggestad, R. Turner, P. VanWylen, and N. Walker, "Construction of a modular large-area neutron detector for the nscl," *Nuc. Instr. Meth. in Phys. A*, vol. 543, no. 2-3, pp. 517 – 527, 2005.

[43] C. Freigang, *Building the Sweeper Magnet Focal Plane Detector*. PhD thesis, Michigan State University, 2001.

[44] S.-G. Crystals, "Bc-400, bc-404, bc-408, bc-412, bc-416 premium plastic scintillators," 2005.

[45] N. Frank, *Spectroscopy of neutron unbound states in neutron rich oxygen isotopes*. PhD thesis, Michigan State University, 2006.

[46] W. Peters, *Study of Neutron Unbound States Using the Modular Neutron Array (MoNA)*. PhD thesis, Michigan State University, 2007.

[47] R. Fox, "Spectcl user's guide," tech. rep., NSCL/MSU, 2003.

[48] R. Brun and F. Rademakers, "Root – an object oriented data analysis framework," *Nuclear Instruments and Methods in Physics Research Section A: Accelerators, Spectrometers, Detectors and Associated Equipment*, vol. 389, no. 1-2, pp. 81 – 86, 1997. New Computing Techniques in Physics Research V.

[49] E. Jones, T. Oliphant, P. Peterson, *et al.*, "SciPy: Open source scientific tools for Python," 2001–.

[50] F. Pérez and B. E. Granger, "IPython: a System for Interactive Scientific Computing," *Comput. Sci. Eng.*, vol. 9, pp. 21–29, May 2007.

[51] J. Lehmann, M. Schindler, and A. Wobst, "Pyx - python graphics package." http://pyx.sourceforge.net/.

[52] G. Christian, *Spectroscopy of Neutron Unbound Fluorine*. PhD thesis, Michigan State University, 2011.

[53] M. Mosby, *Measurement of Excitation Energy in Projectile Fragmentation Reactions*. PhD thesis, Michigan State University, 2011.

[54] K. Makino and M. Berz, "Cosy infinity version 9," *Nuc. Instr. Meth. in Phys. A*, vol. 558, no. 1, pp. 346 – 350, 2006.

[55] N. Frank, A. Schiller, D. Bazin, W. A. Peters, and M. Thoennessen, "Reconstruction of nuclear charged fragment trajectories from a large gap sweeper magnet," *Nuc. Instr. Meth. in Phys. A*, vol. 580, pp. 1478–1484, 2007.

[56] A. Goldhaber, "Statistical models of fragmentation processes," *Physics Letters B*, vol. 53, no. 4, pp. 306 – 308, 1974.

[57] O. Tarasov, "Analysis of momentum distributions of projectile fragmentation products," *Nuclear Physics A*, vol. 734, no. 0, pp. 536 – 540, 2004. ¡xocs:full-name¿Proceedings of the Eighth International Conference On Nucleus-Nucleus Collisions¡/xocs:full-name¿.

[58] G. Audi and W. Meng. Private Communication, April 2011.

[59] G. Audi, A. Wapstra, and C. Thibault, "The ame2003 atomic mass evaluation: (ii). tables, graphs and references," *Nuclear Physics A*, vol. 729, no. 1, pp. 337 – 676, 2003. ¡ce:title¿The 2003 NUBASE and Atomic Mass Evaluations¡/ce:title¿.

[60] V. Maddalena, T. Aumann, D. Bazin, B. A. Brown, J. A. Caggiano, B. Davids, T. Glasmacher, P. G. Hansen, R. W. Ibbotson, A. Navin, B. V. Pritychenko, H. Scheit, B. M. Sherrill, M. Steiner, J. A. Tostevin, and J. Yurkon, "Single-neutron knockout reactions: Application to the spectroscopy of ^{16,17,19}C," *Phys. Rev. C*, vol. 63, p. 024613, Jan 2001.

[61] A. M. Bernstein, V. R. Brown, and V. A. Madsen, "Neutron and proton transition matrix elements and inelastic hadron scattering," *Physics Letters B*, vol. 103, no. 4-5, pp. 255 – 258, 1981.

[62] D. Bazin, A. Brown, B. M. Campbell, C. A. Church, J. C. Dinca, D. J. Enders, A. Gade, T. Glasmacher, G. Hansen, P. W. F. Mueller, H. Olliver, C. Perry, B. M. Sherrill, B. J. R. Terry, and A. Tostevin, J. "New direct reaction: Two-proton knockout from neutron-rich nuclei," *Phys. Rev. Lett.*, vol. 91, p. 012501, Jun 2003.

[63] J. A. Tostevin Private Communication.

[64] C. Rodríguez-Tajes, D. Cortina-Gil, H. Álvarez-Pol, T. Aumann, E. Benjamim, J. Benlliure, M. J. G. Borge, M. Caamaño, E. Casarejos, A. Chatillon, L. V. Chulkov, K. Eppinger, T. Faestermann, M. Gascón, H. Geissel, R. Gernhäuser, B. Jonson, R. Kanungo, R. Krücken, T. Kurtukian, K. Larsson, P. Maierbeck, T. Nilsson, C. Nociforo, Y. Parfenova, C. Pascual-Izarra, A. Perea, D. Pérez-Loureiro, A. Prochazka, S. Schwertel, H. Simon, K. Sümmerer, O. Tengblad, H. Weick, M. Winkler, and M. V. Zhukov, "Structure of $n22$ and the $n = 14$ subshell," *Phys. Rev. C*, vol. 83, p. 064313, Jun 2011.

[65] Z. Elekes, Z. Dombrádi, T. Aiba, N. Aoi, H. Baba, D. Bemmerer, B. A. Brown, T. Furumoto, Z. Fülöp, N. Iwasa, A. Kiss, T. Kobayashi, Y. Kondo, T. Motobayashi, T. Nakabayashi, T. Nannichi, Y. Sakuragi, H. Sakurai, D. Sohler, M. Takashina, S. Takeuchi, K. Tanaka, Y. Togano, K. Yamada, M. Yamaguchi, and K. Yoneda, "Persistent decoupling of valence neutrons toward the dripline: Study of $c20$ by γ spectroscopy," *Phys. Rev. C*, vol. 79, p. 011302, Jan 2009.

[66] L. Coraggio, A. Covello, A. Gargano, and N. Itaco, "Shell-model calculations for neutron-rich carbon isotopes with a chiral nucleon-nucleon potential," *Phys. Rev. C*, vol. 81, p. 064303, Jun 2010.

[67] B. A. Brown and W. D. M. Rae, "Nushellx@msu." http://www.nscl.msu.edu/ brown/resources/resources.html.

[68] P. Hansen, "Studies of single-particle structure at and beyond the drip lines," *Nuclear Physics A*, vol. 682, no. 1-4, pp. 310 – 319, 2001.